

Conditiebewaking aan de hand van statorstroomanalyse

Condition Monitoring with Motor Current Signature Analysis

Bram Corne

Promotoren: prof. dr. ir. J. Desmet, prof. dr. ing. J. Knockaert

Proefschrift ingediend tot het behalen van de graad van

Doctor in de ingenieurswetenschappen: werktuigkunde-elektrotechniek



**UNIVERSITEIT
GENT**

Vakgroep Elektrische Energie, Metalen, Mechanische Constructies en Systemen

Voorzitter: prof. dr. ir. L. Dupré

Faculteit Ingenieurswetenschappen en Architectuur

Academiejaar 2017 - 2018

ISBN 978-94-6355-078-9

NUR 959, 978

Wettelijk depot: D/2017/10.500/113



Ghent University
Faculty of Engineering and Architecture
Department of Electrical Energy, Metals,
Mechanical Constructions and Systems

Examination board:

prof. dr. ir. Jan Desmet	(promotor)	Ghent University (EA08)
prof. dr. ing. Jos Knockaert	(promotor)	Ghent University (EA08)
prof. dr. ir. Luc Taerwe	(chairman)	Ghent University (EA14)
prof. dr. ir. Sérgio M.A. Cruz		University of Coimbra
prof. dr. ir. Wim Serruys		Ghent University (EA08)
prof. dr. ing. Stijn Derammelaere		Antwerp University
prof. dr. ir. Sofie Van Hoecke		Ghent University (EA06)
prof. dr. ing. Kurt Stockman		Ghent University (EA08)
dr. ing. Bram Vervisch		Ghent University (EA08)

Ghent University campus Kortrijk
Faculty of Engineering and Architecture

Department of Electrical Energy, Metals, Mechanical Constructions and Systems
Research group EELAB - Lemcko
Graaf Karel de Goedelaan 34,
B-8500 Kortrijk, Belgium

Tel.: 0032 56 241 235

Dissertation for the degree:
Doctor of Electromechanical Engineering
Academic year: 2017-2018

Dankwoord

“ Een doctoraat? ... En euh... Wat is dat dan juist?”

Deze woorden gericht aan Jan Desmet werden in het labo van Lemcko uitgesproken tijdens het uitvoeren van metingen in het kader van mijn masterproef, voorjaar 2012. Op dat moment had Jan noch mezelf geen enkel idee waartoe dit initiërend gesprek zou leiden. Niettemin was dit de aanloop naar een vier jaar durend avontuur vol uitdagingen, hoogtepunten en tegenslagen, resulterend in het neerleggen van dit proefschrift. Het is bijgevolg niet onterecht dat dit dankwoord start met het bedanken van Jan, de promotor van mijn doctoraat. Dit niet alleen voor de financiering van dit onderzoek, maar vooral voor het eindeloze vertrouwen die hij mij gegeven heeft tijdens mijn jaren als doctoraalstudent. Ten allen tijde heb ik de vrijheid gekregen om het einddoel en de richting van mijn onderzoek zelf te bepalen, al was dit wat buiten de lijn van het klassieke Lemcko-onderzoek. Ook de verantwoordelijkheid die ik kreeg op onderwijsvlak, industrie-gerichte opleidingen, gerechtsexpertises en andere dienstverlening zorgden mee voor een verrijking op professioneel en persoonlijk vlak waar ik in de toekomst ongetwijfeld nog vruchten van zal plukken. Daarop aansluitend bedank ik graag Jos Knockaert, de wetenschappelijke copromotor van dit onderzoek. Jos zorgde er niet alleen voor dat dit gevoerde onderzoek kwaliteitsvol was, maar dat dit ook ten allen tijde relevant bleef naar industriële toepasbaarheid. Daarnaast had Jos ook zijn handen vol als moderator bij het temperen van de wetenschappelijke discussies tussen Jan en mezelf (twee identieke koppigaards die altijd gelijk hebben), waarvoor dank. Naast deze wetenschappelijke promotoren zorgde nog één persoon er rechtstreeks voor dat dit doctoraat op een succes is uitgedraaid. Zonder expliciete kennis te hebben van het onderzoek gaf hij me enorm waardevolle ‘tips and tricks’ in het voeren van een doctoraatsonderzoek. Zijn introductie tot de Gentse papiermolen, de juiste conferenties, de passende magazines, de maffiosi van uitgevers, een internationaal netwerk... hebben mijn onderzoekstraject zonder enig twijfel vergemakkelijkt. Bovenal leerde hij me dat naast het werken voldoende ruimte moet zijn voor ontspanning (ref. Berlijn, Coeur d’Alène, Lausanne, Miami). Colin Debruyne, mijn oprechte dank voor uw begeleiding.

Het allegaartje van personeel op UGent campus Kortrijk heeft heel wat verschillende wetenschappelijke uitdagingen en persoonlijke bekommernissen opduikend tijdens dit doctoraatsonderzoek van de baan geholpen. Dit in het bijzonder door: knappe kop Bram Vervisch; regeltechnieker Stijn Derammelaere; handige José Vangheluwe; IT-nerd Agkaton Bottenberg; papierexpert Fleur Ghekiere; businessman Bart Verhelst; frietjeslovers Wesley Cottegnie; en pompierke Bram

Vanseveren. Daarnaast mag het huidige en voormalige Lemcko-team niet vergeten worden, de jarenlange opbouw van kennis en expertise maakt het werk van de huidige en toekomstige wetenschappelijke onderzoekers aanzienlijk eenvoudiger.

Naast deze steunende collega's bevindt er zich nog een stevige achterban die mij jarenlang onvoorwaardelijke gesteund heeft: vrienden en familie. Om te beginnen moeten mijn ouders bedankt worden. De kansen die ik kreeg om te mogen én kunnen studeren waar en wat ik wil is een ferm onderschatte waarde die ik hopelijk ook aan mijn kinderen zal kunnen doorgeven. Zonder hun overgedragen waarden en normen zou ik nooit bereikt hebben waar ik op vandaag sta, dit op professioneel en persoonlijk vlak. Ook mijn liefste zusjes maken bewust of onbewust een noemenswaardig deel uit van de fundamenten van dit doctoraatsdiploma. De vele pittige discussies omtrent de maatschappelijke impact van de ingenieurswetenschappen ten opzichte van de psychologische wetenschappen hebben mijn passie voor techniek enkel maar aangewakkerd en verder ontwikkeld. Zij waren er bovendien telkens weer om me te helpen herinneren dat ik wat meer tijd moest maken voor mezelf en mijn gezinnetje. Tot slot rest mij enkel nog één persoon te bedanken, niettemin de meest belangrijke persoon die bedankt moet worden, Annelies Vanhoutte. Zij verdient op zijn minst de helft van de credits bij het behalen van deze doctorstitel. Afgekeurde papers, lastige examenperiodes, stressvolle presentaties, uitputtende vergaderingen... heeft ze vier jaar lang ondergaan met een niet te schatten hoeveelheid begrip en steun (zoals met kaasjes en salamiëtsjes). Hoe Annelies daarenboven elke dag opnieuw zorgde voor een perfect georganiseerd huishouden is iets waar ik niet genoeg respect voor kan betuigen. Ons dochtertje Estelle kan haar enkel maar gelukkig prijzen met zo'n fantastische moeder. Elke dag is het een groot genot om van het werk thuis te komen in ons warm gezinnetje. Annelies, bedankt voor alles!

Bram Corne

Kortrijk, December 2017

Table of Contents

English summary	xxv
Nederlandse samenvatting	xxix
1 Introduction	1-1
1.1 Preface	1-1
1.2 Problem statement	1-7
1.3 Research goal	1-11
1.4 Approach	1-13
1.5 Publication list Bram Corne	1-15
1.5.1 Journal publications	1-15
1.5.2 Conference publications	1-15
1.5.3 Other publications	1-16
2 A review on CM with MCSA	2-1
2.1 Introduction	2-1
2.2 Condition Monitoring technologies	2-2
2.3 Motor Current Signature Analysis	2-9
2.3.1 Stator signatures	2-10
2.3.2 Rotor signatures	2-12
2.3.2.1 Electrical Errors	2-13
2.3.2.2 Mechanical Errors	2-14
2.3.3 Bearing signatures	2-17
2.4 Conclusion	2-23
3 Stator current analysis	3-1
3.1 Introduction	3-1
3.2 Measurement method	3-2
3.2.1 Current measurement	3-4
3.2.2 Data acquisition	3-9
3.3 Frequency analysis	3-12
3.3.1 Discrete Fourier transformation	3-12
3.3.1.1 Aliasing	3-14
3.3.1.2 Leakage	3-17
3.3.1.3 Picket fence effect	3-20
3.4 Practical implementation	3-22
3.4.1 Digital signal processing	3-22
3.4.2 Current analysis tool	3-23

3.4.3	Case study	3-27
3.5	The Extended Park Vector Approach	3-33
3.6	Conclusion	3-35
4	Mechanical fault manifestation	4-1
4.1	Introduction	4-1
4.2	Rotor eccentricities	4-3
4.2.1	Misalignment	4-4
4.2.2	Mechanical unbalance	4-7
4.3	Bearing faults	4-10
4.3.1	Bearing outer race fault	4-11
4.3.2	Bearing inner race fault	4-14
4.3.3	Bearing cage fault	4-18
4.4	Validation of the bearing fault model	4-20
4.4.1	Multi-body dynamics simulation	4-20
4.4.2	Industrial test case	4-22
4.5	Conclusion	4-25
5	Fault emulating test-rig	5-1
5.1	Introduction	5-1
5.2	AMB dimensions	5-3
5.2.1	Steady state parameter estimation	5-3
5.2.2	Electromagnetic finite element simulation	5-6
5.3	AMB dynamics	5-7
5.3.1	AMB control design	5-8
5.4	Practical implementation	5-14
5.4.1	Position measurement	5-14
5.4.2	Current control	5-15
5.4.3	The AMB	5-16
5.4.4	Validating experiment	5-21
5.5	Conclusion	5-25
6	Experiments	6-1
6.1	Introduction	6-1
6.1.1	Emulating evolving mechanical faults	6-3
6.1.2	Analyzing variations in the stator current	6-3
6.2	Misalignment	6-7
6.3	Rotor unbalance	6-11
6.4	Bearing faults	6-15
6.4.1	Single point outer race bearing faults	6-15
6.4.2	Single point inner race bearing faults	6-18
6.4.3	Bearing cage faults	6-20
6.5	Conclusion	6-23
7	Conclusions	7-1
7.1	Overall conclusions	7-1
7.2	Future Research	7-3

8 Bibliography**8-1**

List of Figures

1.1	Both the occurrence and the impact of failure determines the criticality index of the machines X1 - X9	1-2
1.2	The simplified model of the rotor, stator and foundation for the vertical direction	1-8
1.3	The simplified model of the electric machine	1-9
1.4	Replacing the mechanical bearing by an active magnetic bearing enables the ability of inducing fault related rotor movements . . .	1-13
2.1	An infrared temperature analysis of two IMs severing bearing problems [1]	2-3
2.2	Measurement devices for performing advanced vibration analysis .	2-4
2.3	Example of a fault-indicating vibration spectrum with highlighted fault frequency components performed on the DE side of a 2 pole pair 250kW, 50Hz, 1416rpm IM, case study discussed in §3.4.3 .	2-6
2.4	General MCSA-algorithms indicate the faulty signatures in the stator current via spectral analysis	2-10
2.5	Examples of stator winding short-circuits, [1]	2-11
2.6	Examples of broken rotor bars, [1]	2-13
2.7	Detecting rotor speed with the ever-present unbalance and misalignment fault components in the stator current spectrum	2-15
2.8	Static (left) and dynamic (right) eccentricity	2-16
2.9	Examples of bearing problems, [1]	2-18
2.10	The commonly used dimensions for a regular ball bearing fault frequency calculation	2-18
2.11	The derivation of the kinematic model in obtaining the characteristic bearing fault frequencies	2-21
3.1	Two signals with the same RMS value but with another crest factor	3-3
3.2	The working principle of a Fluke® i400s current clamp (classic current transformer)	3-6
3.3	Working principle of measuring current with a Hall-element . . .	3-6
3.4	Fluke® i400s absolute fault for the 40A range	3-7
3.5	Fluke® i400s performance test set-up	3-8
3.6	The relative measurement error of the Fluke® i400s current clamp (circular markers and correlated with the striped line) and the Agilent current clamp (star marker and correlated with the full line) .	3-9

3.7	Zoom of the relative measurement error of the Fluke® i400s current clamp (circular marker) and the Agilent current clamp (star marker)	3-9
3.8	The <i>National Instruments</i> ™ cDAQ system to acquire voltage . . .	3-10
3.9	The frequency response function of the anti-aliasing filter in NI-9238 [8]	3-15
3.10	Visualization of the phenomenon aliasing. a) the gauss time function; b) the frequency function with aliasing (red bars); c) increasing the sample frequency reduces the overlap; d) applying an anti-aliasing filter resulting in no overlap	3-16
3.11	Visualization of the phenomenon leakage. a) the time signal where T_m is a multiple of $1/f_s$; b) an example of the unavoidable leakage in the spectrum; c) reducing the leakage in the spectrum by applying a Gaussian window on the time signal	3-19
3.12	Incorrect magnitude interpretation for two measurements (striped lines and solid lines) with minor frequency deviation due to the picket fence effect. The red line is the discretized spectrum and the black line is the transform using zeropadding, enhancing the spectral resolution [2,3].	3-20
3.13	The black spectral lines are the original spectrum, the striped line is how [4] interpolates to the real magnitude and frequency. The red spectral lines are the used components in the analysis.	3-23
3.14	Example of a generated plot by the current analysis tool, included with corresponding diagnosis for every fault related frequency component	3-26
3.15	Schematic presentation of the measured drive train	3-27
3.16	Searching for stable operational moments in time (torque and speed)	3-29
3.17	The spectra of vibration and current of the machine under test . .	3-30
3.18	The graphic interpretation of the Clarke Park transform	3-33
4.1	Static eccentricity (left) and dynamic eccentricity (right)	4-4
4.2	Excess of radial forces can have a serious impact on rotating machinery, [1]	4-5
4.3	Misalignments of two rotating shafts	4-5
4.4	Implying combined misalignment with the AMB	4-6
4.5	Misalignment defined by offset and gap difference	4-7
4.6	The quantification of mass-unbalance in a rotational system	4-8
4.7	Stator/rotor relation represented by two 2DOF model with mass m_r , stiffness k_r and damping c_r	4-10
4.8	A quantified single point bearing pit	4-11
4.9	Parameterized outer race impulse function for the vertical direction	4-12
4.10	Vertical rotor displacement for a specific single point bearing outer race fault, $y_o(t)$ (conditions in Table 4.1)	4-15
4.11	The vertical/horizontal impulse functions and rotor movements for the inner race bearing fault specified in Table 4.1	4-17
4.12	Rotor dynamic eccentricity when bearing cage fault occurs	4-19

4.13	The implementation of the bearing in the Multi-body dynamics simulation software <i>Siemens NX</i> [®] motion	4-20
4.14	The validation of the analytical faulty bearing rotor movement model by Multi-body dynamics simulation	4-22
4.15	The rotor movement $y_r(t)$ is calculated out of the measured vibration on the stator frame $\ddot{y}_s(t)$ using this 2DOF model	4-23
5.1	The SST-600 high-speed steam turbine of <i>Siemens</i> [®] equipped with AMBs	5-2
5.2	Magnetic bearing topology	5-4
5.3	The steady state attractive force u generated by a winding as a function the current through that winding, i , and the air gap between the rotor and the poles of that winding z (applicable for each of the four windings)	5-5
5.4	<i>Flux 2D</i> [®] simulation flux density (a) with 5A in the upper pole and 1A in the lower, left and right pole and a zoom in (b)	5-6
5.5	Simulink based model of the vertical AMB system	5-9
5.6	Comparing the simulation results with the set-points for a single point outer race bearing fault	5-11
5.7	Transformation from $s1$ and $s2$ to dx and dy	5-14
5.8	Distance x_3 between the original mechanical bearings and x_4 between the sensors and the bearing at NDE	5-16
5.9	The current sources which control the current through the four windings based on the output of the real-time controller	5-16
5.10	Perfect alignment between the AMB and stator housing of the electric machine using an Aluminum mounting structure	5-17
5.11	<i>Flux 2D</i> [®] simulation of the flux density with different current directions	5-18
5.12	Separating the AMB into eight separate coils in order to obtain the self and mutual inductances	5-19
5.13	The spatial presentation of matrix C for all 8 coils in the AMB, representing the rotor position independent values for the mutual inductances relatively to the self inductances	5-22
5.14	The AMB implemented at DE side of the 11kW IM	5-23
5.15	Comparing the simulation results with the emulation results for a single point outer race bearing fault	5-24
6.1	The GUI which is used to control the AMB and the DC machine	6-2
6.2	Thermal stability of the IM is obtained if the machine warms up under full load for at least 2h	6-4
6.3	The inner construction of the 11kW IM under test	6-5
6.4	The variation in speed during the 160 experiments has to be taken into account in the fault component calculation	6-7
6.5	The $i_e(t)$ spectra during emulated misalignment where $A_{\text{mis}} = 400\mu\text{m}$ with the indicated fault related frequencies f_{eccm} (rotor mixed eccentricity)	6-7

6.6	Varying frequency components in the EPVA vector during the emulation of misalignment/static eccentricity	6-8
6.7	Varying frequency components in the EPVA vector during the emulation of mass-unbalance/dynamic eccentricity	6-11
6.8	The $i_e(t)$ spectra during emulated unbalance where $m_{unb} = 1.6\text{kg}$ with the indicated fault related frequencies f_{eccm} (rotor mixed eccentricity)	6-12
6.9	The circular rotor movement visible in the direct and quadrature component $i_d(t)$ and $i_q(t)$	6-14
6.10	Maximum rotor displacement for a single point bearing outer race fault under varying pit depth and pit length obtained by simulations	6-16
6.11	Varying frequency components in the EPVA vector during the emulation of evolving single point outer race bearing pitting	6-16
6.12	Spectral EPVA vector $i_e(t)$ for an outer race bearing fault emulation where $l_{pit} = 2.5\text{mm}$	6-17
6.13	Varying frequency components in the EPVA vector during the emulation of evolving single point inner race bearing pitting	6-19
6.14	Spectral EPVA vector for an inner race bearing fault emulation where $l_{pit} = 2.5\text{mm}$	6-19
6.15	Varying frequency components in the EPVA vector during the emulation of an evolving bearing cage fault	6-21
6.16	Spectral EPVA vector for a bearing cage fault emulation where $A_{cage} = 150\mu\text{m}$	6-22

List of Tables

1.1	Fault classification for induction machines, [1]	1-4
2.1	Classification of vibration severity zones for machines of Group 1: Large machines with rated power above 300kW and not more than 50MW; electric machines with shaft height $\geq 315\text{mm}$, [5]	2-4
2.2	IM vibration fault frequencies	2-5
2.3	MCSA compared to Vibration analysis, [2]	2-7
3.1	Current measurement methodologies, [6]	3-4
3.2	Fluke® i400s current clamp properties	3-7
3.3	Error made by capturing 10A using the Fluke® i400s current clamp [7] and the NI-9181 DAQ-card [8]	3-11
3.4	Commonly applied types of window, [3, 9]	3-18
3.5	The calculated spectral fault diagnosing frequencies as was presented in §2.3	3-24
3.6	Detailed information from the vibration fault frequencies as in Table 2.2	3-31
3.7	Detailed information from the current fault frequencies as in §2.3	3-32
4.1	Calculation parameters	4-14
4.2	Bearing SKF® 6302 - 2Z parameters and pit dimensions	4-21
4.3	Bearing SKF® 6226 - C3 parameters	4-24
5.1	Fixed AMB parameters	5-4
5.2	Variable AMB parameters	5-5
6.1	Nameplate parameters of the IM under test	6-4
6.2	Misalignment trending functions of the detected fault components in the EPVA vector	6-10
6.3	Unbalance trending functions of the detected fault components in the EPVA vector	6-13
6.4	Trending functions of the spectral outer race fault components in the EPVA vector	6-18
6.5	Trending functions of the spectral inner race fault components in the EPVA vector, $i_e(t)$	6-20
6.6	Trending functions of the spectral cage defect fault components in $i_e(t)$	6-21

6.7 Comparing the emulation results with real bearing fault test cases
(all IMs) 6-24

List of Acronyms

#

2DOF	Two Degrees Of Freedom
------	------------------------

A

AC	Alternating Current
ADC	Analog-Digital-Conversion
AMB	Active Magnetic Bearing

B

BPFO	Ball Pass Frequency Outer race
BPFI	Ball Pass Frequency Inner race
BSF	Ball Spin Frequency

C

CM	Condition Monitoring
----	----------------------

D

DC	Direct Current
DFT	Discrete Fourier Transform
DOL	Direct On-Line
DE	Drive End

E

EMC	Electro-Magnetic Compatibility
EPVA	Extended Park Vector Approach

F

FEA	Finite Element Analysis
FFT	Fast Fourier Transform
FTF	Fundamental Train Frequency

G

GUI	Graphical User Interface
-----	--------------------------

I

IM	Induction Machine
----	-------------------

M

MCSA	Motor Current Signature Analysis
MMF	Magneto Motive Force
MTBF	Mean Time Between Failures
MTTF	Mean Time To Failure

N

NDE	Non Drive End
-----	---------------

P

PWM Pulse Width Modulation

R

RCFA Root Cause Failure Analysis
RMS Root Mean Square
rpm rotations per minute

S

SNR Signal to Noise Ratio

U

UMP Unbalanced Magnetic Pull

List of Symbols

–In order of appearance–

k	harmonic integer 1, 2, 3 . . .	[–]
f_r	the rotational speed	[Hz]
n_b	the number of bearing balls	[–]
bd	the bearing ball diameter	[mm]
pd	the bearing pitch diameter	[mm]
β	the bearing contact angle	[rad]
f_{st}	the characteristic stator winding fault frequency	[Hz]
f_1	the frequency of the fundamental current component	[Hz]
p	the number of pole pairs	[–]
s	the rational slip frequency	[–]
n	harmonic integer 1, 3, 5 . . .	[–]
f_{bar}	the characteristic rotor bar fault frequency	[Hz]
f_{ecc}	the main eccentricity fault frequency	[Hz]
n_{rs}	the number of rotor slots	[–]
v	harmonic integer 1, 3, 5 . . .	[–]
n_d	the eccentricity defining integer	[–]
f_{eccm}	the characteristic mixed eccentricity fault frequency	[Hz]

f_{out}	the outer race bearing fault indicating frequency	[Hz]
f_{in}	the inner race bearing fault indicating frequency	[Hz]
f_{ball}	the characteristic bearing ball spin indicating frequency	[Hz]
f_{cage}	the bearing cage indicating fault frequency	[Hz]
F_s	the sample rate	[Hz]
T_m	the measuring time	[s]
ω_1	the frequency of the fundamental current component	[rad/s]
f_{eccs}	the static eccentricity frequency	[Hz]
f_{eccd}	the dynamic eccentricity frequency	[Hz]
$i_a(t)$	the time-based stator current through phase 'a'	[A]
$i_b(t)$	the time-based stator current through phase 'b'	[A]
$i_c(t)$	the time-based stator current through phase 'c'	[A]
$i_\alpha(t)$	the positive sequence current	[A]
$i_\beta(t)$	the negative sequence current	[A]
$i_\gamma(t)$	the zero sequence current	[A]
$i_d(t)$	the direct current component	[A]
$i_q(t)$	the quadrature current component	[A]
$i_e(t)$	the extended Park vector approach component	[A]
dy	the vertically induced rotor movement during mechanical faults	[mm]
dx	the horizontally induced rotor movement during mechanical faults	[mm]
c_{offset}	the misalignment offset parameter	[mm]
c_{gapdiff}	the misalignment gap difference parameter	[mm]
d_r	the rotor shaft diameter	[mm]

m_{unb}	the equivalent working rotor mass-unbalance	[g]
r_{unb}	the radial location of the mass-unbalance to the rotor centre	[mm]
m_{r}	the mass of the rotor	[kg]
c_{r}	the bearing damping factor	[Ns/m]
k_{r}	the bearing stiffness factor	[N/m]
$h_{\text{y}}(t)$	the fault related vertical rotor/stator impulse function	[N]
$h_{\text{x}}(t)$	the fault related horizontal rotor/stator impulse function	[N]
$\ddot{y}(t)$	the vertical rotor acceleration	[m/s ²]
$\dot{y}(t)$	the vertical rotor velocity	[m/s]
$y(t)$	the vertical rotor displacement	[m]
$\ddot{x}(t)$	the horizontal rotor acceleration	[m/s ²]
$\dot{x}(t)$	the horizontal rotor velocity	[m/s]
$x(t)$	the horizontal rotor displacement	[m]
α_{pit}	the angular position of the faulty outer race pit	[rad]
l_{pit}	the length of the single point bearing pit (inner or outer)	[mm]
d_{pit}	the depth of the single point bearing pit (inner or outer)	[mm]
γ_{pit}	the angle of the ramp in the single point bearing pit (inner or outer)	[rad]
g	the gravitational acceleration	[m/s ²]
$I_{\text{n,y,o}}$	the negative magnitude of the vertically imposed force during outer race faults	[N]
$I_{\text{n,x,o}}$	the negative magnitude of the horizontally imposed force during outer race faults	[N]
$I_{\text{p,y,o}}$	the positive magnitude of the vertically imposed force during outer race faults	[N]
$I_{\text{p,x,o}}$	the positive magnitude of the horizontally imposed force during outer race faults	[N]

$t_{n,o}$	the exact time of the working forces $I_{n,y,o}$ and $I_{n,x,o}$	[s]
$t_{p,o}$	the exact time of the working forces $I_{p,y,o}$ and $I_{p,x,o}$	[s]
$v_{b,o}$	the speed of a bearing ball with respect to the outer race	[m/s]
f_{FTF}	the fundamental train frequency of the bearing (FTF)	[Hz]
t_o	the time between two periodic impacts for an outer race bearing fault (BPFO)	[s]
$I_{n,y,i}$	the negative magnitude of the vertically imposed force during inner race faults	[N]
$I_{n,x,i}$	the negative magnitude of the horizontally imposed force during inner race faults	[N]
$I_{p,y,i}$	the positive magnitude of the vertically imposed force during inner race faults	[N]
$I_{p,x,i}$	the positive magnitude of the horizontally imposed force during inner race faults	[N]
$t_{n,i}$	the exact time of the working forces $I_{n,y,i}$ and $I_{n,x,i}$	[s]
$t_{p,i}$	the exact time of the working forces $I_{p,y,i}$ and $I_{p,x,i}$	[s]
$v_{b,i}$	the speed of a bearing ball with respect to the inner race	[m/s]
h_{int}	the interaction curve between inner race fault and the rotor	[—]
t_i	the time between two periodic impacts for an inner race bearing fault (BPFI)	[s]
ϕ	the initial condition for the calculation of the rotor movement during inner race faults	[rad]
$h_{y,o}(t)$	the vertical impulse function on the rotor for outer race bearing faults	[N]
$h_{x,o}(t)$	the horizontal impulse function on the rotor for outer race bearing faults	[N]
$h_{y,i}(t)$	the vertical impulse function on the rotor for inner race bearing faults	[N]
$h_{x,i}(t)$	the horizontal impulse function on the rotor for inner race bearing faults	[N]
$y_o(t)$	the vertical rotor movement during outer race bearing faults	[m]
$x_o(t)$	the horizontal rotor movement during outer race bearing faults	[m]
$y_i(t)$	the vertical rotor movement during inner race bearing faults	[m]

$x_i(t)$	the horizontal rotor movement during inner race bearing faults	[m]
$u(t)$	the time-based force created by one winding of the AMB	[N]
μ_0	the magnetic permeability of air	[H/m]
N	the number of turns in one winding of the AMB	[—]
$i(t)$	the time-based current through a winding of the AMB	[A]
l_{stat}	the length of the flux path through the AMB	[m]
μ_{rstat}	the relative permeability of the AMB's laminated steel	[—]
l_{sh}	the length of flux path through the shaft in the AMB	[m]
μ_{rsh}	the relative permeability of the shaft in the AMB	[—]
$z(t)$	the time-dependent air gap between the AMB and the shaft	[mm]
A_a	the usable area for the flowing flux through the AMB	[mm ²]
α	the angle between the winding center and the acting force of the AMB	[rad]
$v(t)$	the time varying voltage applied on one winding of the AMB	[V]
R_w	the resistance of one winding of the AMB	[Ω]
L_w	the inductance of one winding of the AMB	[H]
$\mathcal{R}_m(t)$	the magnetic reluctance of the flux path for one AMB winding	[1/H]
$L_{\text{PID}}(s)$	the Laplace-based control function of the AMB	
K_p	the PID proportional factor	
K_d	the PID derivative factor	
K_z	the AMB linearized position stiffness factor	
K_i	the AMB linearized current stiffness factor	
$V(t)$	the vector of time-based voltages applied on every coil of the AMB	[V]
R	the vector of the resistances of every coil of the AMB	[Ω]

$I(t)$	the vector of time-based currents through every coil of the AMB	[A]
$M(z)$	the overall position-dependent matrix of self and mutual inductance of the AMB	[H]
r^2	the coefficient of determination for a fitted polynomial on measurement data	[—]

English summary

Electric rotating machinery has become indispensable in the nowadays industrial activities. Comprehensibly, since these machines transform electrical energy into mechanical energy with a particularly high efficiency. Although robustness and reliability are key-properties of those machines, unexpected premature failures often occur. Concerning industrial production processes, those break-downs can easily lead to enormous economical losses. This is not only due to the replacement value of the broken machine, but the economical loss of production is generally exceedingly high. One way of suppressing those premature failures is establishing a predictive maintenance program. The implementation of such a program consists mostly of applying a condition monitoring system. This system monitors the condition of the machine continuously. When a certain machine problem occurs which can lead into an abrupt failure of the machine, the condition monitoring device has the task of alarming and informing the machine operator or manager. That informative message is required to contain two major parts. First, a specific identification of the detected problem. This is usually done on component level. The second part is an estimated time-to-failure i.e. the remaining secured running time. This time-based information is crucial for the machine operator in order to estimate the urgency of the problem and subsequently plan the proper restoration/repair or replacement of the machine. A message stating that there is a problem with e.g. one of the machine bearings without knowing how fast it can lead into the abrupt breakage of the machine has less value to the machine operator.

During the last decades, intense industry driven efforts have led into the development of several condition monitoring technologies by e.g. analyzing vibrations, currents, temperatures or fluxes. The most applied, reliable and advanced monitoring technique is undoubtedly vibration analysis. Applying this technique, incipient faults of various origin can be detected on component-level supplemented with a corresponding severity estimation using the ISO 10816-standard. However, as acceleration has to be measured, this technique remains relatively expensive; is susceptible to various interferences; requires significant high maintenance; does not include the detection of electrical faults; is dependent on the machine structure/mounting... Another condition monitoring technique which counters these disadvantages is based on stator current measurements, commonly addressed to as motor current signature analysis. This is a rather new, still developing condition monitoring technology. Applying this technique, the condition of the machine is estimated by measuring the current through the stator windings. This has the advantage of being less expensive, more robust and is able to detect more evolving machine problems than the nowadays commercially available technologies. Additionally, measuring current does not require any access to the machine itself, which

is interesting regarding harsh environments or machines installed at inaccessible locations. Following the current state of the art, the most common electrical and mechanical problems can be distinguishably detected and accurately identified by analyzing the stator current fault signatures. However, as soon as an evolving problem is detected, the required time-to-failure has to be estimated. Regarding the detection of electrical faults (stator winding shortcut, rotor bar breakage...), literature provides sufficiently accurate reference tables in which the fault severity can be estimated out of a rational expression of the detected fault components in the stator current. Nevertheless, regarding mechanical faults (bearing problems, unbalance and misalignment), the severity estimation is completely lacking in today's current-based monitoring techniques. This implies a decisive limitation, as for low voltage machines the majority of the unexpected failures has a mechanical origin. Consequently, extensive research is still needed regarding the relation between mechanical faults and their reflection in the stator current. Only if these relations between the severity of mechanical faults and their corresponding reflection in the stator current can be quantified, stator current analysis can finally be implemented as a robust and reliable condition monitoring technology.

The currently available analytical models and finite element software packages mainly focus either on the electrical or mechanical part without including the critical transition in between. The few simulation platforms including this transition are usually too simplistic or lack advanced manipulation to obtain representative and translatable results. As a consequence, experimental research is to be conducted. The propagation of mechanical faults and their reflection in the stator current can be quantified by building a mechanical fault emulator which can impose all kinds of mechanical faults on an electric machine with high accuracy and reproducibility. As most mechanical problems are characterized by specific movements of the machine rotor with respect to the stator, manipulating the rotor position can inversely result in obtaining a fault emulating test-rig. This manipulation can be established by replacing the mechanical drive end side bearing of the electric machine under test by an active magnetic bearing. Thereby, the magnetic bearing enables the recreation of most mechanical problems by imposing fault related rotor movements on an accurate and reproducible way. By correctly designing the control loop of the magnetic bearing, the bearing can physically act as the mechanical bearing would do by adopting its stiffness and damping properties. Subsequently, by simultaneously measuring the stator current during emulation, relations can be quantified between the emulated mechanical fault and the stator current fault signatures. Furthermore, the influence of several other parameters on that quantification can be investigated thoroughly e.g. variations in torque, speed, temperature, power quality, coupling characteristics... Obtaining this goal was done by tackling three main scientific challenges, resulting in three main contributions into the field of stator current based condition monitoring. Firstly, a unique analytical model was obtained which is able to estimate the fault induced rotor movements with respect to the stator for different conditions considering speed, torque, bearing dimensions, bearing properties, fault type, severity... This enables the possibility of calculating every fault related rotor movement subjected to misalignment, mass-unbalance, outer race bearing faults, inner race bearing faults and bearing cage problems. These movements are required to serve as set points for the fault im-

posing magnetic bearing. The second main contribution is the establishment of the novel fault emulating test-rig. The active magnetic bearing was dimensioned and implemented at drive end side of an induction machine to induce the mechanical faults by imposing the obtained fault related rotor/stator movements. The successful realization of the mechanical fault emulator led to the third and last main contribution: the fault quantification. The impact of evolving mechanical faults on the induction machine stator current fault signatures was experimentally investigated. Using this unique and novel way of reproducibly emulating mechanical faults, specific relations are quantified between the severity of multiple mechanical faults and their corresponding reflection in the stator current. This research completed a crucial step towards the ability of implementing stator current analysis as a condition monitoring technology for industry-implemented electric rotating machines with critical functionalities.

Nederlandse samenvatting

– Summary in Dutch –

Elektrisch roterende machines zijn onmisbaar geworden in de hedendaagse industriële omgeving. Begrijpelijk, aangezien ze elektrische energie naar mechanische energie kunnen transformeren met een enorm hoge efficiëntie. Alhoewel de machine gekend staat om zijn betrouwbaarheid en robuust karakter, komt het onverwachts falen van deze machine zeer vaak voor. Met het oog op industriële productieprocessen kan dit falen gemakkelijk leiden tot enorm hoog oplopende economische kosten. Deze kost omvat niet enkel de vervangingswaarde van de machine, maar het economische verlies door de uitval van productie overstijgt deze kost gewoonlijk met een veelvoud van de vervangingswaarde. Een manier om dit vervroegd falen tegen te gaan is het opzetten van een predictief onderhoudsprogramma. De implementatie van dergelijk programma houdt onder andere het toepassen van conditiebewaking in. Dit betekent letterlijk het continu monitoren van de gezondheidstoestand van de machine. Indien vervolgens een bepaalde fout zich voordoet die kan leiden tot een onverwachts falen, heeft het bewakingssysteem de taak om de operator/manager van de machine in te lichten. Dit informatief bericht bestaat uit twee cruciale onderdelen: enerzijds de specifieke beschrijving en locatie van het probleem, dit meestal op componentenniveau. Anderzijds bevat het bericht een berekening van de resterende tijd-tot-falen, met andere woorden een inschatting van hoelang de machine met hoge zekerheid nog zal blijven werken. Die tijdsbepaling is voor de operator cruciaal om een inschatting te kunnen maken omtrent de urgentie van het probleem en vervolgens de gepaste restauratie/herstelling/vervanging te kunnen inplannen. De operator heeft namelijk weinig informatie aan een bericht waarbij gesteld wordt dat één van de machines lagers een defect vertoont zonder accuraat in te kunnen schatten hoelang de machine met een hoge zekerheid zal blijven werken.

Als een gevolg van dit besparingspotentieel heeft zowel de academische wereld als de industrie de laatste tientallen jaren enorm veel geïnvesteerd in conditiebewakingssystemen op basis van verschillende technieken waaronder het meten van trillingen, elektrische stroom, temperatuur of flux. De meest toegepaste en op vandaag geavanceerde techniek is ongetwijfeld trillingsanalyse. Met behulp van deze techniek kan tot op componentenniveau een exacte foutidentificatie uitgevoerd worden. Vervolgens kan, gebruikmakend van de ISO 10816-normering, een ernst aan deze gedetecteerde fout gekoppeld worden. Aangezien hierbij accelerometers gebruikt moeten worden, zijn aan deze methode inherent nadelen verbonden: de techniek blijft nog steeds relatief duur; is sterk onderhevig aan verschillende omgevingsfactoren; vergt een intensief onderhoud; omvat geen detectie

van elektrische problemen in de machine; is sterk afhankelijk van de machinestructuur en -bevestiging... De meeste van deze nadelen kunnen worden weggewerkt door het gebruiken van de statorstroom als een conditiebewakingstechniek. Statorstroomanalyse is een behoorlijk nieuwe conditiebewakingstechnologie in volle ontwikkeling. Deze technologie tracht de volledige conditietoestand van de machine te bepalen door de stromen door de stator windingen te analyseren. Dit heeft het voordeel dat de metingen goedkoper, robuuster, nauwkeuriger en meer volledig zijn dan de op vandaag commercieel beschikbare technieken. Daarenboven kan de stroom vanuit de elektrische stuurkast gemeten worden, wat zeer voordelig blijkt bij machines opgesteld in ruige omgevingen of op ontoegankelijk locaties. Met de huidige state of the art is het reeds mogelijk om het merendeel van de elektrische en mechanische fouten in de machine te detecteren en identificeren op basis van stroommetingen. Daarbij is het echter ook belangrijk dat een voldoende correcte ernstbepaling uitgevoerd kan worden. Op vlak van elektrische problemen zoals kortsluitingen in de statorwindingen of gebroken rotorstaven, worden in de literatuur voldoende methodes teruggevonden die deze ernstbepaling accuraat kunnen uitvoeren. Bij het detecteren van mechanische fouten zoals lagerproblemen, massa onbalans en uitlijnfouten blijft deze ernstbepaling echter op zich wachten. Aangezien voor machines werkend op laagspanning het onverwachts falen voor het overgrote merendeel aan mechanische fouten toe te wijzen valt, impliceert dit gebrek een belemmerende tekortkoming. Bijgevolg is verder onderzoek vereist om het verband tussen mechanische fouten en hun reflectie in de statorstroom in kaart te brengen. Enkel wanneer dit verband tussen de ernst van de mechanische fout en de overeenkomstige reflectie in de statorstroom voldoende gekwantificeerd kan worden, kan statorstroomanalyse als een compleet en betrouwbaar conditiebewakingssysteem toegepast worden.

De huidig beschikbare analytische modellen en magnetische eindige elementen pakketten zijn voornamelijk gefocust op het elektrische enerzijds of op het mechanische aspect anderzijds zonder de exacte transitie daartussen erbij te betrekken. De enkele simulatieplatformen die deze transitie dan toch opnemen zijn gewoonlijk te sterk vereenvoudigd of te weinig manipuleerbaar om representatieve resultaten te boeken. Dit resulteert in het kiezen voor experimenteel onderzoek om de voorgenoemde probleemstelling te behandelen. De vertaling van mechanische fouten naar de statorstroom kan gekwantificeerd worden met behulp van een mechanische foutemulator die de fouten emuleert met een hoge nauwkeurigheid en reproduceerbaarheid. Aangezien de meeste mechanische problemen voorgesteld kunnen worden als een specifieke beweging van de rotor ten opzichte van de stator, kunnen ook omgekeerd mechanische fouten in een machine geïnduceerd worden door de rotor te manipuleren. Dit zal in dit onderzoek verwezenlijkt worden door het lager aan aandrijfszijde van de geteste elektrische machine te vervangen door een actief magnetisch lager. Op deze manier kan dit magnetische lager die mechanische foutgerelateerde rotorbewegingen nauwkeurig en reproduceerbaar nabootsen. Door het correct dimensioneren van het bijhorende controlesysteem kan dit magnetisch lager zich fysiek gaan gedragen als het oorspronkelijke mechanische lager. Dit door middel van de stijfheid- en dempingseigenschappen van het originele lager over te nemen. Vervolgens kan, door het simultaan meten van de statorstroom tijdens emulatie, de verbanden tussen de geëmuleerde fout

en de stroomcomponenten in de stator geanalyseerd worden. Bovendien kan de invloed van verschillende omgevingsfactoren op dit transmissiepad nauwkeurig onderzocht worden zoals variaties in koppel, toerental, temperatuur, power quality. . . Deze doelstelling werd verwezenlijkt door het aanpakken van drie hoofdzakelijk wetenschappelijke uitdagingen, resulterend in drie fundamentele bijdragen. Ten eerste werd een uniek analytisch model opgesteld waarbij de exacte rotorbewegingen bij het optreden van mechanische fouten analytisch bepaald worden in functie van de snelheid, het koppel, de lagerdimensies, de lagereigenschappen, ernst van de fout. . . Zo kunnen de rotorbewegingen gerelateerd aan uitlijnfouten, massa onbalans en lagerfouten onmiddellijk bepaald worden onder verschillende omstandigheden. Deze analytische beschrijving van de foutgerelateerde rotorbewegingen is noodzakelijk om het magnetische lager aan te sturen. De tweede fundamentele bijdrage is het opstellen van de innovatieve mechanische foutemulator. Het magnetisch lager werd gebouwd dat effectief de foutieve rotorbewegingen op een reproduceerbare manier kan induceren in een elektrische machine. Het succesvol voltooiën van deze foutemulator leidt tot de derde en laatste hoofdzakelijke bijdrage: de effectieve foutkwantificering. De impact van verschillende ontwikkelende mechanische fouten op de statorstroom experimenteel onderzocht worden. Met behulp van deze innovatieve wijze om mechanische fouten nauwkeurig en reproduceerbaar te emuleren, werden specifieke verbanden vastgesteld en gekwantificeerd tussen de ernst van verschillende foutsoorten en hun overeenkomstige reflectie in de statorstroom. Dit onderzoek heeft een significante stap vooruit gezet naar het uiteindelijke gebruik van statorstroomanalyse als een betrouwbare conditiebewakingstechnologie voor industriële elektrisch roterende machines met kritische functionaliteiten.

1

Introduction

1.1 Preface

Around 50% of the worldwide produced electrical energy is consumed by electric rotating machinery [10]. Comprehensibly, since these types of machines can transform electrical energy into mechanical energy on a supremely easy, reliable, reversible and efficient way. The major part of that energy consumption, about 70%, can be allocated to the industry. As a consequence, those machines have become indispensable in the nowadays industrial environment. The purpose of the installed rotating machinery in industrial applications varies from simply ventilating fabrication halls to actuating highly crucial and precise production processes such as plastic extraction. Although robustness and reliability are both key properties of these machines, unexpected premature failure occurs quite often. Literature points out that on average 9% of all electric machines fail prematurely [11]. These abrupt failures can easily lead to a heavily disruption of the company's normal operation, directly implying a significant amount of economic loss. In general, the cost of the machine itself is a negligible small part in comparison with the loss of production, demounting, reassembling, re-initialization... Particularly in the food industry and other continuous manufacturing processes with high quality requirements, extremely high costs are imposed by the sudden failure of one of the machines in the chain of production [11]. However, not every machine failure in the industry implies huge economic costs. The way machines are represented in their importance or criticality is called the *criticality index*, [1, 12]. That is a weighted value which considers the frequency of failures and the impact of the failure, graphically presented in Figure 1.1. For example, a machine with a high failure rate such as three times per year with an impact of €80.000 can be defined

evenly critical as a machine with a failure rate of once every 15 years with an impact of €4 million. This dissertation handles a condition monitoring technique which is a part of a predictive maintenance program with the aim of reducing unexpected failure. The focus is hereby on electric machines defined as critical. Out of a self-conducted market survey within the IOF-project "CM with MCSA" funded by the Flemish government, the vast majority of the industrial machines defined as critical are determined to be *Asynchronous Squirrel Cage Induction Machines* or commonly referred to as *Induction Machines* (IMs). Consequently, this dissertation focuses on this type of machine only, connected Direct-On-Line (DOL).

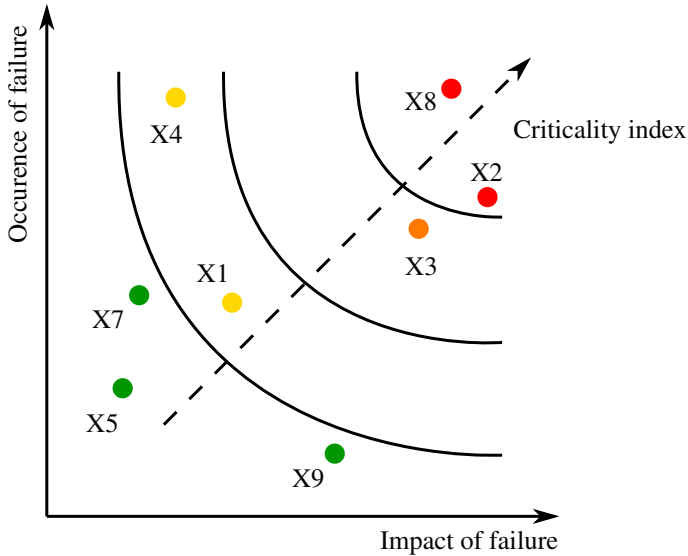


Figure 1.1: Both the occurrence and the impact of failure determines the criticality index of the machines X1 - X9

Considering premature failures, where *premature* has the definition of failing before the specified lifetime by the manufacturer and *failing* has the definition of shutting down where a restart is impossible, the origin can be of numerous reasons. Apart from the specific reason of the machine failure, it is usually opportune to avoid another failure in the future due to that same cause. In order to do so, *Root Cause Failure Analysis* (RCFA) can be performed. Applying this technique, the root cause of each occurring failure can be determined following a specific procedure which could significantly avoid future failures [1]. Additionally, gaining knowledge on the machine behavior using RCFA is useful in the detection of problems which can lead into the machine failure. As an example, the root cause of a failed bearing at Drive End (DE) side of an IM could be:

- a preload miscalculation while dimensioning/developing the machine;

- heavy vibrations due to cavitation in a pump driven by the machine;
- lubrication contamination due to badly maintaining the machine;
- induced bearing currents from a variable frequency drive;
- a misalignment between the machine and its application; ...

In order to obtain a certain categorization in the root cause of failing rotating machinery, several stress categories are defined e.g. thermal, electrical, mechanical and environmental [1]. Almost every part of the machine could be exposed to one or more of those stresses and subsequently lead into a premature failure. Table 1.1 presents a brief overview of the most common stresses/damages causing premature failing of the main IM components implemented in the petroleum and chemical industry, [1]. As can be noticed, the root cause of a failing machine can be found in a certain part of the machine which physically can not lead directly to the abrupt failing of the machine. For example, a broken rotor bar could result in an overheated rotor, which can sequentially cause an axially overloaded bearing and subsequently result in a bearing failure. Or, that same broken rotor bar can cause the stator winding to overheat due to the loss of efficiency and eventually cause a fatal stator winding shortcut. Therefore, the distinction is made between the direct and the indirect cause of a failure. The direct cause is the cause which made the machine fail, like in previous example the bearing or the stator winding. The indirect or root cause is determined to be the real origin of the fault, the broken rotor bar for the previous example. The direct cause of failure for low-voltage machines is in practice found to be 85% bearing related, complemented with 10% stator winding shortcuts and a 5% environmental issues (mechanical impacts due to accidents) [1]. The indirect causes of failing IMs can be assigned to four main machine parts, presented with their probability of occurrence, [13–17]:

- bearing related: 40% ;
- stator related: 38% ;
- rotor related: 12% ;
- other: 10% .

Conclusively, machine failures can have an infinite number of root causes which eventually lead into the direct failure of four main machine parts or components.

Considering critical machines installed in industrial production processes where the uptime is crucial, it is opportune to avoid each premature or unexpected failure by any cause [13–31]. In order to optimize the life-cycle of those machines, a lot of effort has already been made in setting up maintenance programs. Research concluded that the cost of maintaining the critical machines is by far negligible with respect to the savings obtained by avoiding premature failures of any kind. Implementing a maintenance program can be done by four main maintenance strategies, following [5] defined and hereafter described as: corrective, periodic, predictive and proactive maintenance.

Part	Stress-category	Actual stress/damage
Bearings	Thermal	Friction, lubricant, ambient
	Dynamic/static loading	Radial, axial, preload, misapplication
	Vibration and shock	Rotor, driven equipment, system
	Environmental	condensation, foreign materials, excessive ambient, poor ventilation
	Mechanical	Loss of clearances, misalignment, shaft and housing fits
	Electrical	Rotor dissymmetry, electrostatic coupling, static charges, variable-frequency drives
Stator	Thermal	Aging, overload, voltage variation/unbalance, ambient, poor ventilation
	Electrical	Dielectric aging, transient voltages, partial discharge (corona), tracking
	Mechanical	Winding movement, damaged motor leads, improper rotor-to-stator geometry
	Environmental	Moisture, chemical, abrasion, poor ventilation, excessive ambient
Rotor	Thermal	Thermal overload/unbalance, excessive rotor losses, hot spots, incorrect direction of rotation
	Dynamic	Vibrations, loose rotor bars, rotor rub, transient torque, centrifugal force/over-speed
	Mechanical	Casting variations, loose laminations, incorrect shaft-to-core fit, improper rotor-to-stator geometry, improper mounting/design
	Environmental	Corrosion, abrasion, foreign materials, poor ventilation, excessive ambient temperature
	Magnetic	unbalanced magnetic pull, lamination saturation, circulating currents, vibration
	Residual	Stress concentrations, uneven cage stress
	Miscellaneous	Misapplication, poor design, manufacturing variations, improper operation/mounting

Table 1.1: Fault classification for induction machines, [1]

Corrective maintenance is the so called *run-to-failure*-strategy. This means that the machine is operating without any efforts to minimize the chance of premature failing. The machine simply runs until it breaks down. Mostly, if the machine power size is sufficiently large, the machine can be revived by replacing the failed parts. In some applications, corrective maintenance is the optimal strategy in the economical perspective. If the unexpected failure of that specific machine does not imply a significant higher cost than replacing the machine itself, no maintenance effort should be made (low criticality index). However, this maintenance strategy can effectively be applied for very small and/or cheap machines with a significantly high criticality index. It is commonly applied for these type of drive-trains to place a second (or even third), exactly the same drive-train next to the used power line in order to increase the redundancy instead of applying any other kind of maintenance strategy. When one of the machines fails, the other one takes over the functionalities instantaneously. This type of redundancy avoids the shut-down of the production process but however does not affect the lifetime of the drive-train.

Periodic maintenance is a preventive maintenance strategy containing a pre-defined, periodical inspection of every machine condition. This inspection can range from a brief visual control to accurately measuring certain electrical and/or mechanical parameters which can determine the condition of certain machine parts (e.g. performing insulation resistance tests). In most cases, these interventions are conducted while the machine is off-line. Nevertheless, more and more, vibrations and/or thermal analysis is performed on-line in order to estimate the operational condition. The maintenance itself can vary from superficially cleaning the machine to regreasing or even replacing the machine bearings. Some companies gained a lot of experience in periodic maintenance and developed extensive maintenance schedules for every type of machine included in their specific industrial plant. The cost of this type of strategy can differ a lot. A balance should be found between the operational cost of the maintenance plan and the gained profit in the machine life time and avoidance of unexpected breakdowns. Usually, the number of periodic interventions is determined by the condition of the machine. If the machine is running without any suspicion of evolving problems, the frequency is commonly one measurement each month. If that machine is increasing in levels of vibration and/or temperature, the frequency can increase to one intervention each day. Of course, when applying a periodic maintenance strategy, a significant chance of premature failure between the interventions remains.

Predictive maintenance is the most advanced, effective and efficient way of maintaining an electric rotating machine defined as critical. Therefore, it is as well the most expensive strategy. Predictive maintenance is basically estimating a time which states how long the machine will keep running under good conditions. That time is commonly known as the *Mean-Time-To-Failure* (MTTF) or *Mean-Time-Between-Failures* (MTBF). Fault indicating parameters of the machine are usually monitored continuously in order to predict the MTTF/MTBF. This prediction is very useful for the machine operator, because then he can judge the urgency of

the problem and decide on the proper maintenance intervention. This maintenance strategy is generally performed by applying *Condition Monitoring* (CM). In this way, the machine is continuously monitored in order to evaluate the condition and estimate a certain fault severity when a specific issue is detected. Different types of CM technologies are defined based on which fault indicating parameters are measured, e.g. temperature, vibration, sound, stator current and stator flux. The nowadays most implemented and reliable CM technology is by far *Vibration analysis*. The working principle and diagnostic methods are very similar to periodic maintenance, but now on a continuous basis. Based on specific fault related signatures that can be detected in the machine vibrations, faults e.g. rotor unbalance, bearing faults and misalignment can be identified. However, as the relatively sensitive accelerometers are permanently placed in the harsh industrial environments (temperature swings, large impacts, excessive vibrations, dust, moist), this technology remains quite expensive and requires high maintenance e.g. remounting the sensors, sensor recalibration, broken wiring, cleaning... Consequently, only machines with a sufficiently high criticality index really benefit the implementation of this predictive maintenance strategy using vibration analysis.

Proactive maintenance is applied when, after determining the root cause of a failure, all attempts are made in order to avoid future failures with the same cause. This strategy of maintenance can be combined with previously mentioned strategies following by the RCFA. Different levels of feedback and improvements can be defined because it can apply on either the machine, on the mounting structure, on the maintenance team (e.g. greasing bearings)... In proactive maintenance, it rarely happens that the electrical machine itself should be re-dimensioned. Most of all, it regards changes on the mounting structure, correct alignment, proper balancing of the rotors... Consequently, once the machine has successfully served for a couple of years, no proactive maintenance is performed anymore. This type of maintenance strategy is usually applied for new, (re-)initialized machines and their power trains.

1.2 Problem statement

This research considers the application of condition monitoring as a predictive maintenance tool for asynchronous induction machines defined as critical. Furthermore, not vibrations, noise or temperature, but the machine stator current is used in order to detect specific faults in electric machines. Analyzing the stator current, commonly addressed to as Motor Current Signature Analysis (MCSA), has some serious advantages compared to vibration analysis regarding the additional detection of electrical faults, costs of installation, robustness, interference of sensors, machine accessibility... This comparison with respect to other technologies is extensively handled in Chapter 2. Unfortunately, this technology remains unvalorizable in the market of condition monitoring. This partially because MCSA can only cover the electric machine, without being able to state the condition of the full drive train. Nevertheless, the main disadvantage of the current MCSA-algorithms is the lack of information on the exact relation between occurring mechanical faults and their reflection in the stator current [2, 13]. Although every kind of mechanical fault can easily be detected and identified in the stator current, the severity of that fault is hard to estimate. This is mainly due to the complex transition path between the fault and its reflection in the current. The exact analytical derivation of this transition path will not be obtained in this research for an IM due to the complexity of the combined integrals (two spatial integrals and one time integral). However, a strongly simplified fault-transition is illustratively used. The mechanical transition path is defined by approaching the foundation/stator/rotor as a Two-Degree-Of-Freedom (2DOF) model, Figure 1.2. The electrical transition consists of a simplified electric machine with only one connected, concentrated winding and a plain cross-section of the rotor, Figure 1.3. The mechanical fault can be represented by a specific force working onto the rotor of the machine, extensively elucidated in Chapter 4. This vertical force $h_y(t)$ due to the mechanical fault is related to the rotor movement by the equation of motion (obtained using Figure 1.2):

$$\begin{cases} h_y(t) = m_r \cdot \ddot{y}_r(t) + c_r [\dot{y}_s(t) - \dot{y}_r(t)] + k_r [y_s(t) - y_r(t)] \\ 0 = m_s \cdot \ddot{y}_s(t) + [c_s + c_r] \dot{y}_s(t) - c_r \cdot \dot{y}_r(t) + [k_s + k_r] y_s(t) - k_r \cdot y_r(t) \end{cases} \quad (1.1)$$

with: m_r and m_s the equivalent mass of the rotor and the stator; k_r and k_s the equivalent stiffness of the rotor and the stator; c_r and c_s the equivalent damping of the rotor and the stator; \ddot{y}_r , \dot{y}_r , y_r and \ddot{y}_s , \dot{y}_s , y_s the respectively acceleration, velocity and displacement of the rotor and the stator. It can be noticed that the acceleration $\ddot{y}_s(t)$ is in fact the signal which is being measured by performing vibration analysis (acceleration measurement on the stator housing).

The inevitable fault-imposed movement between the rotor $y_r(t)$ and the stator $y_s(t)$ creates a specific air gap variation defined as:

$$a(t) = \bar{a} + y_r(t) - y_s(t) \quad (1.2)$$

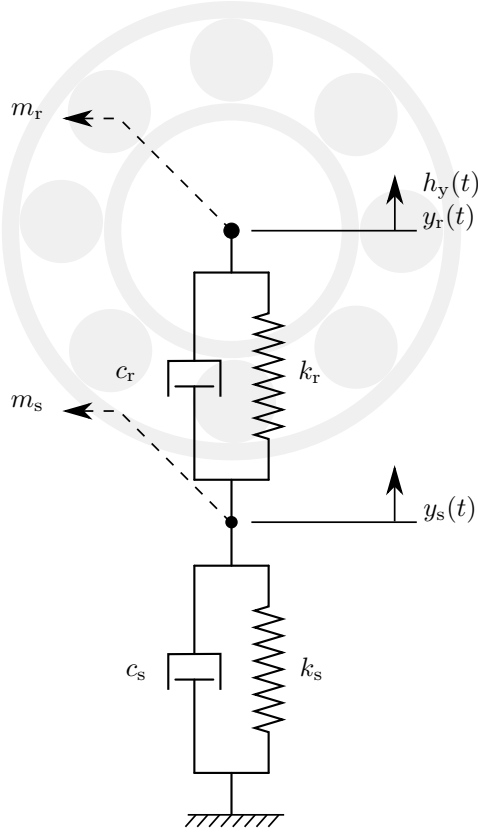


Figure 1.2: The simplified model of the rotor, stator and foundation for the vertical direction

with \bar{a} the mean spatial air gap between the rotor and the stator-poles. This variation results in a change of reluctance path $\mathcal{R}(t)$ between the stator and the rotor, described as [32]:

$$\mathcal{R}(t) = \frac{l_{\text{stat}}}{\mu_{\text{stat}} \cdot \mu_0 \cdot A_{\text{stat}}} + \frac{a(t)}{\mu_0 \cdot A_{\text{air}}} + \frac{l_{\text{rot}}}{\mu_{\text{rot}} \cdot \mu_0 \cdot A_{\text{rot}}} \quad (1.3)$$

with: l_{stat} , l_{rot} the length of the flux-path through respectively the stator and the rotor; A_{stat} , A_{rot} , A_{air} the cross sectional surface of the flux-path through respectively the stator, the rotor and the air gap; μ_0 the permeability of air and μ_{stat} , μ_{rot} the relative permeability of respectively the stator and the rotor. This changing reluctance imposes a change in inductance $L(t)$, described in [32]:

$$L(t) = \frac{n^2}{\mathcal{R}(t)} \quad (1.4)$$

with n the number of turns in the stator winding. Lastly, the unique change of

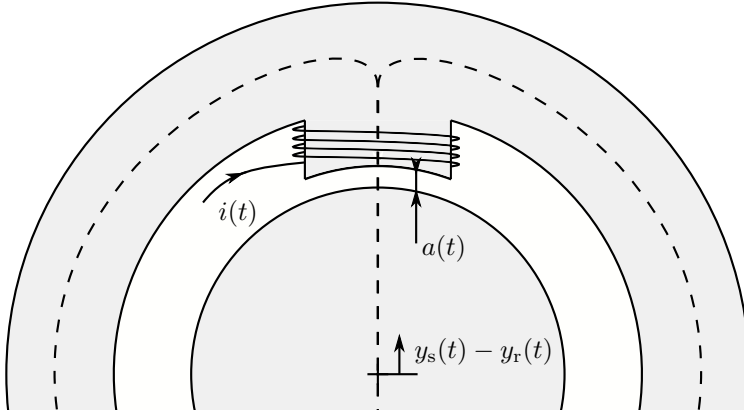


Figure 1.3: The simplified model of the electric machine

inductance due to the faulty rotor-movement implies a modulation of that fault signature on the fundamental stator current component, detectable in the stator current $i(t)$, described by following [13,33]:

$$v(t) = e(t) + R \cdot i(t) - \frac{dL(t) \cdot i(t)}{dt} \quad (1.5)$$

with: R the stator resistance; $e(t)$ the voltage on the T-equivalent parallel elements and $v(t)$ the grid-voltage connected to the electric machine. This simplistic derivation describes the transition of the mechanical fault to the modulated signatures in the stator current. It must be noticed that this sequence of propagation can be translated to a real induction machine. However, these simplified equations can not be used due to the distributed windings and the rotor-complexity. Additionally, this path is difficult to quantify analytically as it is highly depending on the machine operation state, temperature, power quality. . . Conclusively, this complex mechanical fault-propagation obstructs the straight-forward quantification of mechanical faults and their reflection in the stator current.

As a CM technology can only be effective when a certain severity estimation can be determined when a specific fault is detected, stator current analysis remains less of value as a full CM technology. Comprehensibly, because the operator of the monitored machine has less information with a message such as “*There is a problem*” with respect to a message stating “*The machine should be shut down within an hour*” or “*There is a problem, but it will keep running for another few years*”. Therefore, this research is fully focused on elucidating the relation between evolving mechanical faults and their corresponding reflections in the stator current. If that relation is characterized thoroughly, stator current analysis can be used as a complete and reliable CM technology. In order to characterize that relation, four main research approaches are possible: analytical modeling, multi-domain simulation, finite element modeling and experimental research. As been showed in previous analytic derivation of the fault transition, obtaining a representative analytical

model under varying air gap is a complex matter. The combination of two spatial integrals (one due to the distributed field and one due to the changing air gap) and one time integral was too complex to handle in this research. Nevertheless, future cooperation with expertized research-groups can lead into the construction of these simulation models. The possibilities of multi-domain modeling in this approach was very limited as in the packages considered in this market survey did not allow the constructional modifications of the standard models for electrical machinery (ref: *MapleSoft*, *Siemens PLM Software*, *Simscape Multibody* and *AMET*). Even the available finite element modeling software (*Cedrat - Flux 2D* and *Comsol*) did not allow to simulate a changing rotor-position with respect to the stator in a transient, obstructing the exact fault propagation to the stator current. Due to the mentioned limitations of the nowadays simulation platforms/models, the most conceivable way in investigating the mechanical fault propagations towards the stator current is via the experimental approach [22, 23, 34]. Consequently, this approach will be applied in this research.

To obtain reliable results in this experimental approach, a reproducible method is needed in order to emulate quantified mechanical faults in electrical machinery. This emulator should be able to emulating bearing faults as these remain the majority of direct and indirect causes of premature failures. Many authors have been searching for an easy way to emulate those faults in electric machines within academic environments with reproducibility and relevance to industrial applications (mainly bearing related) [13, 22, 23, 34–38]. For now, e.g. emulating bearing faults in electric machines remains difficult, time-consuming and imprecise [2, 23, 38]. The widely used method is replacing one of the machines bearings by a bearing with an artificial implemented fault [22, 34, 35, 37, 38]. Inevitably, reproducibility is already lost by remounting the bearing due to the fact that the total systems characteristics such as stiffness and damping are highly depending on the bearings mounting. Additionally, the way faults are enforced on to the bearing are often very different in respect to the actual faulty situation. For example, mechanical outer race pitting is usually emulated by drilling holes of different sizes in the outer race, which should present several severity stages. Unfortunately, those artificially implemented faults are hardly relevant to real evolving mechanical pitting as the shape of the drilled hole does not corresponds to real mechanical pitting (see Chapter 4). As this research wants to focus on the development of detecting mechanical faults in electric machines based on stator current measurements, building a novel accurate mechanical fault emulator is essential. When the fault emulator is built, finding relations between the fault severity and the stator current fault signature under different environmental influences will be feasible. Subsequently, stator current analysis as a condition monitoring technology can be considered as feasible.

1.3 Research goal

The main goal of the overall research regarding the application of stator current analysis as a CM technology can be stated as follows:

“Avoiding premature unexpected failures of electrical machines installed in industrial production processes by measuring and analyzing electrical current. This is done by identifying any incipient cause of failure with a corresponding prediction of a time-to-failure.”

It must be noticed that this is the final goal in the overall research on using the stator current analysis as a complete and reliable CM technology. The achievement of that overall goal in this thesis would be too ambitious and lack specific actions and steps towards that direction. As a consequence, the goal of this research is defined and described by the following four sequential subgoals:

1. Being able to measure, distinguish and analyze with a sufficient accuracy fault related components in the stator current (Chapter 3).
2. Defining the shape and impact of every kind of evolving mechanical fault on the behavior of an IM, especially bearing faults (Chapter 4).
3. Building a test-rig which can emulate all kind of mechanical evolving faults on an IM with high relevance to real applications (Chapter 5).
4. Finding specific quantified relations between the emulated mechanical faults and the stator current as a function of fault-severity (Chapter 6).

First, as goal one describes, this research starts by being able to measure the stator current and finding fault related components. This is not the main scientific challenge of this dissertation, but can nevertheless not be neglected. With the scope on the application, the measurement and analysis topology should be considered to be rather cheap, accurate, convenient, easy to install... The second goal is more challenging and purely analytical. As the impact of mechanical faults on IMs is to be investigated, the mechanical fault should be defined and characterized completely. More specific, the impact of the fault on the machine has to be defined as a function of bearing type, speed, torque, machine topology, fault severity... This has not been addressed to in literature as only in this specific research approach it is opportune to calculate the specific rotor-movements imposed by mechanical faults. Consequently, this goal handles to most innovative aspect of this thesis. The third goal is a challenge in engineering. A mechanical fault emulator should be build which induces the previously defined faults in a real IM with the focus on accuracy and reproducibility without neglecting the industrial relevance. Although this goal is less scientific and more technical, this goal results in obtaining a very unique mechanical fault-emulating test-rig. The possibilities go way beyond the application of MCSA, as it can as well be used in the development of CM-systems based on vibration analysis. When the first three goals are obtained, the fourth one can be handled. Finding and quantifying the reflections in the stator current

with respect to the severity of the emulated fault. This will result in the first reproducible quantifications of varying mechanical fault-severity and its effect on the corresponding current signatures. By succeeding in this research, MCSA will be a huge step closer to be applicable as a complete and reliable CM technology.

1.4 Approach

Most of the mechanical faults that occur in an electric machine can be related to specific movements of the rotor in relation to the stator (bearing faults, rotor unbalance, misalignment) [2, 13, 39]. This is how the mechanical faults propagate to the stator windings in the first place. Therefore, emulating a mechanical fault in an electric machine could be done by controlling the position of the rotor in relation to the stator with high precision. In order to do so, replacing one of the mechanical bearings of the machine by an Active Magnetic Bearing (AMB) can impose the fault related rotor/stator displacement (conceptually presented in Figure 1.4). Additionally, the AMB has the advantage that the stiffness and damping characteristics of a mechanical bearing can be implemented in the control loop. Consequently, the IM can operate with the AMB as it did with the original bearing. Furthermore, the AMB's flexibility implies that the system characteristics e.g. motor torque and speed remain constant while several mechanical faults are emulated. As the machine does not have to be shut-down to imply evolving mechanical faults, the relation between the fault-severity and its reflection in the stator current can easily be investigated under different operational conditions. With these results, the exact impact of any mechanical fault on the stator current will be evaluated and quantified.

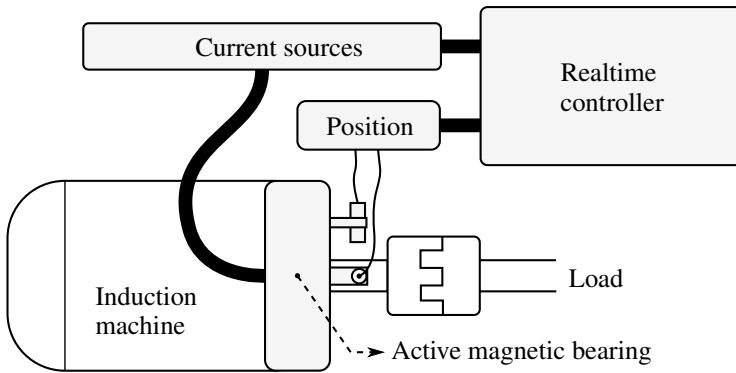


Figure 1.4: Replacing the mechanical bearing by an active magnetic bearing enables the ability of inducing fault related rotor movements

In Chapter 2, an overall review is presented on the usage of condition monitoring in general, completed with the state of the art of using stator current analysis as a condition monitoring technology. This chapter includes a clear presentation on how different fault signatures can be found in the stator current. Subsequently, Chapter 3 focuses on the signal processing aspects of performing current analysis, more specific, measurement techniques and analyzing methods. Crucial processing steps e.g. digital signal processing and frequency transform algorithms are specified in order to obtain an accurate representation of the machine fault diagnosis. The origin and relation between all kinds of mechanical faults and the time

based position of the rotor with respect to the stator is analytically determined in Chapter 4. The use of fault related impulse functions and the simplification of the rotor/stator system as a two degree of freedom mass/spring/damper system results in a unique analytical model which is capable of calculating the rotor positions for any faulty condition. This is mandatory for an easy and accessible fault emulation. Ineluctably, the obtained movements are validated by Multi-body modeling and an industrial test case. In Chapter 5, the novel approach is presented being the emulation of mechanical faults on an 11kW IM with the use of an AMB. That AMB is dimensioned on both static and dynamic requirements including finite element analysis and extensive simulation, mainly based on the results of Chapter 5. During dimensioning, full attention is given to the functionalities of the original mechanical bearing in order to obtain representative and reproducible emulations. The total AMB system from sensor sockets to designing the control system is dimensioned and described extensively. As a result, the unique test-rig is constructed which can emulate all kinds of predefined mechanical faults on a reproducible way. Conclusively, as this is the core of this research, the relations between the emulated faults and the reflections in the stator current are presented in Chapter 6. Using the method of the least squares, the change in stator current due to the imposed mechanical faults is quantified with a strong correlation. Overall conclusions and a view on future research are presented in Chapter 7.

1.5 Publication list Bram Corne

1.5.1 Journal publications

- [1] B. Corne, B. Vervisch, S. Derammelaere, J. Knockaert and J. Desmet. *Emulating Single Point Bearing Faults with the use of an Active Magnetic Bearing*. IET Science Measurement & Technology, Accepted for publication in september 2017

1.5.2 Conference publications

- [2] B. Corne, C. Debruyne, P. De Baets and J. Desmet. *Stator current measurements as a condition monitoring technology — The-state-of-the-art*. pp. 1659-1665, IEEE International Conference on Electrical Machines (ICEM), Berlin, 2014.
- [3] B. Corne, B. Vervisch, C. Debruyne, J. Knockaert and J. Desmet. *Comparing MCSA with vibration analysis in order to detect bearing faults - A case study*. pp. 1366-1372, IEEE International Electric Machines & Drives Conference (IEMDC), Coeur d'Alene, 2015.
- [4] C. Debruyne, B. Corne, P. Sergeant, J. Desmet and L. Vandeveld. *Evaluation of the additional loss due to supply voltage distortion in relation to induction motor efficiency rating*. pp. 1881-1887, IEEE International Electric Machines & Drives Conference (IEMDC), Coeur d'Alene, 2015.
- [5] B. Corne, J. Knockaert and J. Desmet. *Emulating bearing faults - A novel approach*. pp. 2223-2229, IEEE International Conference on Electrical Machines (ICEM), Lausanne, 2016.
- [6] B. Corne, B. Vervisch, S. Derammelaere, S. M. A. Cruz, J. Knockaert and J. Desmet. *Single point outer race bearing fault severity estimation using stator current measurements*. pp. 2642-2649, IEEE International Electric Machines & Drives Conference (IEMDC), Miami, 2017.

- [7] C. Debruyne, P. Sergeant, B. C. J. Rens and J. Desmet. *Modeling and validation of losses due to unbalanced loading of stand-alone generators*. pp. 3574-3580, IEEE International Electric Machines & Drives Conference (IEMDC), Miami, 2017.
- [8] B. Corne, J. Knockaert and J. Desmet. *Misalignment and Unbalance Fault Severity Estimation using Stator Current Measurements*. pp. 1966-1973, IEEE Symposium on Diagnostics for Electric Machines, Power Electronics and Drives (SDEMPED), Tinos, 2017.

1.5.3 Other publications

- [9] J. Desmet, J. Knockaert, C. Debruyne, C. Vansteenberge, B. Corne, B. Verhelst and B. Vanseveren. *Invertor/batterij systemen*. pp. 18-21, Elektrotechnisch Ingenieur: Belgotronic, Belgium, 2014.
- [10] J. Desmet, J. Knockaert, P.Sergeant, B. Corne, C. Debruyne, S. Dereyne, J. Descheemaeker, L. Hespel, C. Vansteenberge and B. Verhelst. *Laagspanningsinstallaties: technologie en ontwerp*. Book - Lemcko, Kortrijk, Belgium, 2015.
- [11] B. Corne and J. Desmet. *Nulgeleiderstromen in laagspanningsinstallaties*. pp. 14-20, Elektricien, Belgium, 2016.

2

A review on Condition Monitoring with Motor Current Signature Analysis

2.1 Introduction

In this chapter, the current state-of-the-art on several Condition Monitoring (CM) techniques is described based on a thorough literature study. This study focuses on the differentiation of Motor Current Signature Analysis (MCSA) with respect to the main monitoring techniques applicable on electric rotating machinery. First, a brief overview on the main CM-technologies applicable on electric rotating machinery is presented in §2.2. From thereon, the added value of performing current based monitoring will be elucidated together with its disadvantages. The subsequent section, §2.3 is focused on the existing literature on MCSA and its algorithms. The reflections of electrical and mechanical faults of different origins towards the stator current are characterized by formulas. Additionally, several techniques are presented which facilitates the extraction of valuable information out of stator current measurements. This chapter is conclusively purely based on literature without containing any novel or contributed material to the field of CM with MCSA.

2.2 Condition Monitoring technologies

Predictive maintenance is a strategy which evaluates the good condition of the machine in order to estimate and ensure the machine stable operation in the future. As soon as that condition is threatened, appropriate actions should be undertaken. The process from continuously capturing the machine fault indicating signals to performing the exact evaluation of the condition and subsequently reporting to the machine operator is generally referred to as *Condition Monitoring* (CM). Every machine signal or parameter which can give an indication about the electric machine condition can be used. The most used and applied technologies regarding the monitoring of electric rotating machinery are based on temperature, vibration, noise, electric current. . . The CM system is responsible to detect certain machine problems which can lead into an unexpected failure. Additionally, the system should provide an estimation of the remaining or secured life-time. Of course, not every CM technology can provide the same in depth analysis on component level. For example, a classic thermal protective circuit breaker can be seen as a very basic way of applying CM. As soon as the temperature in the machine stator windings is exceedingly high, the machine is shut down in order to prevent further collateral damage. Nevertheless, in this dissertation and basically in most literature, CM is seen as an advanced way of fault diagnosis and failure prediction, covering the needs in performing predictive maintenance. As a lot of CM technologies with various gradations in complexity and effectiveness can be applied, commonly based on the critical role of the machine within the economic productivity of the company (not on the technique). As discussed in the previous chapter, the criticality index can provide a benchmark in order to determine the requirements of the CM technology. In the following section, the most applied technologies based on temperature, vibration and noise are briefly discussed in order to situate stator current analysis as a CM technology.

The most basic and straightforward CM technology is based on **temperature analysis**. The majority of the listed root causes in Table 1.1 imply a direct increase of the machine temperature. This increase in temperature can not only be a consequence of mechanical wear, but as well due to the loss of efficiency when certain faults are occurring. Therefore, by monitoring the machine overall temperature, a basic CM technology is established. As a consequence, many produced IMs are already equipped with a built-in thermocouple located in the stator windings. By installing a motor overcurrent protection device featured with a thermocouple input, the IM can be automatically disconnected from the voltage grid when an alarming winding temperature is reached. Unfortunately, this basic, simple and cheap way of condition monitoring is not able to distinguish between different propagating faults in the IM. Estimating an accurate severity of the fault is consequently inconceivable. A more advanced method of applying temperature analysis is the use of frequently taken infrared images of the IM, commonly referred to as thermal imaging. In this way, a visual determination can be made of the location of the fault related heat-sink. An example of these types of measurements is pre-

sented in Figure 2.1, which is respectively a case of a 4kW IM with outer race bearing-problems at Drive-End (DE) side and a 35kW IM severing lubrication contamination [1]. Following [40], only in combination with an advanced thermal model, temperature analysis has the potential to become a comprehensive CM tool. However, [41] showed the added value of machine learning techniques in this analyzing process, avoiding the need of advanced thermal models. This expensive way of monitoring is commonly applied where vibration analysis is very difficult, such as: machines severing excessive vibrations (e.g. compressors, combustion engines), structural movements (e.g. several interacting drive-trains on the same foundation) or very low speed machines (e.g. direct shaft-connected multi-pole generators in wind turbines) [40,42].

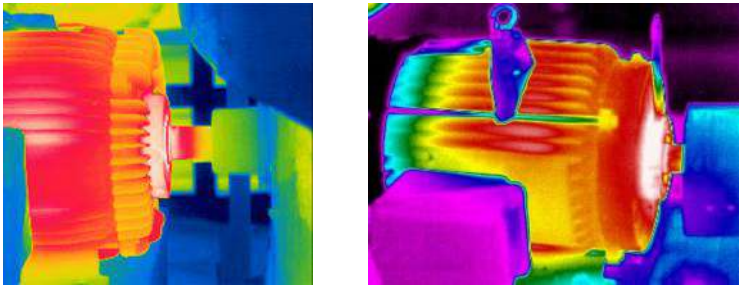


Figure 2.1: An infrared temperature analysis of two IMs severing bearing problems [1]

For now, the most reliable, advanced and commercially applied CM technology is undoubtedly **Vibration analysis**. Vibration analysis on IMs is performed by measuring and analyzing the vibrations of the machine stator housing. A rather simple form of vibration analysis is following the ISO 10816 (previously ISO 2372) Vibration Severity Standard [5] in which the Root Mean Square (RMS) velocity of the machine housing is used as a condition indicator. The RMS velocity is calculated between 10Hz and 1kHz. The resulting value is classified in the standard based on defined alarming limits, depending on the machine size and mounting strategy following Table 2.1 with corresponding zone classification, [5]:

- A: The vibration levels of newly commissioned machines is normally located within this zone.
- B: Machines with vibration levels within this zone are normally considered acceptable for unrestricted longterm operation.
- C: Machines with vibration levels within this zone are normally considered unsatisfactory for long-term continuous operation. Generally, the machine may be operated for a limited period in this condition until a suitable opportunity arises for remedial action.
- D: Vibration levels within this zone are normally considered to be of sufficient severity to cause damage to the machine.

This procedure results in an very rough and vague overall condition indication of the machine as it does not provide any information about the origin of the fault. Therefore, in most cases, this way of performing vibration analysis is insufficient. Furthermore, the magnitudes of the RMS velocity are influenced by various environmental conditions e.g. structural stiffness, adjacent machines or machine functionalities. The interpretation of the vibration magnitude following above categorization is usually imprecise. Mostly, the RMS velocity is logged and compared to the values during initialization. Only when a significant change of magnitude with respect to the initial healthy condition is stated, the operators are alarmed. Inevitably, any kind of fault related prediction is excluded in this way of analyzing vibrations.

Mounting class	Zone boundary	RMS velocity [mm/s]
Rigid	A/B	2.3
	B/C	4.5
	C/D	7.1
Flexible	A/B	3.5
	B/C	7.1
	C/D	11.0

Table 2.1: Classification of vibration severity zones for machines of Group 1: Large machines with rated power above 300kW and not more than 50MW; electric machines with shaft height $\geq 315\text{mm}$, [5]

In order to obtain a more accurate and useful vibration analysis, the spectral content of the vibration signal can be analyzed. Faults such as mass-unbalance or single point bearing faults generate a specific vibration signature, propagated through the stator housing to the accelerometers. The specified characteristic fault frequencies that are detectable with vibration analysis and their specific frequency are listed in Table 2.2 [5, 13, 43, 44].



Figure 2.2: Measurement devices for performing advanced vibration analysis

IM problem	Frequency
Rotor eccentricity	$k.f_r$
Bearing inner race	$k.f_r \frac{n_b}{2} \left(1 + \frac{bd}{pd} \cos \beta \right)$
Bearing outer race	$k.f_r \frac{n_b}{2} \left(1 - \frac{bd}{pd} \cos \beta \right)$
Bearing cage	$k.f_r \frac{1}{2} \left(1 - \frac{bd}{pd} \cos \beta \right)$
Bearing ball	$k.f_r \frac{pd}{2.bd} \left(1 - \left[\frac{bd}{pd} \cos \beta \right]^2 \right)$

with f_r , the rotor speed; $k = 1, 2, 3 \dots$, number of bearing balls n_b , bearing ball diameter bd , bearing pitch diameter pd and bearing contact angle β .

Table 2.2: IM vibration fault frequencies

It can be noticed that only rotor eccentricity and bearing problems are included in the basic diagnosis on electric machinery. However, recent vibration analyzing tools are even able to implement a detection algorithm for electrical problems [45, 46]. This CM technique is widely used and applied in the industry by commercial monitoring devices. Mostly, the measuring device generates a frequency spectrum of the measured data and the user calculates and searches for the fault frequencies in the spectrum. Although, more advanced devices as in Figure 2.2 automatically indicate all fault-related forcing frequencies in the spectrum. Nevertheless, the interpretation of the magnitudes of the spectral content is usually done by the vibration expert. The measurement device rarely indicates a specific severity estimation or reliable MTTF/MTBF. In practice, the vibration spectra is usually logged during initialization and/or start-up in order to be able to compare future measurements with the 'good condition'. As will be shown further in this dissertation, the relative change in magnitude of specific fault components is usually more informative than the absolute magnitude from a single measurement.

Regarding bearing related faults, several techniques are available to detect these type of faults in a very early stage of severity (e.g. envelope spectrum, shock pulse method, spike energy, Kurtosis...) [42, 43, 47]. These techniques are essential, as the presence of the characteristic bearing related components (listed in Table 2.2) in the low frequency spectra already indicates a severe stage [1]. This due to vibration analysis is measuring acceleration of the stator housing. Consequently, only when the bearing fault is large enough to propagate as a movement of the stator housing, it is visualized in the low frequency region [5]. An illustrative example of a vibration spectrum with some highlighted fault indicated components is presented in Figure 2.3. That measurement was performed on a 250kW IM im-

plemented in an industrial production plant which will extensively be discussed in §3.4.3. In some cases not only the vibrations are analyzed in the frequency domain but as well in the time domain, especially in detecting faulty conditions of the drive train e.g. pump cavitation, gearbox fault frequencies or magnitude modulation [5].

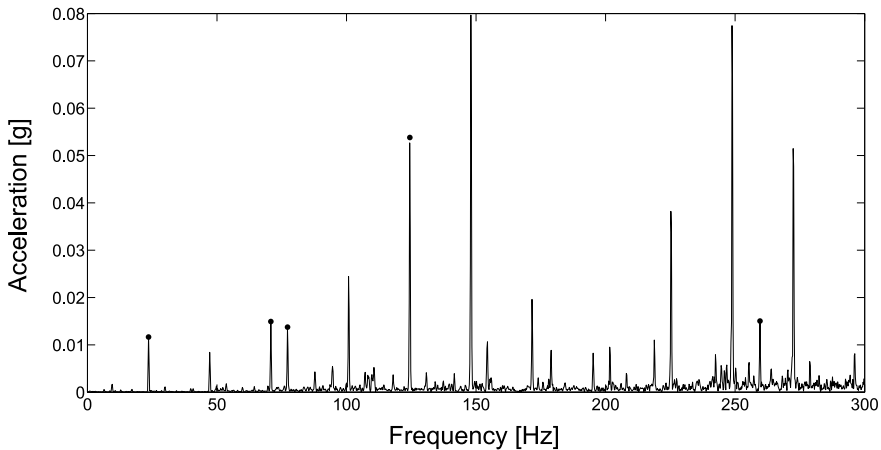


Figure 2.3: Example of a fault-indicating vibration spectrum with highlighted fault frequency components performed on the DE side of a 2 pole pair 250kW, 50Hz, 1416rpm IM, case study discussed in §3.4.3

The evolved industrial experience in vibration analysis has made this technique the most applied method in performing advanced CM, diagnosing machines on component level. This resulted in the convenient but rather simple ISO 2372-standard, widely used as backbone for vibration experts worldwide. Nevertheless, it remains a relatively expensive technology as an investment and in maintenance. This mainly due to the expensive and sensitive accelerometers. Thereby, only for machines with a sufficiently high criticality index, this way of performing CM is applied.

Acoustic analysis is in essence very similar to vibration analysis. With the use of microphones, the machine vibrations can be measured and analyzed in the frequency domain. Frequency based fault components are propagated exactly the same as presented in Table 2.2. It is comprehensible that this kind of analysis is more subjected to interferences in comparison to vibration analysis. When measurements are performed in a noisy environment, the analysis is easily disturbed and wrongly interpreted. However, in terms of detecting bearing faults in a premature severity stage, ultrasonic acoustic analysis is a very useful methodology, [1]. Due to the ultra high-frequency noise produced by incipient bearing wear, it can be detected by acoustic analysis very prematurely with respect to vibration and/or temperature analysis [1]. Usually, only one ultrasonic measurement device is acquired per industrial facility in order to manually measure all installed machines on a periodic basis. As detecting incipient bearing wear is the only significant ad-

vantage of acoustic analysis in monitoring electrical rotating machines, no further attention is given to this CM technology.

The technology that has a lot of functional similarities with vibration analysis and even nullifies some of its disadvantages, is the condition monitoring system based on **stator current analysis** or generally referred to as Motor Current Signature Analysis (MCSA). This CM system measures current through the stator windings in the assumption that most direct and indirect problems which can lead to an unexpected failure can be detected. MCSA has some significant advantages with respect to the most applied CM technology, being vibration analysis. First of all, MCSA is able to detect electrical and mechanical malfunctions which strongly increases the reliability of the CM system. Secondly, the sensors (e.g. current transducers) are by far more robust compared to accelerometers both on electromagnetic interferences and on environmental condition [13, 48]. Furthermore, as in modern applications frequency drive systems are used, the current sensors are already implemented in a drive system which implies that MCSA can be nothing more than a software integration. This reduces the cost of implementation MCSA significantly. Additionally, most of the drive systems are connected to a data communication network, which makes it easy to remotely activate, control and communicate with the MCSA monitoring system. Another significant advantage is that, due to measuring currents, no access is needed to the machine itself, but only to its feeding cables. This is an interesting point in rough and hardly accessible environments e.g. wind turbines or submersible pumps. These arguments illustrate the interest towards MCSA as a condition monitoring technology. Although, it must be noticed that making a correct and interpretable signal analysis of the current is a huge challenge [2]. Table 2.3 presents a comparison of the main (dis)advantages of using MCSA in reference with vibration analysis. The difference between the check-mark and cross-mark does not indicate the exclusion, but indicates the advantage of the one technology with respect to the other.

	Current	Vibration
Easy radial rotor displacement interpretation	✓	✗
Detecting electrical faults	✓	✗
Applicable in rough environments	✓	✗
Rather cheap implementation	✓	✗
Distinguish between several bearings in drive train	✗	✓
Experience in severity estimation	✗	✓
Favorable signal to noise ratio	✗	✓

Table 2.3: MCSA compared to Vibration analysis, [2]

MCSA relies specifically on the IM as a sensor which is an interesting way of measuring. As presented in §1.2, the path from mechanical faults to the stator current is via the air gap. As soon as a mechanical fault occurs, mostly a specific movement between the rotor and the stator is imposed. That radial movement of the rotor in the stator leads to a change of air gap between the rotor and the stator. Magnetically seen is this nothing more than a specific change in the reluctance path. Consequently, a change in the stator inductance is created. That change in inductance $L(t)$ implies a modulated signal on the stator current $i(t)$, following [33]:

$$v(t) = e(t) + R \cdot i(t) - \frac{dL(t) \cdot i(t)}{dt} \quad (2.1)$$

with: R the stator resistance; $e(t)$ the voltage on the T-equivalent parallel elements; and $v(t)$ the grid-voltage connected to the electric machine. This is how mechanical faults are propagating towards the stator current. Generally speaking, stator current analysis is actually measuring the displacement of the rotor with respect to the stator [2, 13, 39, 49]. This is a huge advantage with respect to vibration analysis, where only the acceleration of the stator housing is measured. Moreover, it will be shown throughout this research that in terms of detecting premature bearing faults, the difference between measuring displacement and acceleration can be decisive. For example, a bearing cage malfunction creates a relatively low-frequency movement of the rotor, where a minimal force (acceleration) is generated. By consequence those faults are detectable through MCSA where vibration analysis fails. Additionally, measuring the vibrations of the stator housing is highly subjected to the machine constructional dimensions, framework, measurement location, adjacent machines. . . Nevertheless, vibrations can be measured through the entire drive train, all mechanical components can be monitored. With stator current analysis, only the electrical machine can be monitored. In applications where the whole drive-train should be monitored, multi-sensor analysis is performed, being the combination of MCSA with vibration analysis. The last statement in Table 2.3 expresses the favorable Signal to Noise Ratio (SNR). Generally, the SNR in vibration measurement is much higher than in MCSA. The current spectrum is not only corrupted by noise, but also by numerous harmonic components resulting from the regular magnetic behavior of an IM (certainly drive-fed). The biggest challenge for the practical implementation of MCSA is to measure and distinguish the spectral fault signatures from the other components and noise, located very close to and possibly faded with each other. Although, by using an accurate frequency/magnitude resolution and the correct signal processing methods it will be shown that mechanical faults are clearly distinguished among other components. However, achieving an accurate frequency transformation is for both MCSA and vibration analysis a crucial point of the signal analysis. As a conclusion, this section shows the potential of using MCSA as a reliable condition monitoring technology with respect to the current advanced CM technologies. Due to these significant advantages this research is conducted in order to obtain a more complete, more reliable and less expensive CM technology.

2.3 Motor Current Signature Analysis

According to [14–17], 40% of the unexpected electric motor failures are indirectly related to bearing issues, 38% to stator errors, 12% to rotor failure and 10% to other failures such as accidents. In order to obtain an effective CM system based on MCSA, the system should be able to detect the majority of these categorized problems before total machine failure occurs. Consequently, two important questions should be answered:

1. Are the most common occurring and evolving machine problems affecting the electrical current?
2. How can these problems be detected in the machine current in a premature stage before the machine actually fails?

Apart from the technical difficulties and scientific challenges, it is plausible and relatively straightforward that electrical stator (e.g. winding breakdown), electrical rotor (e.g. broken rotor bar) or electrical bearing problems (e.g. bearing currents) are detectable by analyzing the stator current. However, because the majority of unexpected failures find their root cause in mechanical problems (Chapter 1), mechanical faults should be detected as well in order to obtain an effective CM system. The link between mechanical problems and the electrical current is not straightforward and should be addressed in detail. As will be extensively shown in Chapter 4, the majority of mechanical faults could be described as a specific rotor movement with respect to the stator. Due to that radial rotor movement, the air gap between the stator and rotor varies uniquely according to the specific fault. This implies a change of the magnetic reluctance and so a change in inductance. As this imposed variation affects the stator inductance, the fault signatures in the stator current are inevitably modulated on the fundamental stator current component. In order to extract the information related to motor faults from the stator current, the signal is generally analyzed in the frequency domain. This because most faults generate a very unique frequency related pattern [2, 13, 15, 25, 39, 49–51]. The analysis separates the current into a summation of components with their own frequency, magnitude and phase shift. An example of a current measurement and its frequency analysis can be found in Figure 2.4a respectively Figure 2.4b. MCSA is usually applied by evaluating the stator current in the frequency domain and relating certain fault related frequency components to specific problems in the machine. The magnitude and the differential change in magnitude of those monitored components is commonly used to estimate a certain stage of severity [15, 25, 50, 51]. However, in order to obtain a good evaluation of a fault signature in the stator current, it is important to clearly distinguish between different fault related components and their origin. Next sections will address the most common electrical and mechanical faults together with the way they appear in the stator current. This information, basically known for decades, is essential in further research within this thesis. It must be noted that the elucidated signatures are fully frequency based. The magnitude and severity of the specific faults are poorly discussed in literature,

especially for mechanical faults. Furthermore, some researchers showed thereby the uselessness of MCSA, as no relation could be found between the severity of the mechanical faults and the magnitude of the faulty current components [52]. It is partially due to this literature study and findings that the problem statement and research goals of this dissertation were defined. The following sections of this chapter present the state of the art of MCSA in order to position this research in the overall evolution of MCSA as a CM technology. Three main categories of signatures are defined: stator, rotor and bearing related.

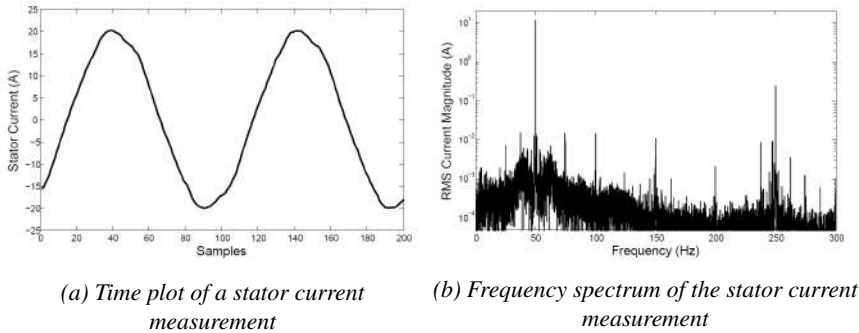


Figure 2.4: General MCSA-algorithms indicate the faulty signatures in the stator current via spectral analysis

2.3.1 Stator signatures

Fortunately, the main causes and the related effects for stator failure have been extensively addressed by other authors in [1, 17, 31, 53–55]. The effort of those authors resulted in the establishment of MCSA-algorithms which are able to detect, identify and estimate the fault severity of stator related faults out of the stator current. As a consequence, this research is not focused on those faults as they are already elucidated thoroughly. Nevertheless, they are included in the final diagnostic MCSA-algorithms. This in order to obtain a complete CM system which is applicable towards the industry. Conclusively, it can be stated that stator errors are commonly noted as stator winding short-circuits, with further categorization as inter-turn, phase-to-phase, phase-to-neutral and phase-to-ground faults. Examples of these types of short-circuits can be found in Figure 2.5. The root cause of these faults can be localized in the following main stresses:

- thermal stress caused by mechanical/electrical overload, electrical unbalance or voltage distortion;
- electrical stress caused by partial discharge which is generally linked to a high dv/dt imposed by frequency inverters;
- environmental stress caused by dirt, moisture, Electro-Magnetic Compatibility (EMC);

- mechanical stress and vibrations caused by manufacturing/installation errors such as misalignment or sloppy bearing placement.

The main cause of winding failure observed by performing services to the industry are the electrical stresses. The winding insulation behaves as a parasitic capacitance to the grounding. When frequency converters with PWM (Pulse Width Modulation) are used, voltages with high dv/dt properties are applied on the machine windings. A high dv/dt means high-frequency voltage components. As the impedance of the parasitic capacitor is inversely proportional to the frequency, high-frequency currents are flowing through the windings insulators. These currents through the insulation are very destructive for the insulation quality and lifetime [1, 56]. Consequently, the machine windings are known to fail quite commonly when using frequency converters [1]. However, adapted machines are available for these kind of applications. Additionally, when the frequency converter is installed several meters from the machine, due to reflections, overvoltages are easily imposed on the machine terminals [56, 57]. These overvoltages also stimulate the degradation of the winding insulation. Fortunately, lot of companies dealt with this issue by presenting several solutions e.g. filters (removing high-frequency components) and constructive changes at the stator windings.

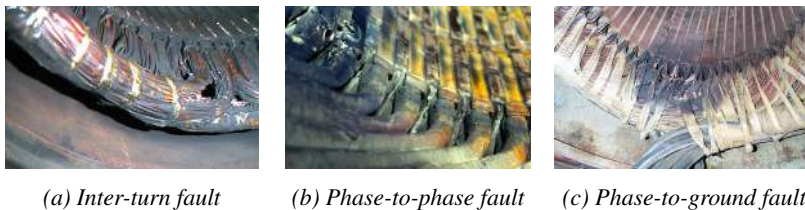


Figure 2.5: Examples of stator winding short-circuits, [1]

The subjected thermal, electrical, environmental and mechanical stresses can easily interfere with each other. For example: a loose foot can imply a stator deformation (mechanical stress), which easily causes an electrical unbalance in the stator. This unbalance can result in a temperature rise in the stator winding above the allowed limit (thermal stress). An excessive temperature leads to rapid aging of the insulation of the coil, which can directly result into a stator winding short-circuit. In general, the short-circuit does not directly imply a motor breakdown, but it has a negative influence on the operative condition of the machine. This because the shortened winding generates a MMF that has an opposite direction of rotation to the main MMF [20, 53] (negative sequence component). The efficiency decreases which again can result in an increase of the thermal overload or decrease in the machine performance limits. All of this reduces the machine lifetime significantly. Thereby, the effort of detecting winding degradation or winding short-circuits is valuable. Many research has already been conducted on the off-line detection on insulation problems in electric machines resulting in good and reliable measurement technologies [1, 17, 26]. As those technologies are out of the scope in CM

systems, no further discussion will be found in this thesis. On-line detection of stator short-circuits has been evaluated as well by different researchers based on the symmetrical component transformation, by evaluating either the negative sequence or zero sequence component in the current [20,53,58]. Additionally, the identification of the stator coil impedances can be used as a stator fault detection [54,55]. In particular for MCSA: the faulty frequency component induced in the stator current due to a short-circuit has been formulated by [31] and is presented as:

$$f_{st} = \left| f_1 \left[\frac{k}{p} (1 - s) \pm n \right] \right| \quad (2.2)$$

With:

f_{st}	the faulty frequency component [Hz];
f_1	the fundamental stator current frequency [Hz];
k	integer: 1, 2, 3, 4 . . . ;
p	the number of pole pairs [-];
s	the slip [-];
n	integer: 1, 3, 5, 7 . . .

According to [53], the presence of a zero sequence component e.g. the third harmonic in the stator current can also indicate a turn-to-turn short-circuit in the machine. This is because in a perfectly balanced three-phased load, zero-sequence components can not physically flow. Consequently, the presence of a third harmonic in the current indicates a stator unbalance caused by a short-circuit. Furthermore, some frequency converters intentionally induce third in-phase harmonics in the three power-lines in order to evaluate the winding balance. However, this third harmonic can also be assigned to other effects such as voltage unbalance, machine asymmetry, saturation, speed oscillation. . . The combination of several stator short-circuit indicators results in an increase of the algorithms effectiveness.

2.3.2 Rotor signatures

The main rotor related problems occurring in IMs can be subdivided by their electrical or mechanical origin. Regarding problems related to squirrel caged rotors, the rotor can be seen as a relatively simple and robust construction. Therefore, the electrical rotor problems are limited to broken rotor bars. They are extensively addressed to by other authors as significant electrical problems [14,21,30,50,59–62]. The rotor related problems with mechanical origin are focused on the eccentricity of the rotor with respect to the stator (static and dynamic) [21, 27, 61, 63–66]. This division between static and dynamic eccentricity will be related to relevant mechanical issues e.g. misalignment and mass-unbalance.

2.3.2.1 Electrical Errors

Broken rotor bars can be considered as a quite common indirect cause of failure. They will usually not be that destructive that they will cause a machine failure. Nevertheless, when they appear due to any kind of reason, they usually impose a significant loss of efficiency. For the same mechanical power, more electrical energy is consumed. That increase of electrical power can cause a machine overload (temperature) and under extreme circumstances causing the machine to fail. As a consequence, it is valuable to detect them so they can be repaired before they destroy the whole machine. Broken rotor bars are showed to have their main cause by severing heavy duty cycles [30, 50, 60, 62, 67]. Every change in torque or speed (by the load or the inverter) induces large varying currents through the rotor bars, this is inherent to the working principle of IMs. These variations in current firstly cause thermal stresses due to the repetitively heating and cooling of the bars. Secondly, tangential forces on the bars are a consequence of a current carrying conductor within a changing magnetic field. These are inevitably causing mechanical stresses. Thirdly, as most squirrel cages are constructed out of aluminum, porosity occurs due to the shrinking process of melted aluminum [68]. This porosity are small air bubbles in the cage, causing high resistant spots, resulting in local hot spots when conducting large currents. These thermal hot spots are causing thermal and mechanical stresses [68]. Conclusively, as regular rotor bars are usually dimensioned to work in the nominal loading conditions, repetitively changing the operative condition can cause a crack or a breakage in the rotor bars. However, most machine manufacturers produce machines especially designed for dynamic loads consisting of rotor bars with a very special geometry allowing high current overloads. Three industrial examples of broken rotor bars are presented in Figure 2.6. The reflection and propagation of broken rotor bars in the stator current



Figure 2.6: Examples of broken rotor bars, [1]

has extensively been discussed in [14, 30, 50, 59–61, 67]. Out of that literature, it is clear that the defect of one bar creates sideband components next to the fundamental frequency in the stator current. This is due to the asymmetrical currents in the rotor bars which impose a negative sequence magnetic field at a speed twice the slip frequency relatively to the stator [14, 30, 50, 59–61]. Consequently, the exact frequency of the sideband components f_{bar} in [Hz] can be formulated as:

$$f_{\text{bar}} = f_1(1 \pm 2 \cdot k \cdot s) \quad (2.3)$$

Because of the inherent relation between the fault frequencies and the motor slip s , detecting broken bars at a very low slip is quite challenging. Leakage of the fundamental current component in the spectrum frequently absorbs the important fault indicating components (leakage further discussed in Chapter 3). However, [14] suggested the Hilbert Transform in order to facilitate the detection of broken rotor bars with low rotor slip. This technique bundles the filtered and demodulated fault components with the fundamental current, resulting in an envelope technique. Applying this, the small difference in frequency between the several valuable harmonic components can be distinguished and broken rotor bars in a machine with low slip can be detected. Similar to the stator fault frequencies, the current fault signature corresponding with broken rotor bars can be induced by other effects e.g. load variations or shape imperfections of the rotor cage. [69] showed that load variations with the same stator current signature as a broken bar can still be discriminated. [50] took the first steps to distinguish broken rotor bars and the (same) induced frequencies of a large cage with spider structure (with equal number of legs as poles). To exclude the previous interfering effects, the detection of a broken rotor bar can also be performed during the startup of the machine and seems to be adequate [59, 70]. The technique is based on the decomposition of the transients in the stator currents due to a change of the load point. However, the MCSA-algorithm obtained in this thesis uses the fundamental equation (2.3) in searching the broken rotor bar fault frequencies and its harmonics.

2.3.2.2 Mechanical Errors

In the detection of mechanical fault related signatures in the stator current, one parameter is always required in calculating the characteristic fault frequencies: the rotational speed. Therefore, in order to exclude extra measurements and sensors, effort is made in order to detect the rotational speed in the spectrum of the stator current. [71] was the first to publish that a speed estimation for IMs can be derived from the stator current spectrum, which meant a crucial step in detecting mechanical faults of any origin. This allows to link mechanical fault signatures in the MCSA without physically measuring the speed of the machine. The estimation of the rotational speed f_r was determined to be the highest peak value within the boundary elements given by:

$$f_r = \text{maxpeak} \left[f_k; \frac{f_1}{p} \right] \quad (2.4)$$

$$f_k = \frac{f_1}{p} \left[1 - \frac{R_r}{\sqrt{R_{st}^2 + (X_{st} + X_r)^2}} \right] \quad (2.5)$$

with:

R_r	the rotor resistance $[\Omega]$;
R_{st}	the stator resistance $[\Omega]$;
X_r	the rotor reactance $[\Omega]$;
X_{st}	the stator reactance $[\Omega]$.

These components are ever-present in the current spectrum because of residual mechanical imperfection. Small eccentricities between rotor and stator, minor mass-unbalance, circular imperfections of the rotor/stator create an amplitude modulation between the fundamental current frequency and the rotational speed. (2.5) represents the search for the speed-indicating component. f_k is the physically maximal slip in the machine.

In practice, the method expressed in (2.5) is usually not applied. Two other spectral components are as well present in the current spectrum due to residual imperfections: two sidebands of f_r around f_1 . They are induced due to the ever-present unbalance and misalignment and propagating as a type of mixed eccentricity (2.7). These two components are detected in the spectrum out of which the mechanical speed can be obtained. This is conceptually presented in Figure 2.7. The speed estimator was successfully validated on both Direct On-Line (DOL) machines and frequency converter-fed machines [2, 39, 49].

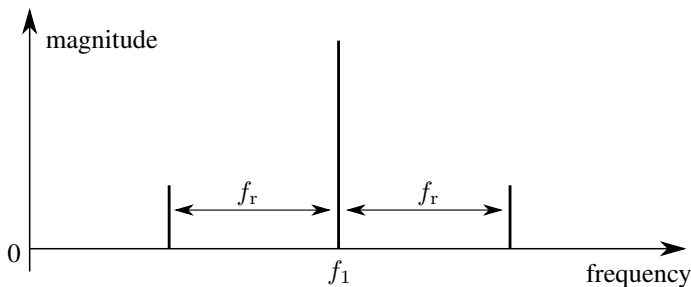


Figure 2.7: Detecting rotor speed with the ever-present unbalance and misalignment fault components in the stator current spectrum

The main mechanical rotor problems are mass-unbalance and misalignment. These faults are as broken rotor bars usually indirect problems. They do not directly cause a machine failure, but they increase the stresses on other more crucial machine components. Regarding mass-unbalance and misalignment, they commonly result in a failure of the bearings. This because both problems are imposing an overload on the bearings. They can be reformed and defined as specific eccentricity problems, which is defined as an unequal air gap between the stator and the rotor. Moreover, misalignment is linked to static eccentricity, where mass-unbalance can be defined as a form of dynamic eccentricity. That unequal air gap in the machines additionally generates an Unbalanced Magnetic Pull (UMP), which

is a radial electromagnetic force [63, 64, 66]. Consequently, both mass-unbalance and misalignment are quite frequent leading to bearing failure [1]. The machines installed in the industry are generally well balanced when they leave the factory. Nevertheless, depending on the application, severe unbalance can easily be imposed onto the machine. In some cases, the unbalance not only harms the bearings due to excessive radial load, but it can as well cause destructive vibrations. In addition, misalignment is even more present in current industrial plants. Due to lack of experience or consultant, only few companies make the effort in aligning their rotating equipment [1]. It is commonly assumed that the dimensioned frame on which the train will be installed is sufficiently aligned within the accepted boundaries. Nevertheless, especially in high-speed applications, small misalignment can cause significant destructive forces and vibrations. Although these faults can be detected and reported to the machine operators by performing CM, these kind of problems can easily be avoided by correct installation and basic maintenance.

Conclusively, these types of mechanical faults shorten the lifetime of the bearings due to the induced radial forces and vibrations. Consequently, they should be detected by the CM-system before they lead to the failure of the machine. In essence, misalignment can be considered as a static deviation of the rotor center with respect to the stator center. Due to the constant radial force working on the rotor, the rotor remains rotating around its own center point, but it is deviated with respect to the stator center. This is referred to as static eccentricity. Regarding mass-unbalance, the unbalanced mass imposes a centrifugal force onto the rotor, causing the rotor center to deviate from the rotational center. This deviation due to mass-unbalance is a form of dynamic eccentricity. The rotational center remains equal to the stator center, but the geometric center of the rotor rotates around the rotational center. These two types of eccentricity were extensively described by several authors [27, 61, 63, 65, 70] and is illustratively presented in Figure 2.8. If a combination of both dynamic and static eccentricity occurs, it is called mixed eccentricity.

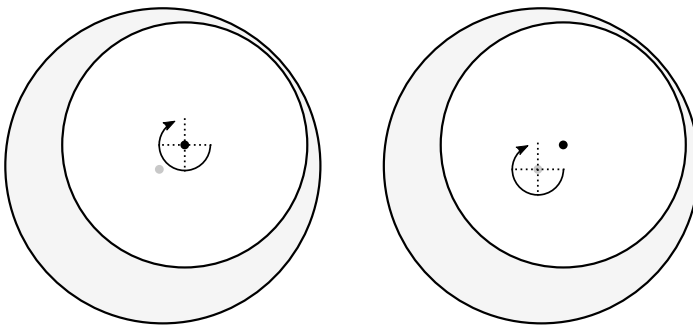


Figure 2.8: Static (left) and dynamic (right) eccentricity

The reflected fault frequency of these mechanical faults in the stator current is again modulated on the fundamental frequency component f_1 . The fault com-

ponents, f_{ecc} , caused by eccentricity on the stator current has been addressed by [27, 61, 63–65, 70, 72] and are written as:

$$f_{ecc} = \left| \left[(k \cdot n_{rs} \pm n_d) \frac{1-s}{p} \pm v \right] f_1 \right| \quad (2.6)$$

with:

n_{rs}	the number of rotor slots [–];
n_d	0 for static and 1, 2, 3 . . . for dynamic eccentricity;
v	harmonics of the fault frequency 1, 3, 5, 7 . . .

For mixed eccentricity, which is a combination of both static and dynamic eccentricity, the harmonics out of (2.6) are supplemented with the frequency components f_{eccm} :

$$f_{eccm} = |f_1 \pm k \cdot f_r| \quad (2.7)$$

This expression of mixed eccentricity and its harmonics represent the components which are used in the detection of the rotational speed in de IM, discussed in previous section. Due to unavoidable unbalance, misalignment and geometric imperfection, these components are always present in the stator current spectrum. The previous findings concerning the rotor eccentricity have been extensively confirmed by experimental results described in [61, 63–65, 72]. Axial static eccentricity has been investigated and simulated in [27] based on calculations of flux linkage. Out of that study, it was showed that an axial static eccentricity generates the same harmonics in the current as a uniform static eccentricity equal to the average of the inclined eccentricity. Consequently, if that average is zero, the problem can not be detected with MCSA and additional information is needed. It is thereby important to avoid axial loads on bearing which are not dimensioned for that purpose. In practice, it quite often occurs that axial load causes axial eccentricity and rapid bearing failure. The root cause of these failures are commonly a mismatch between several drive train components neglecting the thermal expansion of the rotors [1]. When two bearings along the drive train do not have the axial freedom to deal with thermal expansion, the bearings can easily get pressed and overloaded.

2.3.3 Bearing signatures

The fact that 40% of the unexpected motor failures are related to bearing issues illustrates the need of detecting these errors through MCSA. Bearing faults are not only the main root cause of failure, these faults are as well a common consequence of other causes e.g. stator winding unbalance, misalignment, mass-unbalance. . . Some literature mentions up to $\sim 95\%$ for rolling body bearings in induction machines below 750kW and $\leq 3000rpm$, [73]. This means that not only the origin of failure can be addressed to bearing faults, many faults evolve to a bearing fault. Consequently, a CM system can only be found to be effective if bearing faults can



Figure 2.9: Examples of bearing problems, [1]

be detected, preferably in a premature stage. The most common root causes of bearing problems are, [1]:

- excessive external vibrations by load variations, environmental conditions...;
- eccentricities due to unbalances and misalignments;
- dimensioning faults causing tight bearing under stress;
- bad lubrication leading to heating and abrasion;
- contamination of the bearing with e.g. air, water, acid or dirt;
- bearing currents (e.g. partial discharge, shaft currents).

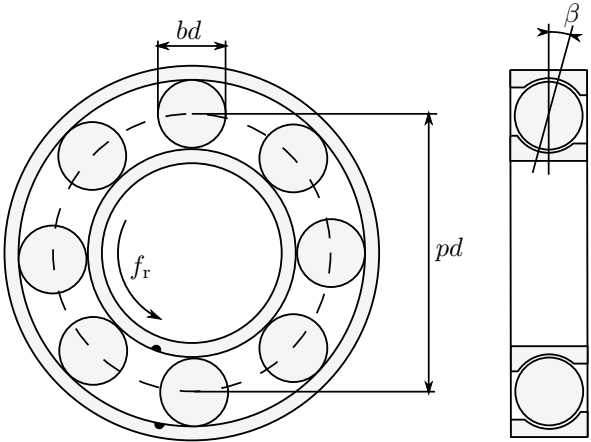


Figure 2.10: The commonly used dimensions for a regular ball bearing fault frequency calculation

As was indicated throughout this chapter, many faults can evolve into other stresses and categories, but bearing faults are by far the main cause of failure. Within bearing faults, further categorization can be defined on two levels: the geometric origin of the fault and the physical type of material wear. On the geometric part, four types are defined: outer race, inner race, bearing ball and bearing cage problems (components visible in Figure 2.10). The type of the material wear can

subsequently be defined either as: spalling, overheating, brinelling (true or false), flaking, grooved wear, corrosion, contamination... Some of these bearing problems are presented in Figure 2.9. In literature, regarding bearing faults in the raceways, it is generally addressed to as *single point* bearing faults. As most bearing faults of any origin or stress-type comes down to wear of material, the first crack on the raceway's surface is called a single point pit. It is then the purpose of the CM system that, from this event on, the problem is detected as fast as possible. Consequently, most research on detecting bearings faults is focused on single point outer/inner race bearing faults. According to [22–24, 38, 43, 44, 72, 74, 75], the induced fault frequencies in the stator current for a single point bearing pit on the outer respectively inner race of the bearing, f_{out} and f_{in} , are defined by the equations:

$$f_{\text{out}} = \left| f_1 \pm k \cdot \frac{n_b}{2} f_r \left[1 - \frac{bd}{pd} \cos \beta \right] \right| \quad (2.8)$$

$$f_{\text{in}} = \left| f_1 \pm k \cdot \frac{n_b}{2} f_r \left[1 + \frac{bd}{pd} \cos \beta \right] \right| \quad (2.9)$$

with: n_b the number of bearing balls; bd the bearing ball diameter; pd the bearing pitch diameter; and β the bearing contact angle. These parameters are visualized in Figure 2.10. These fault-related frequency components are strongly linked to the formulas presented in Table 2.2. They only differ in the modulation with the fundamental current component f_1 . The origin of these equations, referred to as characteristic bearing fault frequencies, can be found using Figure 2.11. First, the angular speed of the rotor and the stator is defined as:

$$\omega_{\text{rot}} = 2\pi \cdot f_r \quad (2.10)$$

$$\omega_{\text{stat}} = 0 \quad (2.11)$$

Neglecting any slip between the bearing balls and the rotor respectively stator, the speeds of the bearing ball as indicated in Figure 2.11 can be written as:

$$v_{\text{out}} = 0 \quad (2.12)$$

$$v_{\text{cage}} = \omega_{\text{cage}} \frac{pd}{2} \quad (2.13)$$

$$v_{\text{in}} = \omega_{\text{cage}} \cdot pd \quad (2.14)$$

This because the speed v_{in} is twice the speed v_{cage} when the ball is rolling on the outer race. As the speed v_{in} is as well the peripheral speed of the inner race, it can be written as:

$$v_{\text{in}} = \omega_{\text{rot}} \frac{pd - bd \cos \beta}{2} \quad (2.15)$$

Using (2.14) and (2.15), the angular speed of the rotor cage is determined to be:

$$\omega_{\text{cage}} = \omega_{\text{rot}} \frac{pd - bd \cos \beta}{2 \cdot pd} \quad (2.16)$$

$$= \frac{1}{2} \omega_{\text{rot}} \left[1 - \frac{bd}{pd} \cos \beta \right] \quad (2.17)$$

This rotational speed can be presented in [Hz] instead of [rad/s], obtaining the Fundamental Train Frequency (FTF) as presented in Table 2.2:

$$f_{\text{FTF}} = \frac{1}{2} f_r \left[1 - \frac{bd}{pd} \cos \beta \right] \quad (2.18)$$

Out of this equation, the ball pass frequency for the outer race (BPFO) can be obtained by the differential speed of the cage with respect to the outer race, multiplied with the number of bearing balls:

$$\omega_{\text{BPFO}} = n_b (\omega_{\text{cage}} - \omega_{\text{stat}}) \quad (2.19)$$

$$f_{\text{BPFO}} = n_b \cdot f_{\text{FTF}} \quad (2.20)$$

$$= \frac{n_b}{2} f_r \left[1 - \frac{bd}{pd} \cos \beta \right] \quad (2.21)$$

The same can be done for the ball pass frequency for the inner race (BPFI), now by the speed difference between the cage and the inner race:

$$\omega_{\text{BPFI}} = n_b (\omega_{\text{rot}} - \omega_{\text{cage}}) \quad (2.22)$$

$$f_{\text{BPFI}} = n_b (f_r - f_{\text{FTF}}) \quad (2.23)$$

$$= n_b \cdot f_r - \frac{n_b}{2} f_r \left[1 - \frac{bd}{pd} \cos \beta \right] \quad (2.24)$$

$$= n_b \cdot f_r - \frac{n_b}{2} f_r + \frac{n_b}{2} f_r \frac{bd}{pd} \cos \beta \quad (2.25)$$

$$= \frac{n_b}{2} f_r \left[1 + \frac{bd}{pd} \cos \beta \right] \quad (2.26)$$

These formulas obtained for FTF, BPFO and BPFI are as presented in Table 2.2 and are modulated around the fundamental current component f_1 in the calculation of (2.9). This because of the inherent transition path between the mechanical fault and the reflection in the stator current.

The calculation of the characteristic bearing fault frequencies require the knowledge of the parameters pd , bd , n_b and β as indicated in Figure 2.10. However, obtaining these dimensional parameters in an unknown industrial installation can be very difficult. In such cases, [21, 38, 74, 75] present an approximation for the race frequencies which is shown to be valid for most bearings with 6 to 12 rolling elements:

$$f_{\text{in}} = |f_1 \pm k \cdot 0,6 \cdot n_b \cdot f_r| \quad (2.27)$$

$$f_{\text{out}} = |f_1 \pm k \cdot 0,4 \cdot n_b \cdot f_r| \quad (2.28)$$

The fault frequency, f_{ball} , due to wear on a rolling element in a bearing has been investigated in [22, 23, 38, 43, 44, 75] and is given by the equation:

$$f_{\text{ball}} = \left| f_1 \pm k \frac{pd}{2 \cdot bd} f_r \left[1 - \left(\frac{bd}{pd} \cos \beta \right)^2 \right] \right| \quad (2.29)$$

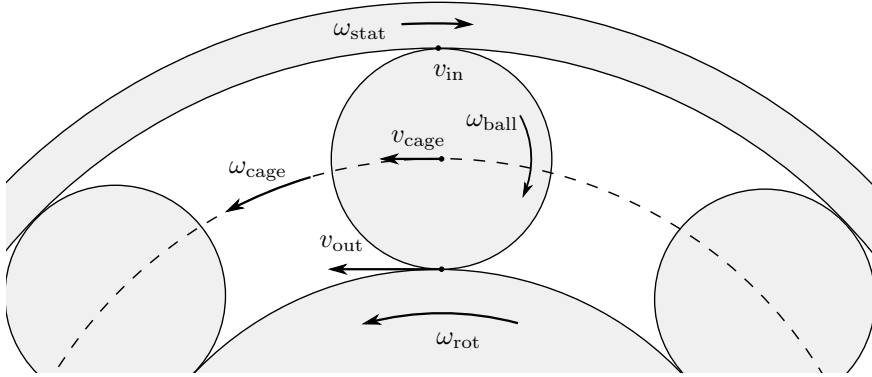


Figure 2.11: The derivation of the kinematic model in obtaining the characteristic bearing fault frequencies

This fault frequency is in practice always present in the spectrum as soon as one of the raceways is subjected to some problems, even without an explicit bearing ball problem. This because it is an inevitable bearing forcing frequency. In general, it rarely occurs that a real bearing ball fault is actually present when it is detected in the stator current, even in the vibration spectrum [1]. It will be shown throughout this dissertation that, as soon as a bearing fault occurs of any origin, all fault frequencies appear in the spectrum, especially the ball spin frequency (BSP) and the FTF. Only the correct interpretation of the magnitudes of the characteristic fault harmonics can really make the distinction between the origin of the detected fault. At last, the fault frequency f_{cage} when a cage failure occurs in the bearing, similar to (2.18) and presented in [22–24, 38, 43, 44, 72, 74, 75] as:

$$f_{\text{cage}} = \left| f_1 \pm \frac{k}{2} f_r \left[1 - \frac{bd}{pd} \cos \beta \right] \right| \quad (2.30)$$

In the world of CM, more specific vibration analysis, it is uncommon to detect a faulty cage in the vibration spectrum. This is mainly because the evolving forces when a defect in a bearing cage occurs are very small. As for vibration analysis the forces between the rotor and stator have to be large before they propagate as an acceleration of the stator housing, it is almost undetectable. Since MCSA measures the displacement between the IM rotor and stator, bearing cage faults are in fact detectable in the stator current in a quite early stage. This will be shown by experiments in Chapter 6.

The study presented in [22] indicates that classic MCSA based on Fourier analysis is insufficient due to the varying magnitude of the fault related frequency components. These varying magnitudes have a spreading effect on the components in the spectrum. Consequently, the use of wavelet packages was introduced. In [44], a full categorization is made for the different bearing faults and their signature in the stator current. The presented study concludes that there is a huge difference

between the single point errors (described above) and generalized roughness of the raceways. This is because the roughness does not induce the clear frequencies described for the single point bearing failures. The faults produce broadband changes in the current spectrum. Nevertheless, [72] successfully investigated the detection of those faults by the produced eccentricity (due to the wear) between the stator and rotor. It can be concluded that the displacement is detectable, but difficult to determine the exact origin of the fault. The efficiency can also be used together with the stator current spectrum as an indicator for generalized roughness faults, described in [38], but in this case, additional sensors are needed. Another detection technique for bearing problems has been described in [28,37]. With a combination of noise cancellation and statistical processing techniques, it is possible to detect bearing issues without requiring detailed information of the machine. The noise cancellation technique is an algorithm which divides the stator current components into noise and fault related components. However, due to the advanced analyzing capabilities presented in the next chapter, all predefined fault components are visualized using a simple discrete frequency transformation. No further algorithms were needed to find specific fault components in the stator current.

2.4 Conclusion

This chapter presented the state of the art of applying motor current signature analysis as a condition monitoring technology. First, the most common technologies in performing CM were briefly discussed. From thereon, the potential of MCSA was stated as a less expensive, more reliable and more complete way of monitoring as it is performed today. Regarding MCSA, the most common detectable faults which can occur in IMs were discussed by type, stress, location and their corresponding reflection in the stator current. In literature, the fault signatures are well described providing clear formulas where exactly the fault component should be located in the spectrum when a certain problem occurs. However, till today, information on the fault severity is still lacking or inadequate. Although a lot of IMs are characterized by specific severity alarming limits or guidelines regarding the detection of electrical faults e.g. broken rotor bars and stator winding shortcuts, information on mechanical severity is still missing completely. This is one of the main reasons why, several years ago, the use of MCSA in CM was neglected as it was experimentally confirmed that the severity estimation of mechanical faults was defined to be impossible or too complex. However, in this dissertation, an effort is made towards finding quantified relations between mechanical fault severities and their magnitude of reflection in the stator current. In order to be able to analyze the evolving mechanical faults in the current spectrum, next chapter is fully committed to measuring the stator current and the signal processing techniques in order to visualize the relevant fault components.

3

Stator current analysis

3.1 Introduction

Using the electric machine stator current in order to estimate the operational condition of the machine starts by measuring the current and visualize the valuable information. In the previous chapters, it has become clear how mechanical faults are propagated from the rotor to the stator. Thereby, relying on literature, it is known how the current should be analyzed to find some fault indicating components. By performing an accurate frequency analysis on the current time signal, fault related frequency components can be highlighted in the spectrum. It became clear in previous chapter that, when searching for spectral fault indicating components, attention should be given to the accuracy in frequency resolution and the disadvantageous Signal-to-Noise-Ratio (SNR). It was additionally mentioned that informative current components can easily be obscured in the spectrum. With the goal of finding fault related current components in the stator current, this chapter has three main parts: how the current will be measured; how the current signal will be processed/analyzed and the practical implementation of the analyzing algorithm. This chapter is fully based on a thorough literature study. Consequently, no novel contribution to this field of current measurements has been made in this research. Nevertheless, it is important to relate the known theory to the particular needs for performing CM based on current measurements starts with an accurate acquirement of the current signals. Gaining knowledge on the errors made by performing the measurement and the phenomena linked to the frequency transformation are required for a correct signal interpretation. It will be shown throughout this chapter that using cheap, commercially available current clamps and some fundamental digital signal processing techniques, CM with MCSA can be performed.

3.2 Measurement method

Performing *accurate measurements* is the ultimate goal for all experimental researchers. Unfortunately, by conducting measurements, errors are unavoidable and ever-present in every application. The question that should be asked is: "What is the tolerable error that can be made which will not interfere with the corresponding outcome?" Subsequently, two crucial questions can be extracted before defining any measurement topology or methodology:

1. What is the purpose of the measurement?
2. What is the signal that has to be measured?

Comprehensibly, information is needed about the signal that must be measured. It starts by determining the quantity e.g. voltage, current, temperature, vibration... Although many quantities can be measured, most sensors provide a voltage signal which has a predefined linear relation to the measured quantity within the useful measurement range. However, the content of the signal is at least equally important: the domain and the scope of the signal; the time variance of the signal; the valuable frequency content... This time variance is very important especially for electrical current measurements. In the field of electricity, the term Root Mean Square (RMS) is generally used in order to represent the magnitude of a signal (voltage and/or current). The RMS value represents an equivalent DC current which has the same power dissipation as the AC current. Therefore, this value is a representation of the power within one period. However, using RMS quantifications, no information is given on the shape of the current. And because the RMS value can be seen as a proportional calculation of the surface underneath the time based signal, two signals with the same period and RMS value can significantly differ in maximum instantaneous magnitude (see Figure 3.1). This can be the case when the stator currents are evaluated from two similar machines, one connected direct-on-line and one inverter fed. The RMS current can be equal, but the maximum current differs. Although the range of a current sensor is usually indicated by the RMS current, it is physically limited by an instantaneous maximum value (peak-value). Consequently, most data sheets of electrical measurement devices indicate a maximal allowed *crest factor*, which is the ratio between the maximum value and the RMS value. In this way, combining the maximum indicated range and the maximum crest factor, the measurable signals for that specific sensor are defined in magnitude. Next to this definition of magnitude-range, the bandwidth is an inherent property of each sensor defining the frequency-range. This indicates what frequency content can be measured, as the bandwidth is usually indicated with the frequency where the output signal is attenuated with $3dB$. It is however not uncommon that next to an upper limit in frequency, a lower limit is indicated (e.g. 10Hz-10kHz). After the signal is captured by the sensor, the time-varying signal usually has to be digitized by an Analog-Digital-Converter (ADC) for several (digital) post-processing techniques. During that conversion, two main parameters are defined: the quantization step and the sample-rate. The quantization

step represents the magnitude resolution of the signal. The sample-rate is how many samples are captured per time-unit. This discretization is a crucial setting during the conversion, as the transfer from an analog signal to a digital signal implies a huge loss of data information regarding magnitude and time. Depending on the proceeding signal processes after capturing the data, the sample-rate plays an important role in the characterization of the signal. For example, if the instantaneous maximal value of a signal has to be determined, it is important that this specific moment in time is captured. It is shown in §3.3 that both the sample-rate and the measurement time having a significant impact on the transformation to the frequency-domain. However, before conducting the measurement, information on the signal is needed in order to properly match the sensor range and bandwidth together with the ADC quantization step and sample-rate.

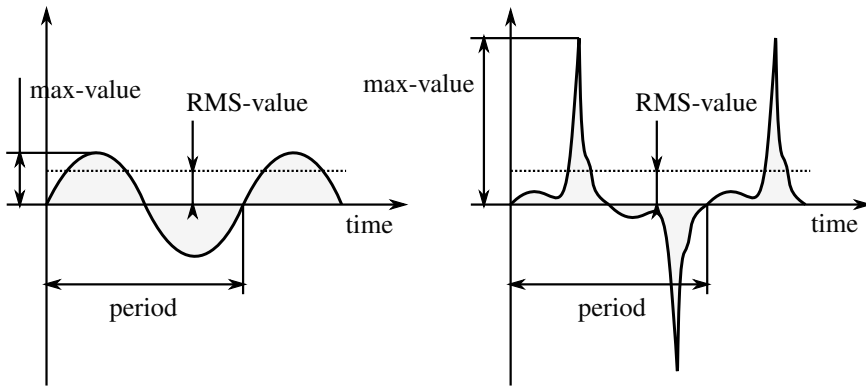


Figure 3.1: Two signals with the same RMS value but with another crest factor

Complemented with the signal properties, information must be gathered about the purpose of the signal. If the measurement acts as an indication or it serves as an input of a high dynamic control system, different measurement methodologies are applied. Fortunately, in this application, it is quite clear what kind of signal is to be measured and what specific information of the signal is of importance. A stator current of an electric machine has to be measured in order to extract a wide range of fault indicating frequency components. This implies a high accuracy in magnitude and in frequency resolution. Next section, §3.2.1, is focused on measuring current with high accuracy over the whole frequency range. Additionally, the current to be measured has a very disadvantageous SNR which represents the amount of valuable data with respect to undesired or unnecessary measured data. This will be handled and validated through that section by some experimental measurements. The following sections will focus on the frequency accuracy and resolution (§3.3). The detection algorithms and signals processes are bundled and validated with a case study in §3.4.

3.2.1 Current measurement

The electrical current through an electric circuit can be measured by different methods of which the commonly applied ones are listed in Table 3.1, [6]. As for measuring other units, most of the methods result in a measurement of voltage. Hence, voltage can easily be measured with high accuracy. The indication of a direct measurement in Table 3.1 means that the measurement device is implemented in the electric circuit. Consequently, the measurement usually affects the current through the circuit. An indirect method is when the current is measured without significantly affecting the electrical system. Regarding CM measurements, it is important that the measurement does not affect the fault analysis and that the measurement can easily be conducted on-line. Therefore, only indirect measurements are taken into consideration. Nevertheless, an overview of the methodologies listed in Table 3.1 is given and subsequently described following [6].

Direct/Indirect	Modus	Method
Direct	Resistive	Current sense resistors
	Transistor	$R_{DS(ON)}$
		Ratio-metric
Indirect	Magnetic	Current transformer
		Rogowski coil
		Hall effect device

Table 3.1: Current measurement methodologies, [6]

Resistive current measurement is the most straight-forward and convenient way of measuring current through an electrical conductor [6]. An especially calibrated resistor is placed in the electric circuit whereby a proportional measurable voltage over that resistor manifests due to the current through the resistor. Usually, a low impedance shunt resistor is used with a stable temperature coefficient. Note that the lower the impedance is, the less the measurement affects the circuit. At a rather low cost, a robust and accurate current measurement is obtained. However, due to the inductive and relative low impedance property of the stator, the resistor can easily interfere with the electric circuit. Additionally, due to this direct measurement method, the machine conductors have to be interrupted to install the shunt resistor and the measurement circuit is not galvanically isolated from the power circuit. This is not convenient for large power applications.

Transistor current measurement is mostly applied to create a overcurrent protection [6]. Although, Ratio-Metric current sensing MOSFETs can be used to measure current. However, they are limited to an accuracy of $\pm 5\%$ of the measured current (with temperature compensation) [6]. This method again provides a voltage proportional to the measured current. They have the advantage of being lossless since these components generally have a negligible resistance. As this

method is again direct and results in a very poor accuracy, this method is not taken into consideration in performing CM.

All indirect measuring methods are essentially *Magnetic current measurements* [6]. This results immediately in an isolation between the electric circuit and the equipment. A first principle to measure current by a magnetic modus is using current transformers. Due to the basic principle of the transformer, the current to be measured has to be alternating. This is because a change of magnetic flux is required in order to induce voltage in the secondary winding. Consequently, no DC current can be measured. By minimizing the number of turns in the primary coil, a low impedance path can be obtained. Thereby, the interaction of measuring the current and the current itself is minimal [6]. In practice, ring-shaped laminated steel is constructed around the conductor to be measured and the secondary coil is wound around the lamination steel (as seen in Figure 3.2) [6]. Thereby, the electric circuit does not have to be interrupted to implement the measurement equipment and the primary coil is minimized. Usually, the current through the secondary coil I^* is rectified and transformed to a measurable voltage signal V_I . This is the basic principle of a commercial current clamp. The voltage induced in the secondary coil can subsequently be related linearly to the measured current I . It has to be mentioned that in practice, the current I^* is kept constant by regulating the voltage V_I . Thereby, the flux through the coil can be manipulated in order to keep the clamp working in the linear area. Additionally, in order to measure accurately, the laminated steel may not be in the nonlinear magnetization area (saturation). Therefore, the indicated current range (RMS and crest factor) should be respected. This is a common mistake by measuring non-sinusoidal currents. Generally, the RMS current is within the current range of the clamp, but as noticed in previous section, the instantaneous maximal current can easily be out of range. In these cases, the captured signal is deformed. Avoiding this change of incorrect measurements due to clamp saturation, Rogowski coils can be applied [6]. Using a Rogowski coil in order to measure current magnetically is the second main principle. This principle is similar to the current transformer, but the Rogowski coil has an air core instead of (normally) laminated steel. Consequently, the Rogowski has a very small inductive property and therefore a fast, linear response between the measured current and the corresponding voltage. As magnetic saturation does not apply for the air core in Rogowski coils, the risk of measurement errors is reduced. Nevertheless, the required integrator can easily induce unacceptable errors in the very low and high frequency regions [6].

When the measurement of AC and/or DC is required, the third main magnetic principle can be applied: measuring with a Hall-element [6]. The physical methodology is presented in Figure 3.3. The current I induces a magnetic field B , which interferes with the constant current I_c through a metallic plate. That interaction between the field B and the current I_c can be measured in the change of voltage over the metallic plate, V_I . As this indirect method literally measures the magnetic field, DC current can be measured. This method is more expensive and less robust than using a current transformer due to the increased internal complexity [6].

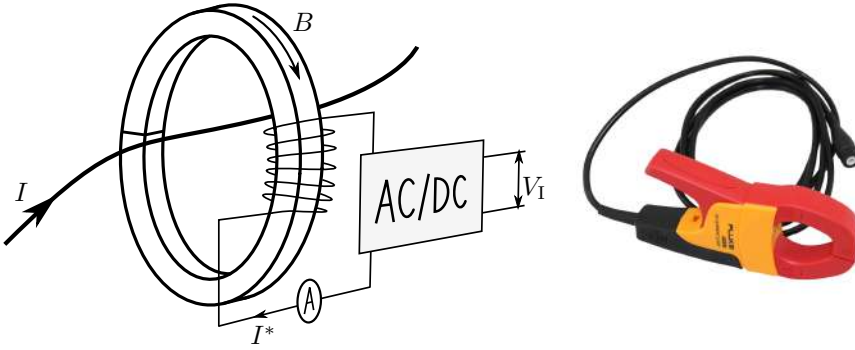


Figure 3.2: The working principle of a Fluke® i400s current clamp (classic current transformer)

Additionally, the required external voltage is usually provided by batteries which causes issues for long term measurements. This can however be avoided by the installation of a grid-connected power supply. Nevertheless, due to the capability of measuring DC, this measuring principle is abundantly applied.

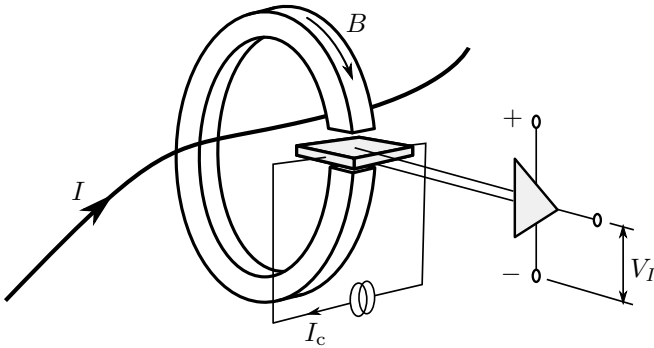


Figure 3.3: Working principle of measuring current with a Hall-element

As the industrial and commercial purpose of this research can not be neglected, it is of huge interest to validate whether a simple, cheap, robust, commercially available current clamp satisfies the requirements of detecting fault related frequency components in the spectrum of the stator current. By considering all previously mentioned technologies, the preferred measurement methodology is applying current clamps (transformer principle). The current clamp under test is the Fluke® s400i, Figure 3.2. Table 3.2 presents the most relevant properties. The two ranges create the flexibility for measuring large and small power sizes with a satisfying accuracy. The bandwidth of 10kHz exceeds by far the fault reflecting area (see fault formulas discussed in §2.3). Additionally, an internal voltage transformation is included, which simplifies capturing the data. The indicated clamp measurement accuracy is an interesting property to consider. Due to the disadvan-

	40A Range	400A Range
Measurement range	0.5A-40A	5A-400A
Bandwidth	5Hz-10kHz	
Output voltage	10mV/A	1mV/A
Accuracy	$\pm 2\% + 0.015A$	$\pm 2\% + 0.04A$
Conductor position	$\pm 1\%$ of reading + 0.05A	
Temperature coefficient	$\pm 0.01\%/^{\circ}C$ ($\leq 18^{\circ}C$ or $\geq 28^{\circ}C$)	

Table 3.2: Fluke® i400s current clamp properties

tageous SNR, signals up to $-60dB$ (attenuation of 1000 with respect to the fundamental component, derived from the results out of [2, 13, 23, 24, 38, 43, 74]) must be distinguished with high accuracy from a fundamental current component of e.g. 40A or 400A. Following the indicated accuracy in Table 3.2, this would never be possible, as the accuracy for both ranges during full reading would respectively be $\pm 1.27A$ and $\pm 12.09A$. The absolute measurement error as a function of the RMS current through the clamp is presented for the 40A-range in Figure 3.4. Following those properties, it is clear that this clamp would never be able to accurately capture very small frequency components superposed on the large fundamental current. Nevertheless, because the use of this cheap, commercial current clamp would be very beneficial in this application, an experiment is conducted in order to validate the accuracy of measuring small frequency components in a large RMS current signal.

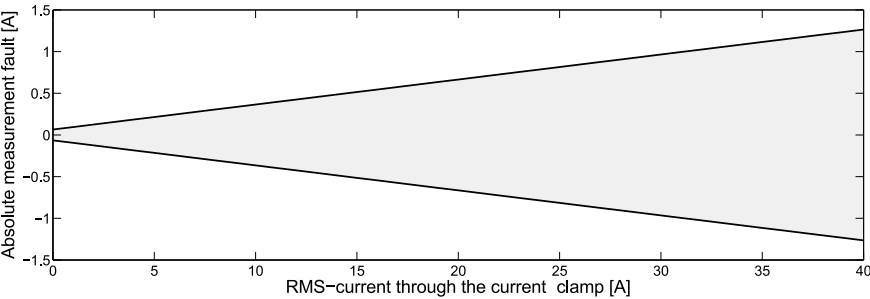


Figure 3.4: Fluke® i400s absolute fault for the 40A range

The setup for the experiment is presented in Figure 3.5. A current is conducted through an electric circuit by connecting several 200W incandescent lighting bulbs to the power grid. A small current with a known and controllable amplitude and frequency is generated using a signal generator. Those two different currents are both measured by the *Fluke® i400s* current clamp. The small signal is additionally measured by a second, more accurate *Agilent* current clamp ($\pm 0.1\%$

of reading) and through voltage via a shunt resistor of 44.40Ω . The voltage measured on the shunt resistor is used as a reference to compare both measurement results of both current clamps. The purpose of the measurement is to confirm the fact that, following the data sheet, small superposed signals on a large fundamental component are not measurable with the *Fluke® i400s* current clamp [7]. Therefore, repetitively, several frequency components of different frequencies and magnitudes are superposed on the 'large' fundamental current which is changed as well. The magnitude of the superposed signal varies from 1mA to 100mA each at a frequency of either 51Hz, 73Hz, 270Hz and 884Hz (relevant to the range of the stator current fault frequencies, Chapter 2). The fundamental component of 50Hz varies in magnitude by switching 200W incandescent lamps from 1 to 15 bulbs. The switching of these bulbs results in a current variation from 0.87A to 13.20A in steps of 0.87A. The relation between the amplitude of the small current through the clamps and the relative measurement error is presented in Figure 3.6. A zoom of those results is presented in Figure 3.7.

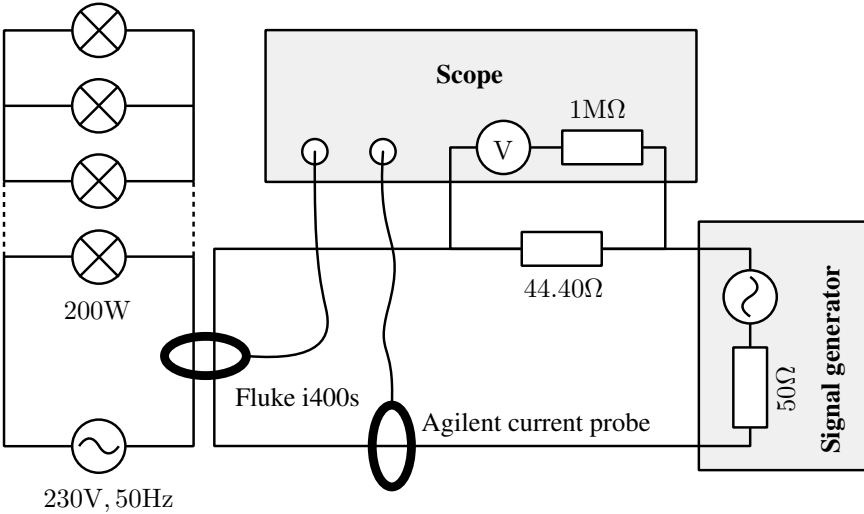


Figure 3.5: *Fluke® i400s* performance test set-up

As can be observed, the *Fluke® i400s* current clamp satisfies the requirements unexpectedly. Following Table 3.2, only an accuracy of $\pm 412\text{mA}$ can be obtained when a fundamental current of 13.20A is flowing. However, when a signal of several mA manifests on other frequencies, a general accuracy can be obtained of $\pm 2.5\%$ of the superposed signal magnitude. By doing this experiment, it becomes clear that the indicated accuracy in the data sheet can be applied separately for each frequency. The reason that this is not included in the data sheet of the current clamp is probably because this is not one of the purposes of this current clamp. As will be shown further throughout this dissertation, fault related frequency components in the stator current are valuable to analyze upward the limit of -60dB in reference to the fundamental 50Hz-wave (§3.4.3). For an 11kW IM, the fun-

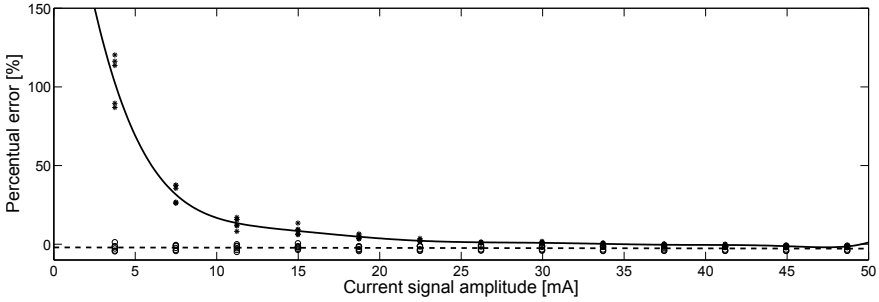


Figure 3.6: The relative measurement error of the Fluke® i400s current clamp (circular markers and correlated with the striped line) and the Agilent current clamp (star marker and correlated with the full line)

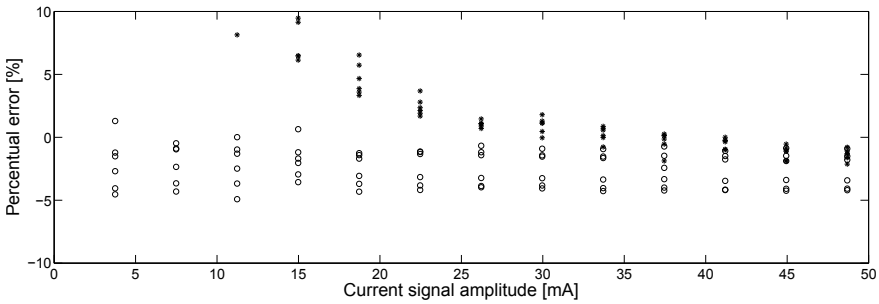


Figure 3.7: Zoom of the relative measurement error of the Fluke® i400s current clamp (circular marker) and the Agilent current clamp (star marker)

damental stator current component is $\sim 15\text{A}$, the valuable fault components will generally be $\sim 15\text{mA}$. Following the current clamp data sheet, this small signal would disappear in the boundaries of measuring accuracy. However, doing this experiment confirmed that those signals can easily be measured with an accuracy of $\pm 2.5\%$. Consequently, currents are measured by the Fluke® i400s current clamps in following dissertation. Due to this experiment, it can fortunately be stated that a CM technology based upon stator current measurements can be established with the use of rather cheap, commercially available current clamps.

3.2.2 Data acquisition

As the current is measured with a sufficient accuracy, the current clamp voltage signal must be acquired. As the signal will be processed digitally, an analog-to-digital signal conversion is required. That conversion contains a discretization of the signal in the time domain, defined by a sample-rate. Additionally, the signal is discretized in the magnitude, defined by a quantization step. The sample-rate is the number of samples taken in one second. If this rate is too high, unnecessary data has to be stored. If the rate is too low, valuable data can be lost. The sample-rate is in this case defined by the valuable content in the frequency spectrum. As



Figure 3.8: The National Instruments™ cDAQ system to acquire voltage

the signals will be examined for fault-indicating components between 0Hz (DC) and 2kHz (§2.3), a minimum sample-rate of 4kHz is required (see §3.3). To acquire the voltage signal, *National Instruments™ Compact DAQ Card NI-9238* and *Chassis NI-9181* are used (Figure 3.8, [8]). With this card and chassis, 4-channel voltage signals of maximum $\pm 500\text{mV}$ can be sampled simultaneously with a maximal sample-rate of 50ks/s [8]. Every sample is stored as a 24-bit word, which defines the quantization step of 59.6nV ($= 0.596\mu\text{A}$). The accuracy of the card is defined as $\pm 0.07\%$ of reading and $\pm 0.005\%$ of the range. Acquiring the voltage signal out of the *Fluke® i400s* current clamp while measuring 15A, an absolute measurement error is made of $\pm 1.65\text{mA}$ due to the analog-to-digital conversion. As this error of $\pm 0.011\%$ is negligible with respect to the error made by the current clamps ($\sim \pm 3\%$), it is not taken into account during analysis. Using the *NI-9181* chassis with USB cable, data can directly be imported in *Matlab®*. Furthermore, settings such as measurement time, sample-rate, sensor settings can be controlled from this software. This way of measuring creates both high quality and flexibility, complementary for this research. Further throughout this dissertation, grid voltage and vibration will be captured as well with NI-cDAQ-cards (respectively *NI-9242* and *NI-9234*) and the 4-slot chassis *NI-9174*. This way of sampling ensures that vibration, voltage and current are simultaneously logged with the same time-stamp.

To conclude the current signal acquiring, the measurement errors in magnitude made by the current clamp and ADC conversion are listed in Table 3.3 for measuring a 10A sinusoidal current using the *Fluke® i400s* current clamp and the *NI-9181* data-acquisition card.

		Voltage error [mV]	Current error [mA]
Fluke® i400s	±2.5% of reading	±2.5	±250
	±15mA absolute	±0.15	±15
NI-9238	24-bit on ±500mV	$59.62 \cdot 10^{-6}$	$5.962 \cdot 10^{-3}$
	±0.07% of reading	±0.07	±7
	±0.005% of scale	±0.025	±2.5
Total measurement error		±2.745	±274.5

Table 3.3: Error made by capturing 10A using the Fluke® i400s current clamp [7] and the NI-9181 DAQ-card [8]

3.3 Frequency analysis

Out of the previous section, the signal is measured and digitized with a clearly defined accuracy (see Table 3.3). Now, the frequency spectrum must be obtained before fault related data in the current can be visualized in the current spectrum. To obtain a frequency spectrum out of a time based digital signal, a frequency transformation is required. Three main methods are defined in order to transform signals to the frequency domain: Fourier transform, Laplace transform or Wavelet transform. In signal analysis, only Fourier and Wavelets are applicable. Due to the gained experience in previous research and the ready-made algorithms applied in *Matlab*®, it is chosen to apply the *Discrete Fourier Transform* (DFT), by using the *Fast Fourier Transform* (FFT) algorithm. This transforms a time based signal to a frequency based signal. It is not excluded that other transformation techniques e.g. the Wavelet transformation will not be needed in the application of stator current based condition monitoring in order to compete with time-varying signals [70]. However, in this scientific research, the DFT will meet the requirements as the conducted measurements and analysis can be conducted under controllable and stabilized non-time varying conditions. This method is universally applied in a wide variety of branches [3, 9]. However, several transforming phenomena introduce difficulties in the proper interpretation of the spectral content. Although the phenomena by transformation are unavoidable, numerous attempts were made to minimize those errors. By applying techniques such as anti-aliasing and windowing, a sufficiently accurate spectrum is obtained to satisfy the needs of analyzing fault indicating frequency components in the spectrum. The following sections will briefly discuss the DFT, its phenomena and the proper solution applied in this research within the context of the application.

3.3.1 Discrete Fourier transformation

The French mathematician and physicist Joseph Fourier (1768* - 1830†) stated and proved around the year 1822 the following groundbreaking statement:

"Every time-periodic signal can be written as a linear combination of sine and cosine functions."

This statement is expressed mathematically by the following continuous time equation:

$$f(t) = \frac{1}{\sqrt{2 \cdot \pi}} \int_{-\infty}^{\infty} \mathcal{F}(\omega) \cdot e^{-j \cdot \omega \cdot t} \cdot d\omega \quad (3.1)$$

with $f(t)$ the periodic time function, $\mathcal{F}(\omega)$ the Fourier frequency function and the frequency ω . By applying this formula, every continuous time signal can be represented by an infinite sum of sine and cosine functions. However, the time based function to be transformed is discretized, which makes it impossible to work in the continuous time domain. Therefore, the Discrete Fourier Transformation (DFT) is applied in order to transform the sampled (discrete) current signal into a discrete frequency signal. This discrete Fourier series is in most cases practically

applied by means of a Fast Fourier Transform (FFT). The FFT is fundamentally nothing more than a optimized algorithm to calculate the DFT in a very fast and efficient way [3, 9]. The basic mathematical expression for the DFT algorithm is expressed as:

$$I(k) = \frac{1}{N} \sum_{n=0}^{N-1} I(n) \cdot e^{-j \frac{2 \cdot \pi \cdot k \cdot n}{N}} \quad (3.2)$$

with the sequence $I(k)$ of N complex numbers, the sampled stator current $I(n)$ for sample n , the frequency k and the total number of samples N . As can be noticed, the frequency spectrum obtained by the FFT always contains a number of discrete frequency values equal to the number of samples provided by the time signal. As (3.2) only holds for periodic signals, the provided time signal is considered to be periodic following the full measurement time T_m . As a consequence, the fundamental frequency is inevitably defined as $1/T_m$, regardless the captured time signal. Following Fourier's statement, the signal can be reconstructed by a combination of sine and cosine functions having frequencies which are integer multiples of the fundamental frequency $1/T_m$. Therefore, the resolution of the frequency spectrum, or the distance between two frequency components is $1/T_m$. Additionally, the number of samples $F_s \cdot T_m$, where F_s is the sample-rate, are divided in negative and positive frequency components. As the spectral resolution is $1/T_m$ and $F_s \cdot T_m$ frequency components can be generated, the domain of the spectrum is determined to be $[-F_s/2; +F_s/2]$. Conclusively, the time signal sample-rate F_s determines the domain of the DFT to be $[-F_s/2; +F_s/2]$ and the time signal measurement time T_m fixes the spectral resolution to be $1/T_m$. This relation can be seen in figure a and b from Figure 3.10 of which the transformation of a Gauss curve from time to frequency domain is presented. Where T_m determines the range of the time based signal, F_s determines the range of the frequency domain. Furthermore, F_s determines the resolution of the time based signal as where T_m determines the resolution in the frequency domain. It must be noted that, by using algorithms such as the zero-padding method, ZoomFFT, Hilbert-transform... these relations can be manipulated in order to increase the resolution of the frequency spectrum [3, 9, 14]. Although the accuracy of magnitude and frequency of the frequency components can be increased, the bandwidth of the measurement always remains the same, defined by the sample-rate and measurement time. As these enhancing techniques consequently obstruct the proper interpretation, only the basic FFT algorithm is applied in this research. However, as will be handled in §3.3.1.3, another type of technique will be applied in order to obtain a very high accuracy in frequency and magnitude of the spectral components.

In most applications, the measured time signals contain a combination of sine functions, especially in electric applications. In that perspective, the visualization/-calculation of the negative frequency components by the FFT algorithm seems useless. However, if the FFT algorithm (3.2) is performed on a pure sine wave signal with frequency ω_1 , two components are visible in the spectrum. The frequencies $-\omega_1$ and ω_1 each with a half magnitude of the original signal. This is because

(3.2) states that the time signal can be constructed with a finite sum of factors following the form of $e^{-j \cdot x}$ (combination of sine and cosine functions, not only sine waves). Thereby, a sine function can be represented by those factors following Euler's formula:

$$A \cdot \sin(\omega \cdot t + \phi) = \frac{A}{2 \cdot j} \left[e^{j(\omega \cdot t + \phi)} - e^{-j(\omega \cdot t + \phi)} \right] \quad (3.3)$$

Consequently, a sine function analyzed by performing a DFT is always indicated by a negative and positive frequency component with half of the magnitude. As in this research only sine functions are considered, the negative spectrum is flipped at the positive side which is doubled in magnitude. Thereby, the obtained frequency spectrum as output of the algorithm $[0 : F_s/2]$ can be considered as an analysis of the frequency content of the signal following sine functions with frequencies that are multiples of $1/T_m$. That is how the spectrum is usually visualized by commercial spectral analyzers. As a consequence, it is commonly said that FFT represents the content of a signal as a sum of sine waves.

3.3.1.1 Aliasing

Based on the previous statements, the time signal can only be analyzed on the frequency content for frequencies up to $F_s/2$ [2, 3, 9]. This does not imply that frequency components above that limit won't be visible in the spectrum. By sampling a high-frequency signal with a rather low sample-rate, a new sine function arises out of the discrete components with a frequency equal to the sample-rate minus the original signal frequency. Consequently, those signals disturb the correct interpretation of the spectrum. When performing a DFT on a measured and sampled signal, the algorithm expects the signal to repeat itself every 'measuring time' (with fundamental period $1/T_m$). Subsequently, not only the time function is infinite, but also the frequency function is assumed to be infinite and repeats itself every F_s . The visualization of this statement is presented in Figure 3.10. A discrete Gaussian time function is measured for a specific time T_m and sampled with a frequency F_s (Figure 3.10.a). By applying a FFT on the time signal, it is assumed to be periodic with period T_m . The frequency transformation of a Gaussian curve is as well a Gaussian curve and is symmetric around the axis of 0Hz. As the signal is as well periodic in the frequency-domain, repeating every F_s in the frequency spectrum, overlap occurs. When the frequency content of the measured signal is smaller than $F_s/2$, no problem arises. When however the signal content exceeds the frequency $F_s/2$, like a Gaussian function does, the periodic frequency function overlaps (Figure 3.10.b). Thereby, the exceeding components are reflected on the axis of $F_s/2$. By oversampling the time signal (increasing F_s), the overlap can be avoided only when the frequency content of the signal is smaller than the half of the sample frequency. However, oversampling a Gaussian function is impossible, as the function has frequency components from minus infinity to infinity. However, Figure 3.10.c shows the reduction of overlap when the sample frequency is

increased. Usually, as it is rather unknown what the exact content of the signal is (especially on noise), the time sampling is directly followed by a digital filter. This filter is called an *anti-aliasing filter* and filters all components beyond $F_s/2$, avoiding any spectral overlap (Figure 3.10.d). As could be noticed in Figure 3.10.d, the components adjacent to the cut-off frequency of the anti-aliasing filter are deformed. The data acquisition equipment used in this research is standard provided with an integrated anti-aliasing filter. For the used acquisition card NI-9238, this anti-aliasing is performed by a Delta-Sigma filter. This is the combination of over-sampling and anti-aliasing. Specifically for NI-9238, the oversampling is done at $128 \cdot F_s$ ($\sim 6.5\text{MHz}$ for 51.2kHz). Subsequently, a digital filter is applied which has a pass-band at $\sim 0.453 \cdot F_s$ and a stop-band at $\sim 0.547 \cdot F_s$, presented in Figure 3.9. Finally, the signal is re-sampled to the sample-rate F_s . The frequency dependent gain in the pass-band (the *passband flatness*) is digitally countered. In order to deal with this attenuation due to the anti-aliasing filter and aliasing in general, the sample-rate is usually determined by multiplying the required frequency domain with the factor 2.56 [5]. So, if the relevant frequency range of DC to 2kHz has to be evaluated, the practical sample-rate is 5120Hz . This is how the nowadays vibration analyzers determine the sample-rate. In the application of measuring electrical current, is common to evaluate the harmonic content up to the 40st harmonic or 2kHz , [76]. Nevertheless, in this research stadium were storage space is not limited, spectral analysis will be conducted up to 20kHz , which sets $F_s = 2.56 \cdot 20\text{kHz} = 51.2\text{kHz}$ (maximum sample-rate of the NI-9238).

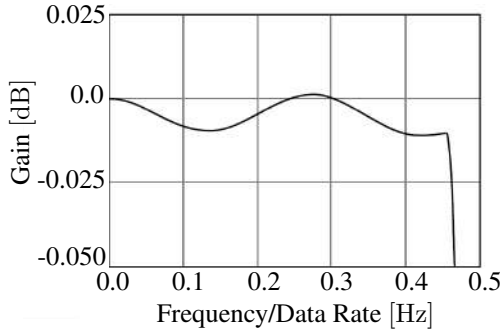


Figure 3.9: The frequency response function of the anti-aliasing filter in NI-9238 [8]

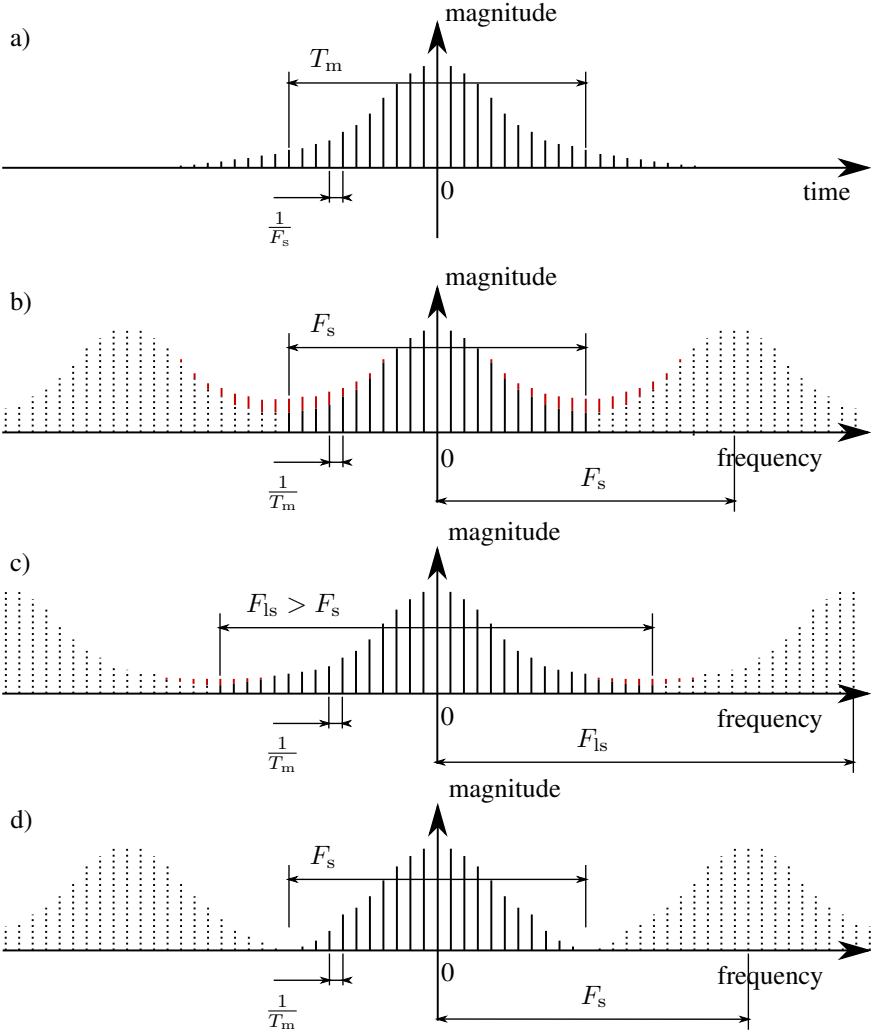


Figure 3.10: Visualization of the phenomenon aliasing. a) the gauss time function; b) the frequency function with aliasing (red bars); c) increasing the sample frequency reduces the overlap; d) applying an anti-aliasing filter resulting in no overlap

3.3.1.2 Leakage

So, by sampling a time signal defined by a specific measuring time frame T_m and a sample-rate F_s , the DFT algorithm assumes that the time signal is periodic with a fundamental frequency $1/T_m$. Thereby, following the basics of periodic function, the following equation should hold for every measured signal $y(t)$ with time t :

$$y(t) = y(t + T_m) \quad (3.4)$$

This equation can only hold if the frequency of the measured signal is either equal or a multiple of $1/T_m$. Unfortunately, when measuring a real time based signal with fundamental frequency f_x , it is statistically impossible that f_x is an exact multiple of $1/T_m$. This is because f_x is always an irrational number (infinite numbers by the comma). Therefore, the measured signal can never be periodic with period T_m . As the DFT expects the time based signal to be a periodic function with a period T_m , an error is inevitably introduced in the spectrum commonly addressed to as *Leakage* [2, 3, 9]. It must be noticed that this leakage phenomenon can also be introduced for functions with rational frequencies if T_m is no multiple of the signal's period. For example, regarding a signal of 50Hz which is measured for $T_m = 1.234s$, the formula (3.4) does not hold and inevitably introduces leakage in the frequency spectrum.

This phenomenon is graphically clarified by Figure 3.11. In Figure 3.11.a, a sinusoidal time signal with frequency f_x is measured for a measuring time T_m , which is a multiple of $1/f_x$. Therefore, leakage can not be found in the corresponding spectrum. In Figure 3.11.b, a realistic example is given, where $1/f_x$ is not a multiple of T_m . As a consequence, spectral leakage is appearing in the spectrum. Those additional spectral components are formed because the time signal is not a smooth, infinite function anymore. The time based phase shift is a discontinuity in the time function. The solution to this unavoidable implication can be found by applying *windowing* of which this method is graphically presented in Figure 3.11.c. The time signal is thereby multiplied with a specific function with length T_m , directly implying the exact periodicity of the total signal. With this multiplication, (3.4) hold for any captured signal. Due to this implication, the leakage in the frequency spectrum is minimized. The so called *window-function* can be chosen as a function of the purpose of the analysis. Table 3.4 gives an overview of the most commonly applied windows and their main specifications. In that table, it can be observed that every window introduces a specific error in frequency (*Noise bandwidth*) and an error in magnitude (*Max. magnitude error*) in the spectrum. In this research, as the accuracy of both frequency and magnitude is equally important, the *Hanning window* is applied on every frequency transformation.

Window type	Sidelobe roll-off [dB/decade]	Noise bandwidth rel. to line spacing	Max. magnitude error [dB]
<i>Rectangular</i>	-20	1.00	3.9
<i>Hanning</i>	-60	1.50	1.4
<i>Hamming</i>	-20	1.36	1.8
<i>Kaiser-Bessel</i>	-20	1.80	1.0
<i>Truncated Gaussian</i>	-20	1.90	0.9
<i>Flat-top</i>	0	3.77	<0.01

Table 3.4: Commonly applied types of window, [3, 9]

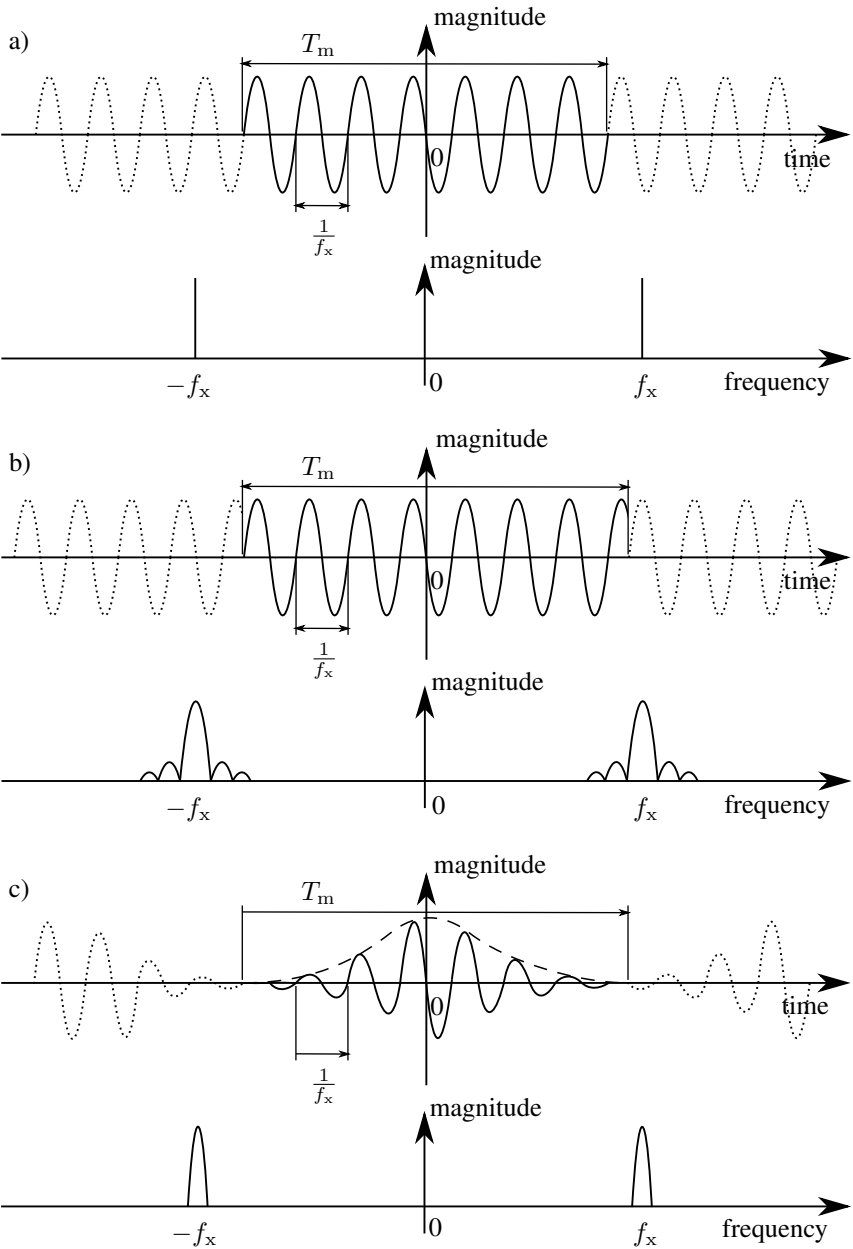


Figure 3.11: Visualization of the phenomenon leakage. a) the time signal where T_m is a multiple of $1/f_x$; b) an example of the unavoidable leakage in the spectrum; c) reducing the leakage in the spectrum by applying a Gaussian window on the time signal

3.3.1.3 Picket fence effect

Another disadvantageous phenomenon called the *picket fence effect* is also introduced in the spectrum by the inherent irrational character of any real captured signal [2, 3, 9]. As discussed, it is statistically impossible to measure a fundamental frequency which is exactly equal to a specific frequency component in the spectrum. Therefore, the measured component is always divided between two components. The resolution of the spectrum could be increased by taking more samples (measuring longer), but this never eliminates the picket fence effect. On the contrary, increasing the resolution could be disadvantageous. For example: when a fictional 50.050000... Hz sine wave is measured for 1s (spectral resolution of 1Hz), a maximum error of 0.66% is introduced due to the spectral division of the component between 50Hz and 51Hz (using Hanning window). By increasing the resolution by measuring for 10s (spectral resolution of 0.1Hz), a maximum error can be reached up to 15.15% [2]. This because the component is now divided between 50.0Hz and 50.1Hz. As measured signals are inevitably irrational frequencies, the infinite series of numbers by the comma are unknown, the accuracy of the displayed spectral component can vary between 0% and 15.15% (using Hanning window).

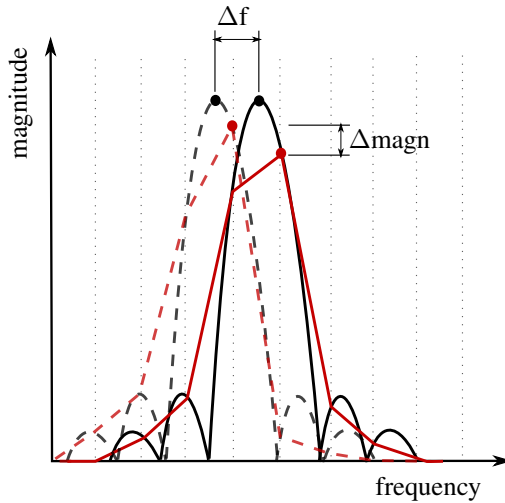


Figure 3.12: Incorrect magnitude interpretation for two measurements (striped lines and solid lines) with minor frequency deviation due to the picket fence effect. The red line is the discretized spectrum and the black line is the transform using zeropadding, enhancing the spectral resolution [2, 3].

Furthermore, in terms of condition monitoring, there is a need of comparing the magnitudes of two frequency spectra on different moments in time. If a minor frequency variation occurs between the same components of the two measurements e.g. due to inevitable variations the rotational speed, the picket fence effect interferes with the correct interpretation of magnitudes. This phenomenon is pre-

sented in Fig. 3.12. In this research, an interpolation method is used based on the magnitudes of the adjacent peaks to calculate accurately the magnitudes and frequencies [4]. This interpolation method fits a *sinc* function on the spectral peaks of interest and their adjacent components. This is because the spectral presentation of the applied Hanning window corresponds to a *sinc* function. Due to the interpolation method, the accuracy of the magnitude/frequency calculation in the spectrum is no longer dependent on the resolution of the spectrum or measurement time. The required minimal resolution of the spectra is now determined by the proximity of two adjacent components in the spectrum of which the magnitude is valuable. The spectral resolution must be kept high enough so that two components of interest do not merge into one frequency component (long measurement time). Nevertheless, the spectrum resolution may not be too high so that a minor frequency variation during the sampling period results in splitting up one component in several components (spread spectrum effect). This occurs frequently when measuring rotating machines as the speed varies during the measurement time. Those requirements result in a crucial part of capturing the stator current: measure the current with a stable frequency and magnitude. If the sampled data is not stable, the magnitudes of the current components are easily spread or deformed in the spectrum (even with the minimum required resolution) [3, 9]. The challenge is to accurately determine the perfect sample-rate and measuring time so that the content which must be analyzed is correctly presented. This will be handled in the following chapter, determining the machines stable operation point in order to perform the frequency analysis.

3.4 Practical implementation

Now the stator current measuring method, setup and the theoretical background of the applied signal processing techniques were handled in the previous sections, the measuring procedure and corresponding algorithms can be elucidated. The current signal is measured with the use of the *Fluke® i400s* current clamps in combination with the *National Instruments™ Compact DAQ* card: *NI9238*. The data is directly acquired in the mathematical software *Matlab®*. In this software, all processing algorithms regarding frequency analysis and signal conditioning are performed. The use of this environment ensures that every digital signal processing step is fully under control. In this way, all phenomena occurring due to the DFT e.g. aliasing, leakage and the picket fence effect can be properly encountered. Additionally, a peak search tool is programmed in order to match fault related frequency components with the measured spectrum. After performing the measurement and providing the necessary properties and conditions, a graph and table is generated presenting a spectral analysis with fault related diagnoses.

3.4.1 Digital signal processing

First, the electrical measurement is conducted whereby the relevant data is imported in *Matlab®*. The required control language is provided by *National Instruments™* to use in *Matlab®*. Thereby, the raw data is directly available for analysis and processing. As mentioned in the previous section, aliasing is excluded by using these NI DAQ-cards with integrated anti-aliasing filter (Delta-Sigma-filter). The code directly provides the current time signal of the four current clamps connected to the *NI-9238* card with a clearly specified sample-rate and number of samples (\approx measuring time). In order to perform the frequency analysis, *Abravibe* toolbox is applied [9]. With the use of this toolbox, the FFT is obtained. To avoid leakage, a Hanning window is applied on the time based waveforms. It must be noted that the commonly applied *averaging* and *overlap* while performing a frequency transformation are intentionally ignored in this dissertation. By splitting the time signal into frames and average the frequency spectra of each frame, a lot of time varying information is lost. In practice, it is widely applied in order to obtain a more stable and reproducible frequency spectrum. By doing this, the analyst has the impression that a non time varying signal is measured. However, these stabilizing techniques can easily result in the disappearance of valuable information or phenomena. For example, if a frequency component appears for 0.5s during a measuring time of 10s and it is subsequently transformed to the frequency domain with an averaging of 10 and 50% overlap, this component will be hardly visible in the averaged spectrum [3, 5]. As in this research reflections of specific time based signatures have to be found where time variety is crucial, *averaging* and *overlap* are not applied. Thereafter, the picket fence effect is countered by the interpolation method described in [4]. This method is based on the two adjacent frequency components which would be one component in a continuous frame but

are divided due to the picket fence effect (as in Figure 3.12). Based on the relative difference in magnitude, a correction in frequency and magnitude is calculated. As the magnitude and frequency interpolation can only be applied on the present frequency components and not on every discrete sample, an automatic peak detection algorithm is required. This algorithm searches in the obtained spectrum for components which are larger than their adjacent peaks (not necessarily the maximal ones). On every peak and the second largest adjacent peak, the interpolation algorithm is applied. This is graphically presented in Figure 3.13. By using those simple algorithms, an accurate FFT function is obtained. With this method, every signal whether it is current, voltage or vibration, can be presented in the frequency spectrum with high accuracy. This algorithm was extensively validated within the software environment as well as with practical measurements. Performing the validation, it was noticed that most commercially available frequency analyzers are not provided with this interpolation algorithm, which can cause significant errors in interpretation as presented in §3.3.1.3.

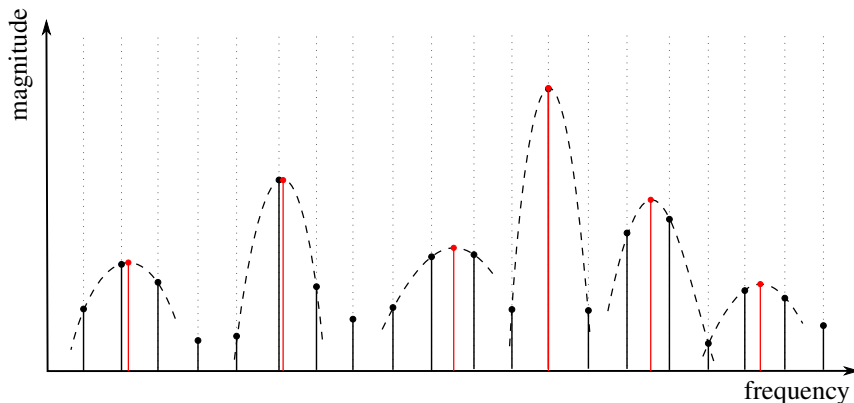


Figure 3.13: The black spectral lines are the original spectrum, the striped line is how [4] interpolates to the real magnitude and frequency. The red spectral lines are the used components in the analysis.

3.4.2 Current analysis tool

To facilitate the research, a tool is created in order to automatically analyze the machine stator current with the focus on MCSA. More specific, the previously established frequency analysis and the fault indicating current components mentioned in §2.3 are combined in an automatic generated frequency graph. An overview of the fault indicating components included in the diagnostic algorithm is given in Table 3.5. To minimize the input arguments of the tool, an automated current based speed detector is integrated, as discussed in §2.3.2.2, described in (2.7) and graphically presented in Figure 2.7. Thereby, only time based voltage and current signals must be provided to the tool together with some machine properties e.g. bearing

information, number of pole pairs and number of rotor slots. The speed estimator is based on the unavoidable mass-unbalance, eccentricity and geometric imperfections in electric machinery. Due to that unbalance, an ever present air gap variation at rotor speed implies a modulated sine wave on the fundamental frequency. As the detection method uses rather low-frequency components, the speed estimation is not disturbed by using a frequency converter. The fault analysis function contains the search to fault related frequencies in the current spectrum. In that function, the pre-calculated fault frequencies listed in Table 3.5 are matched with the real frequency components in the obtained frequency spectrum. It must be noted that for some faults, e.g. static eccentricity and inner race bearing fault frequencies, sidebands at f_r are included as fault frequencies. It is convenient for the analyst to be able to address every highlighted peak to a specific indicator. To facilitate the user interface, a table is outputted with a list of all faulty components with their corresponding calculated fault frequency, detected fault frequency, magnitude and harmonic relation. Additionally, a plot is formed with an interactive pointer, listing all possible diagnosis on every fault related peak. An example is presented in Figure 3.14. Some of the data tips are highlighted with their corresponding interpretation in the spectrum.

Fault diagnose	Formula
Stator winding shortcut	$f_{st} = k \cdot f_r \pm v \cdot f_1 $
Broken rotor bar	$f_{bar} = f_1 \pm 2 \cdot k \cdot s \cdot f_1 $
Static rotor eccentricity	$f_{eccs} = n_{rs} \cdot k \cdot f_r \pm v \cdot f_1 $
Dynamic rotor eccentricity	$f_{eccd} = (n_{rs} \cdot k \pm n) f_r \pm v \cdot f_1 $
Mixed rotor eccentricity	$f_{eccm} = f_1 \pm k \cdot f_r $
Bearing inner race defect (BPFI)	$f_{in} = \left f_1 \pm k \left[\frac{n_b}{2} f_r \left(1 + \frac{bd}{pd} \cos \beta \right) \right] \right $
Bearing outer race defect (BPFO)	$f_{out} = \left f_1 \pm k \left[\frac{n_b}{2} f_r \left(1 - \frac{bd}{pd} \cos \beta \right) \right] \right $
Bearing ball defect (BSF)	$f_{ball} = \left f_1 \pm k \left[\frac{pd}{2 \cdot bd} f_r \left(1 - \left[\frac{bd}{pd} \cos \beta \right]^2 \right) \right] \right $
Bearing cage defect (FTF)	$f_{cage} = \left f_1 \pm k \left[\frac{1}{2} f_r \left(1 - \frac{bd}{pd} \cos \beta \right) \right] \right $
Electrical harmonics	$f_{harm} = h \cdot f_1$

Table 3.5: The calculated spectral fault diagnosing frequencies as was presented in §2.3

where:

f_1	fundamental current component [Hz];
f_r	rotational speed frequency [Hz];
s	slip [-]
k	harmonic integer 1, 2, 3, 4 . . . ;
v	harmonic integer 1, 3, 5, 7 . . . ;
n	harmonic integer 1, 2, 3, 4 . . . ;
n_{rs}	the number of rotor slots [-];
n_b	number of bearing balls [-];
bd	ball diameter [mm];
pd	pitch diameter [mm];
β	bearing contact angle [rad];
h	harmonic integer 2, 3, 4, 5 . . .

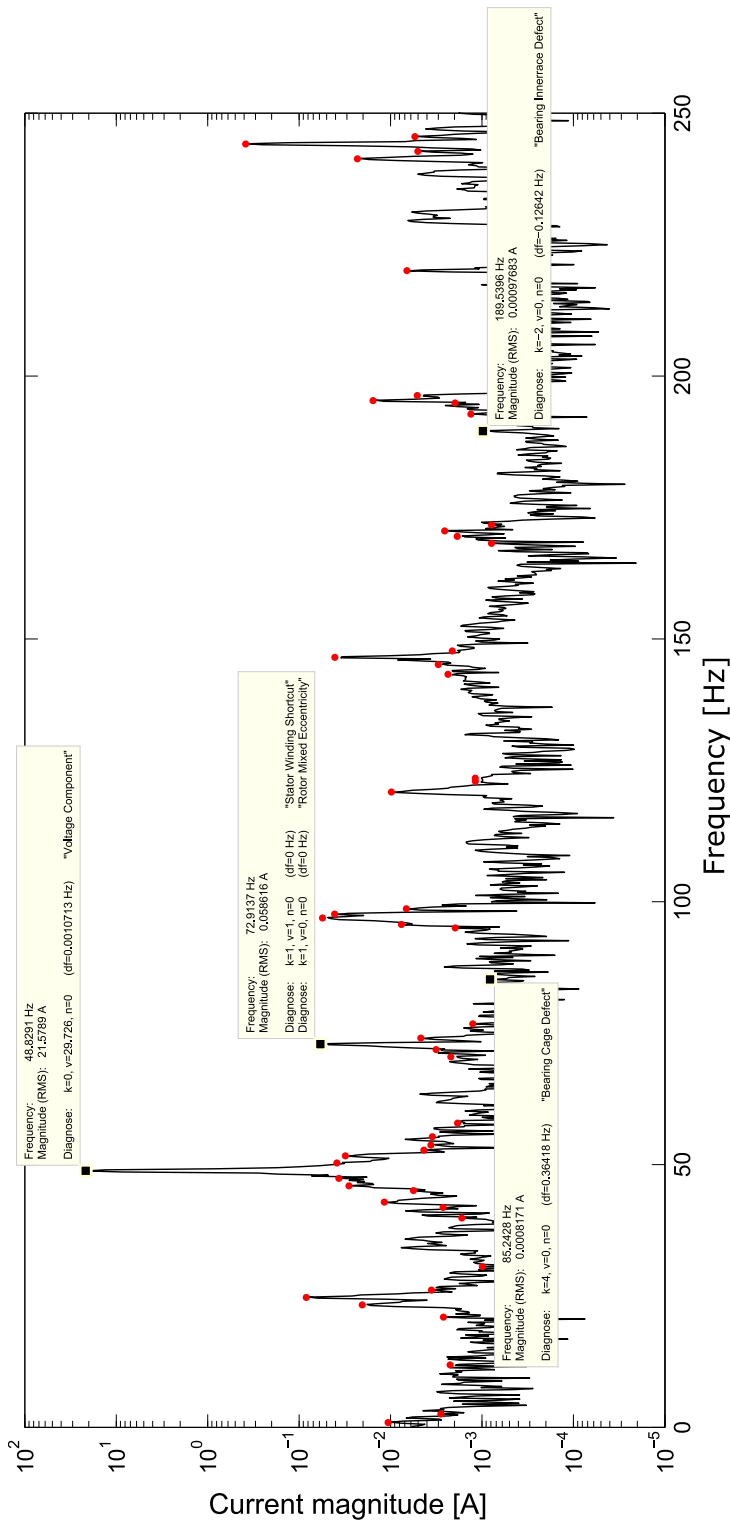


Figure 3.14: Example of a generated plot by the current analysis tool, included with corresponding diagnosis for every fault related frequency component

3.4.3 Case study

As the stator current analysis tool is ready to be used, some feasibility tests can be performed. More specific, it is interesting to verify the possibility of detecting mechanical faults e.g. a bearing fault by analyzing the stator current via the previously described algorithms. Condition based measurements are performed in the context of an industrial assignment on an IM which drives a fan in order to draw some exhaust gases from an industrial production process. The torque and speed of the machine is controlled as a function of the amount of gases that have to be removed. Therefore, a frequency converter is installed to control the IM. The converter is located on $\pm 100\text{m}$ away from the IM, resulting in overvoltages and probably induced bearing currents in the machine [77]. Consequently, there is a strong suspicion for a damaged bearing due to electro pitting and subsequently mechanical pitting. The drive train consists of an IM with the following properties: 980kW; 690V; 50Hz; 4 poles (1500rpm); driver fed. The fan is connected to the machine via a bearing supported shaft (see Figure 3.15). The relevant properties of the bearings implemented in the IM are:

pitch diameter (pd):	180mm
ball diameter (bd):	31.75mm
ball contact angle (β):	0°
number of bearing balls (n_b):	9

With these properties, the fault related frequencies in order to perform the MCSA are calculated following the formulas obtained in §2.3 and Table 3.5. In order to create a certain reference to compare the measurements and diagnostics, vibration analysis is complementary included in this test case. Thereby, the faulty frequencies presented in Table 2.2 are calculated as well.

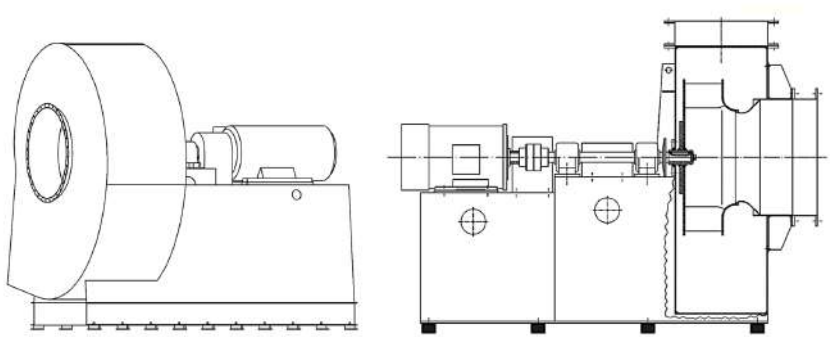


Figure 3.15: Schematic presentation of the measured drive train

The measured machine bearing at Non Drive End (NDE) is electrically isolated from the stator housing with an aluminum oxide coating (Al_2O_3). This is commonly done in applications using frequency converters, in order to prevent

circulating bearing currents. As thereby the biggest chance of actual bearing problems is at DE-side, the accelerometer is placed at DE-side, as close as possible to the *weakest* bearing (shortest fault propagation path). The following properties are inherent to the used accelerometer:

Sensitivity:	100mV/ g
Bandwidth:	1Hz – 10kHz
Range:	$\pm 50g$

The current and vibration are obtained as described previously in this chapter. Only a few seconds of data is needed in order to gain a sufficient frequency resolution which avoids merging of valuable frequency components [5]. However, to make sure that the used data is stable under the varying load conditions, 5min of data is logged and saved locally. The varying RMS current and the fundamental frequency of the stator current in those 5min are calculated from the current samples and are presented in Figure 3.16a and 3.16b. Those two signals provide clear information about the load conditions and variations of the drive-train during measurement. In this way, it can be determined which time frame is stable enough to analyze. This is important so that the small frequency variation of f_r or f_1 during the analyzed time frame would not spread out important frequency content within the spectrum (spread spectrum). Still, the resolution remains high enough to avoid the merging of two valuable components. Out of Figure 3.16a and 3.16b, the data is determined to be stable enough to analyze between the time stamps [65s, 105s] and [130s, 185s] (minimal frequency and magnitude variations). In Figure 3.16b, the frequency variations which can cause spread spectrum are visualized. Thereby, the maximum spectral resolution and so the length of the time frame is determined. In the stable dataset, e.g. [65s, 105s], the frequency still varies $\pm 0.1\text{Hz}$, which should result in a spread out frequency component if the resolution of the frequency spectrum was chosen higher than 0.1Hz. This means that the time frame should be $< 10\text{s}$. As the minimum resolution for the analysis should be 0.2Hz in order to differentiate between the fault indicating frequency components, a time frame of 5s is applied in this analysis.

First, vibration analysis is performed. The spectral results are found in Figure 3.17a with the fault frequencies indicated by a bullet. The more detailed information of the fault frequencies is listed in Table 3.6. Diagnosing the vibration spectra, it becomes clear that there is some serious bearing damage at DE of the induction machine. The dominant fault is a bearing inner race defect, but the presence of the outer race, ball and cage fault frequencies indicates that the fault is already in an advanced state [5, 44]. To confirm the stage of the bearing fault, the RMS velocity of the vibration between 10Hz and 1kHz are compared with the ISO 2372 (10816) standard [5]. Out of those calculations (4.53mm/s), the machine is classified as *zone C*. This means that the machine may run for a limited period, but it is unsatisfactory for long-term continuous operation. Regarding the state of the bearing, the

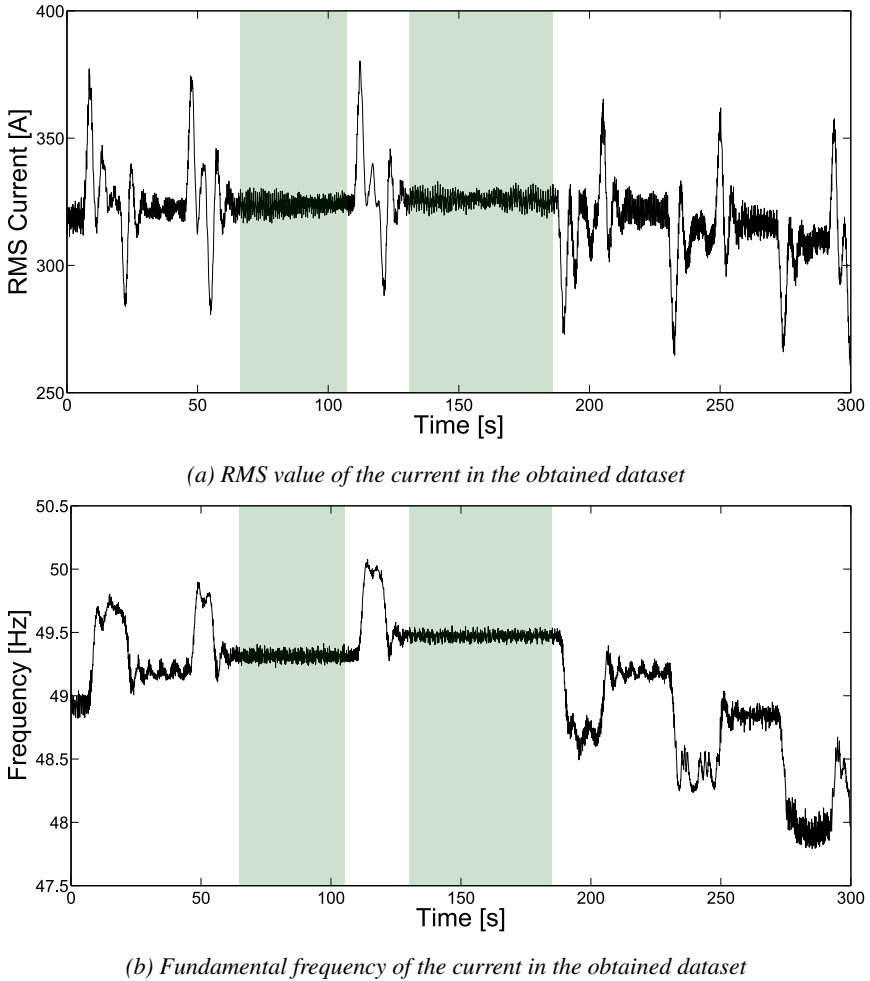
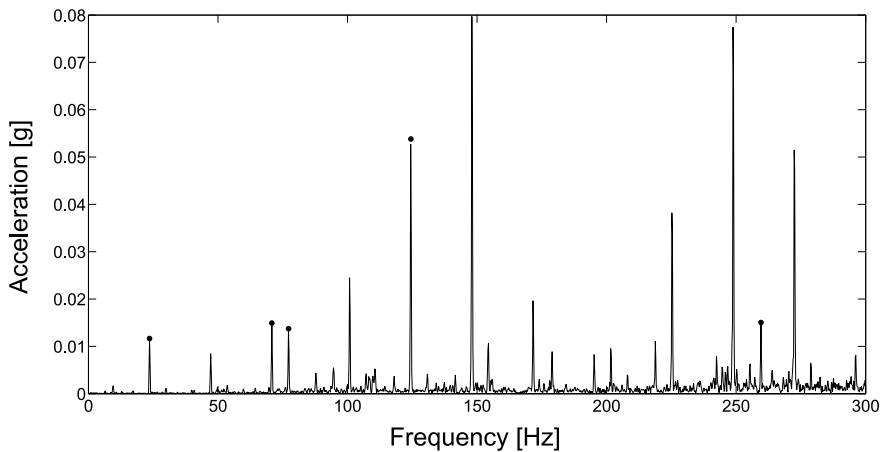


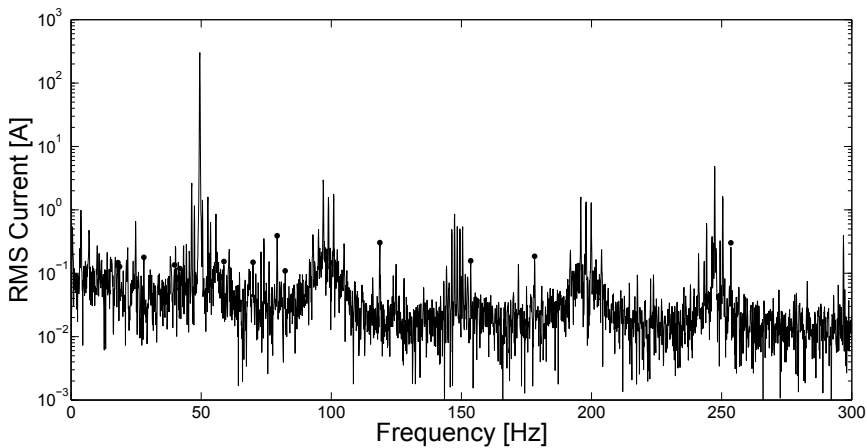
Figure 3.16: Searching for stable operational moments in time (torque and speed)

fault should definitely be detectable by the MCSA method. The current spectrum analysis can be found in Figure 3.17b. The detailed analysis is presented in Table 3.7. The current analysis also indicates the bearing problems. For MCSA, it is impossible to distinguish between the bearing at DE and at NDE if the bearings have the same dimensions. However, as the vibration analysis of the DE bearing and the current spectrum both indicate some bearing issues, it is most likely that the problems are in fact occurring at DE. The current spectrum is additionally indicating all kinds of bearing faults (ball, inner race, outer race, cage). This confirms an advanced bearing problem. To be sure about the stage or severity of the bearing fault, the magnitudes of the frequency components should be evaluated.

This preliminary case study confirms that the signal analysis satisfies the requirements. The small fault related frequency components can be found in the



(a) Vibration spectrum



(b) Current spectrum

Figure 3.17: The spectra of vibration and current of the machine under test

current spectrum. Thereby, the hardware and software topologies are confirmed to be valid. Additionally, the problem statement made in §1 is confirmed as well. Although many articles are published about this topic [22–24, 28, 34, 36, 37, 75, 78–80], the magnitudes of the mechanical fault indicating frequency components in the stator current still do not provide sufficient information about the bearing fault's severity. Therefore, this case study indicates that further research about the relation between the motor current fault components and the bearing state is needed. The following chapters in this dissertation will completely focus on finding relations between evolving mechanical faults and their reflection in the stator current by experimental research.

Indicated fault	Frequency [Hz]	Magnitude [mg]	Order k [–]
Bearing cage	9.72	1.88	1
Rotor eccentricity	23.60	11.65	1
Bearing cage	29.16	1.26	3
Rotor eccentricity	47.20	8.44	2
Bearing ball	64.81	1.18	1
Rotor eccentricity	70.80	14.93	3
Bearing outer race	87.46	4.36	1
Bearing inner race	124.93	53.80	1
Bearing ball	129.63	1.50	2
Bearing outer race	174.93	2.29	2
Bearing ball	194.44	8.34	3
Bearing inner race	249.86	5.48	2
Bearing outer race	262.40	1.25	3

Table 3.6: Detailed information from the vibration fault frequencies as in Table 2.2

Indicated fault	Frequency [Hz]	Magnitude [mA]	Order k [–]
Bearing ball	18.23	146.9	–1
Bearing cage	19.01	127.1	–3
Bearing cage	29.16	178.0	–2
Bearing cage	39.31	135.0	–1
Bearing outer race	41.89	118.5	–1
Bearing cage	59.61	153.0	1
Bearing cage	69.76	149.0	2
Bearing cage	79.92	391.1	3
Bearing inner race	81.02	109.1	–1
Bearing ball	117.16	304.4	1
Bearing ball	153.63	157.1	–3
Bearing inner race	179.96	185.1	1
Bearing ball	252.57	302.0	3

Table 3.7: Detailed information from the current fault frequencies as in §2.3

3.5 The Extended Park Vector Approach

Although previous measurements and sections only indicated the classic line current spectral analysis as it is found in literature, different on-line methodologies can be applied in order to identify fault related components in the stator current. Examples are analyzing the line spectra, the power density spectrum, the positive/negative/zero-sequences, the Park vector... as discussed and compared in [67, 81, 82]. In this dissertation, the Extended Park Vector Approach (EPVA) is applied on all further analysis [67]. The EPVA consists of a demodulation technique which further simplifies the spectral analysis of the electrical current. As can be noted in Table 3.5, all mechanical fault frequencies are modulated on the fundamental current component f_1 . This implies that every mechanical fault frequency is visualized in the spectra twice: once as positive sideband and once as the negative sideband. By performing the demodulation on the fundamental frequency ω_1 , all fault frequencies are visible as one solid component which represent the original fault forcing frequency. This approach consists of the transformation of the three phase line currents by the Clarke and Park transform, illustratively presented in Figure 3.18.

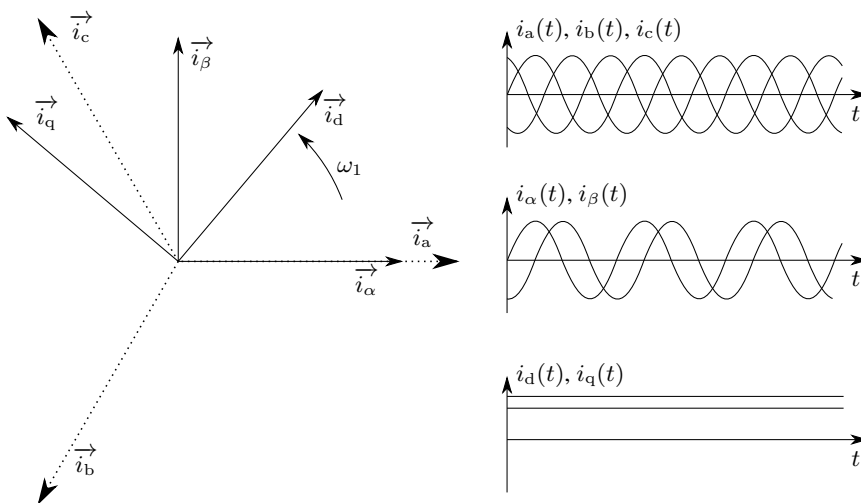


Figure 3.18: The graphic interpretation of the Clarke Park transform

By applying the power invariant Clarke transform on the three phase currents $i_a(t)$, $i_b(t)$ and $i_c(t)$, the three axes coordinate system is transformed to an orthogonal coordinate system of which $i_\alpha(t)$, $i_\beta(t)$ and $i_\gamma(t)$ are the time varying coordinates, [67, 83]:

$$\begin{bmatrix} i_\alpha(t) \\ i_\beta(t) \\ i_\gamma(t) \end{bmatrix} = \sqrt{\frac{2}{3}} \begin{bmatrix} 1 & -1/2 & -1/2 \\ 0 & \sqrt{3}/2 & -\sqrt{3}/2 \\ 1/\sqrt{2} & 1/\sqrt{2} & 1/\sqrt{2} \end{bmatrix} \begin{bmatrix} i_a(t) \\ i_b(t) \\ i_c(t) \end{bmatrix} \quad (3.5)$$

By performing the Park transform on the two dimensional currents $i_\alpha(t)$ and $i_\beta(t)$

($i_\gamma(t)$ is considered as the zero-sequence component), a rotating coordinate system is applied at speed ω_1 . This speed is the fundamental current frequency ($\omega_1 = 2\pi \cdot f_1$). This results in the essence of the technique: the demodulation, see Figure 3.18. The Park transform outputs a direct, quadrature and zero component $i_d(t)$, $i_q(t)$ and $i_z(t)$ expressed as, [67, 83]:

$$\begin{bmatrix} i_d(t) \\ i_q(t) \\ i_z(t) \end{bmatrix} = \begin{bmatrix} \cos(\omega_1 \cdot t) & \sin(\omega_1 \cdot t) & 0 \\ -\sin(\omega_1 \cdot t) & \cos(\omega_1 \cdot t) & 0 \\ 0 & 0 & 1 \end{bmatrix} \begin{bmatrix} i_\alpha(t) \\ i_\beta(t) \\ i_\gamma(t) \end{bmatrix} \quad (3.6)$$

The resulting signals $i_d(t)$ and $i_q(t)$ are combined to the EPVA vector, $i_e(t)$, by the following expression, [67, 82, 83]:

$$i_e(t) = \sqrt{i_d(t)^2 + i_q(t)^2} \quad (3.7)$$

Eventually, the time-varying signal $i_e(t)$ is analyzed in the frequency domain in the search for rotor related problems in the IM. Regarding bearing faults, the fault related frequency components are simplified to these following formulas as in Table 2.2:

$$f_{\text{out}} = k \cdot \frac{n_b}{2} f_r \left[1 - \frac{bd}{pd} \cos\beta \right] \quad (3.8)$$

$$f_{\text{in}} = k \cdot \frac{n_b}{2} f_r \left[1 + \frac{bd}{pd} \cos\beta \right] \quad (3.9)$$

$$f_{\text{ball}} = k \cdot \frac{pd}{2 \cdot bd} f_r \left[1 - \left(\frac{bd}{pd} \cos\beta \right)^2 \right] \quad (3.10)$$

$$f_{\text{cage}} = k \cdot \frac{1}{2} f_r \left[1 - \frac{bd}{pd} \cos\beta \right] \quad (3.11)$$

These fault frequency calculations are now exactly the same as for vibration analysis (see Table 2.2, Chapter 2), which simplifies the spectral analysis significantly [67]. This EPVA is applied on most measurements in Chapter 6, where the experiments on mechanical faults are conducted.

3.6 Conclusion

This chapter was focused on measuring and analyzing the stator current, corresponding to the first defined goal in this overall research, see Chapter 1. Although this chapter did not result into a major contribution to the field of current measurements, this research is needed in order to fully comprehend the errors and phenomena linked to the spectral interpretation of time based current signals. By conducting experiments on the detection of small frequency components carried on a large fundamental current component, it is concluded that a cheap, commercially available current clamp measures with a sufficient accuracy to perform CM based measurements. Subsequent to digitally acquiring the time based voltage signals out of the current clamps, an anti-aliasing filter is applied (via a Delta-Sigma filter) in order to prevent high frequency components disturbing the low-frequency spectra. Applying the DFT - FFT algorithm, the frequency spectra of any signal can be obtained with high accuracy due to a proper fitted window and an advanced interpolation algorithm. Thereby, the disadvantageous phenomena leakage and picket fence effect are countered and suppressed. By fitting specific pre-calculated fault frequencies on the obtained stator current spectra, the machine condition can be diagnosed automatically with the focus on electrical and mechanical problems. The whole topology and signal processing algorithm was validated by the detection of an inner race bearing fault of an industrial IM of 980kW. In further analysis, the EPVA is applied because of the gained simplicity in analyzing the spectral content with the focus on mechanical phenomena. This is because most mechanically induced faults are modulated on the fundamental current component, unnecessarily confusing the spectral analysis. As the stator current analysis algorithm was successfully completed in this chapter, further chapters handle the experimental mechanical fault emulation and the corresponding spectral analysis of the stator current.

4

Mechanical fault manifestation

4.1 Introduction

The intention of the fault emulating test-rig is to manipulate the rotor position with respect to the stator position. By doing this, fault related rotor movements can reproducibly be imposed on an electric machine while analyzing the stator current. To do so, the mechanical bearing at drive end side from an 11kW induction machine will be replaced by an Active Magnetic Bearing (AMB). This bearing takes over all functionalities of the original bearing and additionally creates the fault related rotor movements. The dimensioning and construction is handled in the next chapter, because the dynamic response of the AMB is dependent on the required fault related rotor movements. Therefore, this chapter is fully focused on the impact of all kinds of mechanical faults on the rotor movements of an IM. As the mechanical faults being considered in this thesis are detectable in the stator current by unique frequency components, they all imply a specific rotor movement with respect to the stator (MCSA requires a variation in air gap). The consequence of using an AMB to emulate some mechanical faults is that rotor bow must be neglected, because with the AMB only one radial degree of freedom can be obtained at DE-side. However, regarding small induction machines, rotor bow can assumed to be negligible [1, 84].

In following sections, the movement of the rotor is theoretically approached for misalignment, unbalance and bearing faults under variable conditions such as bearing parameters, stiffness, damping properties and fault severity. No literature can be found on this exact definition of specific fault related rotor movements and their propagation within electric machinery. This mainly because these movements are only considered valuable in this specific application where they can be served

as set-points for the magnetic bearing. This chapter contains the construction of a unique analytical model which can obtain the specific rotor movements for most mechanical faults detectable in the stator current. As a consequence, the research proposed in the following sections within this chapter is completely unique and considered to be a significant contribution to the development of CM-systems in general. This because, next to MCSA, other technologies e.g. vibration analysis can benefit from these calculation due to the translatability to e.g. stator house acceleration profiles.

4.2 Rotor eccentricities

Eccentricity is an unavoidable phenomenon in rotating electric machinery. First, a distinction is made between static and dynamic eccentricity, visualized in Figure 4.1 and described in [27, 61, 63, 66]. Regarding static eccentricity, the rotor is rotating around its own gravitational center, but is deviated with respect to the center of the stator. This is a constant deviation. The rotor does not move around with respect to the stator. Regarding dynamic eccentricity, the rotational center is equal to the center of the stator, but the rotor center is deviated with respect to the center of the stator. This implies that the rotor position with respect to the stator is constantly varying following a circular movement. Once an eccentricity occurs which is a combination of both static and dynamic eccentricity, it is called mixed eccentricity. However, both static and dynamic eccentricity are mainly imposed by respectively excessive static and/or dynamic radial forces on the machine bearings, [27, 63, 66]. Once the bearings fail due to that load, the rotating machine will break down and -depending on the application of the equipment- serious economic damage can be caused. A few examples of excessive radial overload and its consequences are presented in Figure 4.2, [1]. As a consequence, excessive radial forces and eccentricities should be avoided in any rotating application as they are a main indirect cause of failure [1].

Radial forces are commonly generated by any belt, chain or gear transmission. However, if the machine is correctly dimensioned for its application, this should not cause unacceptable eccentricities. The main causes of excessive eccentricity can be found in misalignment and mass-unbalance. Because of misaligning one machine with another (or one rotor with another), unpredictable and mainly underestimated radial forces are exposed on the bearings of both machines. In addition, mass-unbalance can cause as well significant dynamic radial loads and thereby rotor eccentricities. Furthermore, once an eccentricity (static or dynamic) is imposed onto the machine, the Unbalance Magnetic Pull (UMP) severely increases the magnitude of the eccentricity, [63, 85]. As these two main causes of eccentricity can easily induce serious trouble with the machine robustness and reliability, detecting misalignment and mass-unbalance on industrial drive trains is very valuable. Consequently, in the industrial and academic field, a lot of effort has been made in order to detect eccentricities on several ways: vibration analysis, current signature analysis, acoustic analysis, flux analysis... [1, 86]. As this thesis focuses on the application of MCSA, only relations between eccentricity and its reflection in the stator current is examined. The following sections handle respectively the induced rotor movement when misalignment and mass-unbalance occur. The rotor deviation (or eccentricity) is analytically expressed in such a way that the severity of the fault can be increased easily on the test-rig while the current signatures are analyzed.

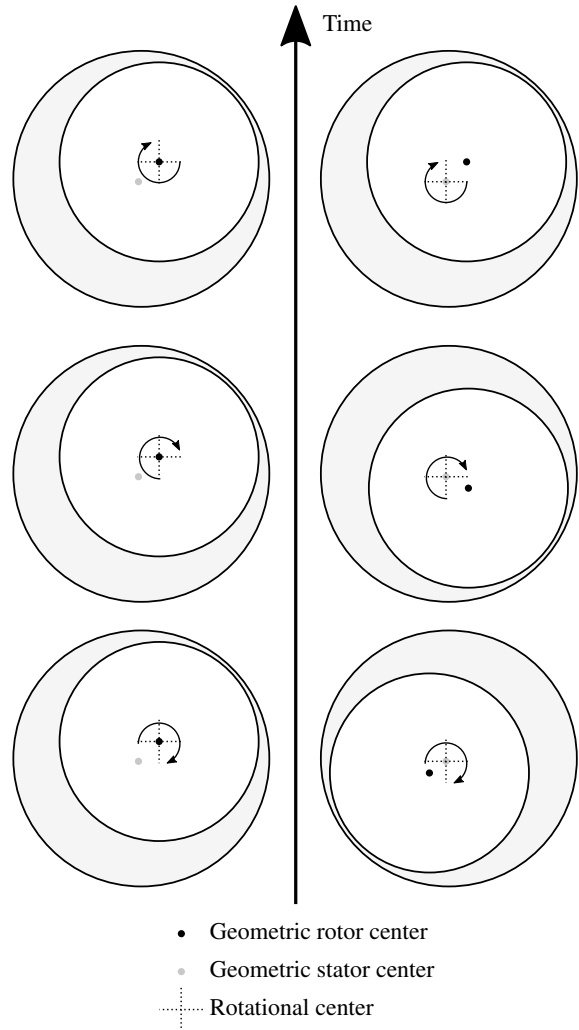


Figure 4.1: Static eccentricity (left) and dynamic eccentricity (right)

4.2.1 Misalignment

Misalignment is a term given to the error in the alignment between two rotating shafts, which is commonly used in positioning electric machines coupled with a load machine (fans, gearboxes, pumps...). Misalignment is divided in three main categories: parallel (or lateral), angular and combined misalignment. Those groups can each be subdivided by the horizontal and vertical misalignment. Figure 4.3 represents these groups of misalignment in a two-dimensional plane. Misalignment does not directly imply a failing of one of the coupled rotating machines, but the bearings of the coupled machines can be subjected to heavy static and/or dynamic loads which can easily result into an unexpected premature failure. It has



Figure 4.2: Excess of radial forces can have a serious impact on rotating machinery, [1]

to be noted that, in every application, combined misalignment is always present as perfect alignment is practically nonexistent. Nevertheless, it is comprehensible that a small amount of misalignment does not directly threaten the condition of the machine. Consequently, a lot of companies have built (mostly based on experience) tolerance tables in order to quantify the acceptance of angular and parallel misalignment [86]. However, industrial experience showed that the perfect alignment can cause the bearings to malfunction, as they need a certain amount of preload in order to make the rolling elements to rotate. Several cases of bearing failure are known where a lack of preload disabled the grease functionalities and overheated the bearing dramatically [1, 86].

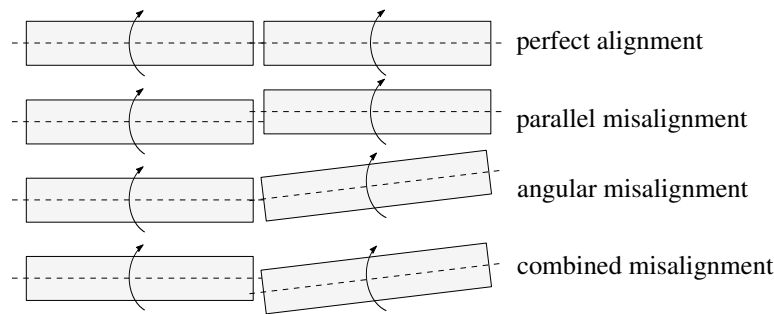


Figure 4.3: Misalignments of two rotating shafts

Emulating misalignment in an academic environment is technically possible by rearranging the IM in reference to the load, in this case a DC machine. This is however not very easy and convenient to imply a specific quantified misalignment in a reproducible way with an order of magnitude in μm . Although only combined

misalignment can be imposed, the AMB can displace the radial position of the rotor in relation to the stator at DE side very accurately, presented in Figure 4.4 (see Chapter 6). In order to obtain an accurate, quantified combined misalignment, the NDE bearing of the IM and the bearings of the load machine must be located on a perfect straight line. Unfortunately, as there is only one degree of freedom in the system (the AMB), not all combined misalignments can be reproduced.

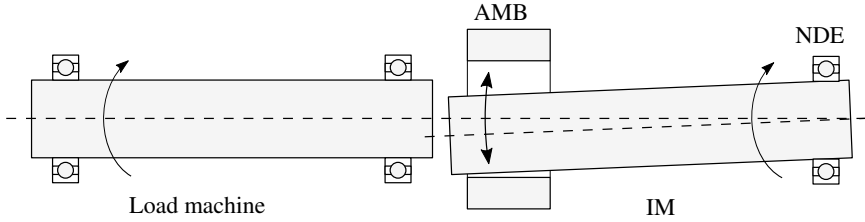


Figure 4.4: Implying combined misalignment with the AMB

Misalignment, in terms of rotor movement, is in essence a specific static eccentricity (this will be confirmed in Chapter 6). The rotor is, due to the coupled machine, radially loaded in one or another direction. Therefore, the AMB set-points dx and dy where the AMB is axially located can be written as a constant function in time for a specified direction:

$$dx = A_{\text{mis,hor}} \quad \text{and} \quad dy = A_{\text{mis,ver}} \quad (4.1)$$

with:

dx	set-point AMB horizontal;
dy	set-point AMB vertical;
$A_{\text{mis,hor}}$	eccentricity in horizontal direction;
$A_{\text{mis,ver}}$	eccentricity in vertical direction;

and:

$$A_{\text{mis}} = \sqrt{A_{\text{mis,hor}}^2 + A_{\text{mis,ver}}^2} \quad \text{total static eccentricity.} \quad (4.2)$$

Misalignment is usually not defined by the term A_{mis} , but by the terms *offset* and *gap difference*, graphically presented in Figure 4.5 [1, 86] (or respectively *rim* and *face*). *Face* and *rim* were commonly used before misalignment was measured with laser technology, being the read-off values of the dials in the alternative measuring methods [1]. Following Figure 4.5, the relation between the magnitude of misalignment, A_{mis} and the *offset*, c_{offset} , can be expressed as follows:

$$A_{\text{mis}} = \frac{x_2}{x_1} c_{\text{offset}} \quad (4.3)$$

with:

x_1	distance between NDE bearing and shaft end at DE;
x_2	distance between NDE bearing and DE bearing.

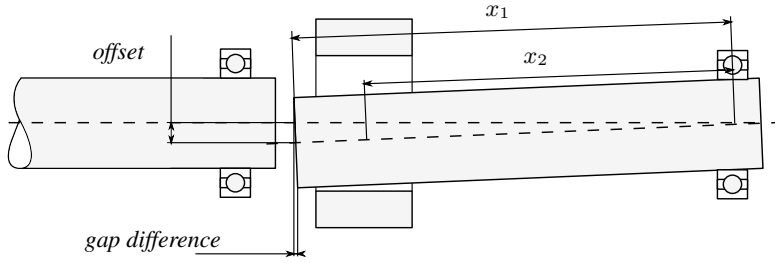


Figure 4.5: Misalignment defined by offset and gap difference

Due to the single degree of freedom in the test-rig using the AMB (Figure 4.5), the *gap difference*, c_{gapdiff} , can be expressed as a function of c_{offset} and the shaft diameter d_r :

$$c_{\text{gapdiff}} = d_r \cdot \sin \left[\arctan \left(\frac{c_{\text{offset}}}{x_1} \right) \right] \quad (4.4)$$

$$= \frac{d_r}{\sqrt{1 + \frac{x_1^2}{c_{\text{offset}}^2}}} \quad (4.5)$$

To summarize, misalignment A_{mis} can be expressed as a function of *offset*, c_{offset} or *gap difference*, c_{gapdiff} by the following equations:

$$A_{\text{mis}} = \begin{cases} \frac{x_2}{x_1} c_{\text{offset}} \\ \frac{x_2}{\sqrt{1 - \frac{d_r^2}{c_{\text{gapdiff}}^2}}} \end{cases} \quad (4.6)$$

With the use of previous equations, the severity (or magnitude) of misalignment and its reflection in the stator current can easily be investigated. The variables c_{offset} or c_{gapdiff} immediately result in specific static deviation A_{mis} . This deviation can be imposed by both a horizontal and/or vertical rotor displacement, respectively $A_{\text{mis,hor}}$ and $A_{\text{mis,ver}}$, defined in (4.2). These values of $A_{\text{mis,hor}}$ and $A_{\text{mis,ver}}$ directly result in the set-points dx and dy for the AMB, described in (4.1). When static eccentricity is applied into the IM, a reflection of that deviation is present in the stator current as it is defined by the formulas out of Table 3.5. As will be shown through experiments in Chapter 6, the relations between the severity of misalignment and the reflections for static eccentricity in the current spectra are clearly quantified.

4.2.2 Mechanical unbalance

Due to geometric and constructional imperfections, any operating IM is always severing residual mass-unbalance. Figure 4.6 presents the definition of an mass-unbalance. Aside the geometric position of the rotor, once the gravitational center-point of the rotor deviates from the rotational center, mass-unbalance can be defined. The quantification of the unbalance is done by defining a certain equivalent

mass-unbalance, m_{unb} , and a gravitational radius of that mass, r_{unb} . By coupling direct loads onto the shaft of the machine (e.g. pulleys, gears, sprockets), the unbalance is insuperably increased as small eccentricity is unavoidable [1]. Unbalance is fairly easy to identify by vibration analysis, because the eccentric mass generates an alternating force on the bearings and so on the stator housing (proportional with the measured acceleration). By observing a phase shift on 90° between the horizontal radial and vertical radial direction, mass-unbalance can be differentiated by any other overlapping component. Furthermore, the distinction can be made by changing the rotational speed (if possible), as a change of rotational speed affects the fault component following a quadratic relation. In order to detect the mass-unbalance in the stator current, an air gap variation must be imposed between the stator and the rotor. That variation is generally induced by the unbalance force reacting onto the bearings, as they (re)act as a simplified spring/damper system. These specific stiffness and damping properties of the bearing can be provided by the bearing supplier (or in the data sheet). The result of the propagation of the unbalanced force on the bearings is in fact a classic example of dynamic eccentricity (see Figure 4.1, right). Therefore, in this approach, mass-unbalance will be emulated by applying a dynamic eccentricity onto the machine.

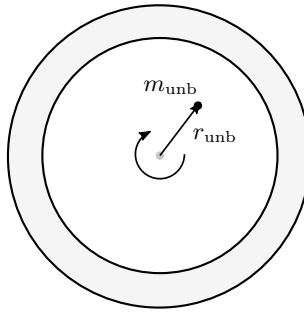


Figure 4.6: The quantification of mass-unbalance in a rotational system

As the unbalance induces a dynamic eccentricity, defined as a circular motion of the rotor center with respect to the rotational center, the specific rotor movements dx and dy are obtained by following time based trigonometric formulas (projection of the circular shape on two orthogonal axes):

$$dx = A_{\text{unb}} \cdot \sin(2\pi \cdot f_r \cdot t) \quad (4.7)$$

$$dy = A_{\text{unb}} \cdot \sin\left(2\pi \cdot f_r \cdot t + \frac{\pi}{2}\right) \quad (4.8)$$

with:

A_{unb}	magnitude of dynamic eccentricity;
t	time.

Now, the only unknown parameter in obtaining the rotor movements for every mass-unbalance is the magnitude of the dynamic eccentricity, A_{unb} . As the dy-

dynamic eccentricity is induced due to the centrifugal force originated by the mass-unbalance, it can be calculated as follows:

$$A_{\text{unb}} = \frac{F_{\text{unb}}}{k_r} = \frac{4\pi^2 \cdot m_{\text{unb}} \cdot r_{\text{unb}} \cdot f_r^2}{k_r} \quad (4.9)$$

with:

F_{unb}	centrifugal/unbalance force;
k_r	radial DE bearing stiffness.

Similar to static eccentricity within misalignment, a dynamic eccentricity due to mass-unbalance creates a unique signature in the current. Comprehensibly, as a clear air gap variation is imposed between the rotor and stator. When a mass-unbalance is applied, the fault frequency, f_{eccd} , is detectable in the stator current spectrum (see Table 3.5) [27, 61, 63, 64].

Note: In practice, due to many imperfections, rotating unbalance is (similar to misalignment) unavoidable. Because of this fact, the International Standard Organization created the *ISO 21940-11:2016* in which tolerable limits are defined for mass-unbalance in all kinds of applications. Conclusively, both misalignment and mass-unbalance are unavoidable. This means that the combination of static and dynamic eccentricity is ever-present in every electric rotating machine. This combination of these eccentricities is, as mentioned in §4.2, called *mixed eccentricity*. The signature of mixed eccentricity in the stator current spectrum, f_{eccm} , is defined as:

$$f_{\text{eccm}} = f_1 \pm k \cdot f_r \quad (4.10)$$

As already been discussed in Chapter 3, these components are used in the automated speed estimation based on stator current measurements. Of course, these components are as well used in the detection of misalignment and mass-unbalance. The differentiation between these phenomena is done by evaluating both fault frequency components of static and dynamic eccentricity as indicated in Table 3.5) [27, 61, 63, 64].

4.3 Bearing faults

The origin of bearing problems in the raceway can be variable, from mechanical to electrical issues, from factory imperfections to dimensioning and/or application mismatches [1, 39, 49]. The damage on the raceway is generally categorized following the visual appearance e.g. spalling, overheating, Brinell marks, excessive wear, corrosion, mechanical or electrical pitting. Besides, it is not excluded that the deterioration of the bearing fault can vary as a function of time. Conclusively, raceway problems are impossible to define in one single dimension/occurrence. Nevertheless, most bearing faults in their initial state can be related to material impurities or cracks which are present beneath the surface of the raceway. When, under operation, an excessive radial load is imposed on the race, the internal stress around the crack can increase excessively. This evolves in the propagation of the crack towards the raceway. Once the crack is exposed on the raceway as a surface impurity, it is commonly addressed as single point pitting [22–24, 38, 39, 43, 44, 49, 72, 74, 75]. That single point bearing pitting can evolve into more pitting, general roughness, spalling, other wear. . . However, in order to cover most bearing problems and especially immature bearing problems, this dissertation discusses the emulation of single point bearing pitting only. Thus, crucial information is needed about rotor movements for all kinds of single point bearing faults gathering severity conditions, rotor speed, fault location, bearing parameters. . . Once these movements are obtained and quantified, the emulation will be very similar to the real situation, because the implemented AMB excites the rotor on exactly the same axial location as the original mechanical bearing.

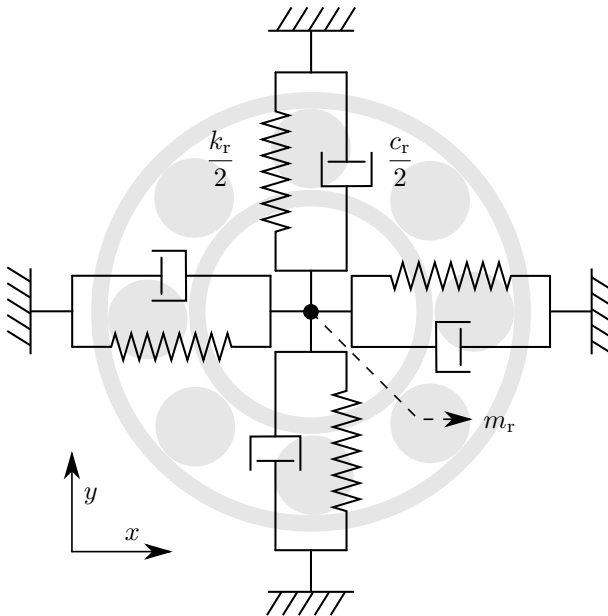


Figure 4.7: Stator/rotor relation represented by two 2DOF model with mass m_r , stiffness k_r and damping c_r

The rotor/stator system can be approximated by a simplified Two Degrees Of Freedom (2DOF) model with both a horizontal and vertical freedom, graphically presented in Figure 4.7 for the DE bearing of an IM. As this dissertation is more focused on the transmissible path from the mechanical rotor movement towards the electrical fault components in the stator current, this simplified model is sufficient to conduct this research. Nevertheless, it is possible to upgrade the model in order to obtain a more accurate representation of the rotor movements. However, the 2DOF system is fully characterized by a mass m_r , a stiffness k_r and a damping c_r following the force equation:

$$\begin{cases} h_y(t) = m_r \cdot \ddot{y}(t) + c_r \cdot \dot{y}(t) + k_r \cdot y(t) \\ h_x(t) = m_r \cdot \ddot{x}(t) + c_r \cdot \dot{x}(t) + k_r \cdot x(t) \end{cases} \quad (4.11)$$

$y(t)$ and $x(t)$ represent respectively the instantaneous vertical and horizontal displacement of the rotor with respect to the stator at time t . $h_y(t)$ and $h_x(t)$ are representing the forces between the rotor and the stator. $\ddot{y}(t)$, $\ddot{x}(t)$ and $\dot{y}(t)$, $\dot{x}(t)$ are respectively the instantaneous acceleration and velocity of the rotor with respect to the stator in the vertical and horizontal direction. The mass/spring/damper system can now be excited by using fault related force impulse functions, representing the rotor being excited by a single point bearing fault. The resulting system responses will then characterize the rotor movement under faulty conditions, which can subsequently serve as set-points for the AMB.

4.3.1 Bearing outer race fault

To characterize the single point outer race bearing fault, a pit is depicted in Figure 4.8. The pit has a certain length l_{pit} , depth d_{pit} and angle γ_{pit} . The angle α_{pit} is the angular position of the pit on the bearing outer race with respect to the vertical centerline through the bearing center point.

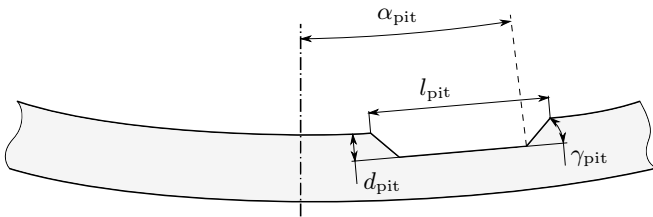


Figure 4.8: A quantified single point bearing pit

During rotation, the occurrence of the pit in the outer race causes a periodic impact on the rotor position. The periodicity is related to the speed in which the bearing balls are passing the pit. Due to the variable angular position of the pit throughout the outer race, α_{pit} , the 2DOF system gets excited by the outer race pit in the two directions: x and y . Correspondingly, the fault related force is subdivided in a vertical and horizontal force component, respectively $h_{y,o}(t)$ and $h_{x,o}(t)$. The vertical force function acting on the 2DOF system is shaped and parameterized in Figure 4.9. In the following derivation, subscript y,o and x,o are

used to refer to the vertical and the horizontal direction in case of single point outer race bearing faults.

The equivalent rotor mass, m_r , is constantly subjected to the gravitational force, resulting in the following expression of the magnitudes $I_{n,y,o}$ and $I_{n,x,o}$ (graphically presented for the vertical direction in Figure 4.9):

$$\begin{cases} I_{n,y,o} = -m_r \cdot g \\ I_{n,x,o} = 0 \end{cases} \quad (4.12)$$

with g the gravitational acceleration. Whenever a bearing ball passes the pit, a radial clearance d_{pit} is created for a certain time $t_{n,o}$, expressed as:

$$t_{n,o} = \frac{l_{\text{pit}}}{v_{b,o}} \quad \text{with: } v_{b,o} = \pi \cdot pd \cdot f_{\text{FTF}} \quad (4.13)$$

$v_{b,o}$ states the speed of the bearing ball passing the outer race pit. f_{FTF} represents the Fundamental Train Frequency (FTF) defined as, [13]:

$$f_{\text{FTF}} = \frac{f_r}{2} \left(1 - \frac{bd}{pd} \cos \beta \right) \quad (4.14)$$

with: f_r , the rotational speed; pd , the pitch diameter; bd , the bearing ball diameter and β , the bearing contact angle (as defined in Figure 2.10).

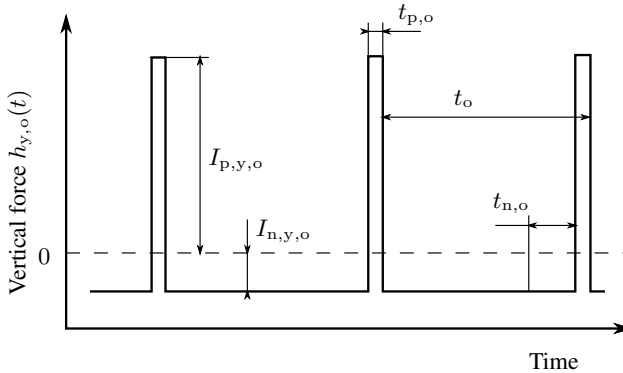


Figure 4.9: Parameterized outer race impulse function for the vertical direction

Because the outer race pit introduces a clearance d_{pit} whenever a bearing ball passes that pit, the rotor is able to displace with respect to the stator for a defined time $t_{n,o}$. As the deep groove ball bearings scoped within this thesis commonly have a positive radial clearance ($30\mu\text{m}$ for the SKF 6218 - C3 bearing mounted in this test-rig), the outer race is technically only supported by one or two bearing balls, because the outer circumference of the bearing balls is smaller than the outer raceway circumference. Additionally, when the traveling bearing ball is located at the very bottom of the bearing (in the top of the loaded zone), the rotor is supported by that bearing ball only. If the bearing ball subsequently falls into a bearing pit, the rotor is not supported by any other bearing balls. This vertical clearance

during that moment of free fall before it touches another adjacent bearing ball was determined to be $6.25\mu\text{m}$ for the bearing listed in Table 4.1 (when $\alpha_{\text{pit}} = 0$). The actual rotor displacement depends on the gravitational force imposing on the rotor. Consequently, the spatial location of the outer race pit, α_{pit} , is of interest. In following equations, the clearance d_{pit} only acts as a boundary value, i.e. a physical limit of the rotor displacements $d_{y,o}$ and $d_{x,o}$. It must be noted that the equations are only valid for $\alpha_{\text{pit}} \in [-\frac{\pi}{2}; \frac{\pi}{2}]$, as it is assumed that the largest radial load is located at $\alpha_{\text{pit}} = 0$. Furthermore, it is highly unlikely that any outer race pitting will occur at a non-loaded area.

$$\begin{cases} d_{y,o} = \frac{g}{2} t_{n,o}^2 \cdot \cos^2(\alpha_{\text{pit}}) & \text{with: } d_{y,o} \leq d_{\text{pit}} \\ d_{x,o} = \frac{g}{4} t_{n,o}^2 \cdot \sin(2 \cdot \alpha_{\text{pit}}) & \text{with: } d_{x,o} \leq d_{\text{pit}} \end{cases} \quad (4.15)$$

After the time $t_{n,o}$, the displaced bearing ball is pushed back on the original track which follows the circular shape of the outer race. The amount of radial rotor displacement ($d_{y,o}$ and $d_{x,o}$), the ramp angle γ_{pit} and the speed $v_{b,o}$ defines the time $t_{p,o}$ in which the rotor is pushed back in the initial, central position, expressed as:

$$t_{p,o} = \frac{\sqrt{d_{y,o}^2 + d_{x,o}^2}}{\tan(\gamma_{\text{pit}}) \cdot v_{b,o}} \quad (4.16)$$

During the time $t_{p,o}$, a positive force $I_{p,y,o}$ and $I_{p,x,o}$ is acting on the rotor, largely determining the behavior of the system response when a bearing fault occurs:

$$\begin{cases} I_{p,y,o} = m_r \left(\frac{d_{y,o}}{t_{p,o}^2} - g \right) \\ I_{p,x,o} = m_r \frac{d_{x,o}}{t_{p,o}^2} \end{cases} \quad (4.17)$$

Those forces $I_{p,y,o}$ and $I_{p,x,o}$ are acting on the rotor with a specific period, depending on the FTF and the number of bearing balls, n_b :

$$t_o = \frac{1}{n_b \cdot f_{\text{FTF}}} \quad (4.18)$$

The force-functions caused by the single point outer race bearing fault $h_{y,o}(t)$ and $h_{x,o}(t)$ for both vertical and horizontal direction are conclusively established based on previous formulas and Figure 4.9 (with $k \in \mathbb{N}_0$):

$$h_{y,o}(t) = \begin{cases} m_r \left(\frac{d_{y,o}}{t_{p,o}^2} - g \right) & \text{for } t \in [0 : t_{p,o}] + t_o \cdot k \\ -m_r \cdot g & \text{for } t \in [t_{p,o} : t_o] + t_o \cdot k \end{cases} \quad (4.19)$$

$$h_{x,o}(t) = \begin{cases} m_r \frac{d_{x,o}}{t_{p,o}^2} & \text{for } t \in [0 : t_{p,o}] + t_o \cdot k \\ 0 & \text{for } t \in [t_{p,o} : t_o] + t_o \cdot k \end{cases} \quad (4.20)$$

Parameter	Value	Unit
l_{pit}	2	[mm]
d_{pit}	100	[μm]
γ_{pit}	$\frac{\pi}{6}$	[rad]
α_{pit}	0	[rad]
pd	17.5	[mm]
bd	7.4	[mm]
β	0	[rad]
n_b	8	[—]
f_r	24.8	[Hz]
m_r	21.9	[kg]
c_r	14.53	[kNs/m] :
k_r	$2.85 \cdot 10^5$	[kN/mm]
g	9.81	[m/s ²]

Table 4.1: Calculation parameters

Using the mathematical software tool described in [9], the 2DOF system is excited by the force functions obtained for a specific case of which the parameters are listed in Table 4.1. The corresponding vertical response function, $y_o(t)$, is presented in Figure 4.10. This is the exact vertical rotor displacement when that single pit outer race bearing fault propagates in this specific IM. Consequently, using this technique, the rotor movement when a single point outer race bearing fault occurs can be obtained for a wide variety of conditions. By adapting the rotational speed, pit dimensions, bearing parameters, bearing characteristics..., subsequently recalculating the force functions and exciting the 2DOF system, exact movements of the rotor with respect to the stator can be obtained for an infinite number of situations, even varying severity. As a consequence, as these high-dynamic rotor movements are now characterized, they can serve as bench-mark in dimensioning the dynamic requirements of the AMB, discussed Chapter 5.

4.3.2 Bearing inner race fault

The main difference between inner and outer race problems is that regarding inner race bearing faults, the problem is rotating with respect to the stator at speed f_r . The time based force functions applied on the rotor, caused by the inner race bearing pit, are established equivalently to §4.3.1. Although Figure 4.8 is a representation of a single point outer race bearing pit, the same pit dimensions are applied in the following derivation with the exception of α_{pit} as the fault is now rotating. Counter-intuitively, the time $t_{n,i}$ of the unsupported rotor when a bearing ball passes the inner race pit is exactly equal to $t_{n,o}$. This is because the speed of

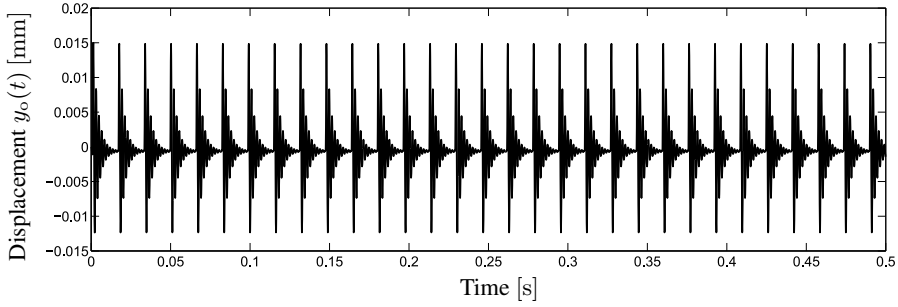


Figure 4.10: Vertical rotor displacement for a specific single point bearing outer race fault, $y_o(t)$ (conditions in Table 4.1)

the bearing ball passing the inner race pit, $v_{b,i}$, is the same as $v_{b,o}$, (4.13):

$$v_{b,i} = \pi (pd - bd \cdot \cos \beta) f_r - \pi \cdot pd \cdot f_{\text{FTF}} = v_{b,o} \quad (4.21)$$

resulting in:

$$t_{n,i} = \frac{l_{\text{pit}}}{v_{b,i}} = \frac{l_{\text{pit}}}{v_{b,o}} = t_{n,o} \quad (4.22)$$

Due to the varying position of the pit, the resulting rotor displacement (defined as $d_{y,i}$ and $d_{x,i}$) created during the time $t_{n,i}$, is now a function of time:

$$\begin{cases} d_{y,i} = \frac{g}{2} t_{n,i}^2 \cdot \cos(\omega_r \cdot t + \phi) \cdot f_{\text{int}}(t) \\ d_{x,i} = \frac{g}{2} t_{n,i}^2 \cdot \sin(\omega_r \cdot t + \phi) \cdot f_{\text{int}}(t) \end{cases} \quad (4.23)$$

with:

$$\omega_r = 2\pi \cdot f_r$$

$$d_{y,i} \leq d_{\text{pit}}$$

$$d_{x,i} \leq d_{\text{pit}}$$

$$h_{\text{int}}(t) = \begin{cases} \cos(\omega_r \cdot t) & \text{for } t \in \left[-\frac{\pi}{2} : \frac{\pi}{2}\right] + 2\pi \cdot k \\ 0 & \text{for } t \in \left[\frac{\pi}{2} : \frac{3\pi}{2}\right] + 2\pi \cdot k \end{cases}$$

$$\text{and } k \in \mathbb{N}_0$$

It must be noted that in (4.23), the inner race pit is located at the lowest point of the bearing at time $t = 0$ s. The angle ϕ is the spatial angle between the single point inner race bearing pit and the first passing bearing ball (in the direction of movement). The function $h_{\text{int}}(t)$ is defined as the interaction curve between the rotor and the rotating bearing pit. When the pit is located at the top half of the bearing, no rotor displacement is induced by gravity. When the pit is located at the bottom half of the bearing, the gravitational force interacts following a cosine function. Similar to outer race bearing fault propagation, the time in which the

displaced bearing ball is restored in the original circular track and the rotor is pushed back to its initial position is written as:

$$t_{p,i} = \frac{\sqrt{d_{y,i}^2 + d_{x,i}^2}}{\tan(\gamma_{\text{pit}}) \cdot v_{b,i}} \quad (4.24)$$

The inner race force-functions are:

$$h_{y,i}(t) = \begin{cases} m_r \left(\frac{d_{y,i}}{t_{p,i}^2} - g \right) & \text{for } t \in [0 : t_{p,i}] + t_i \cdot k \\ -m_r \cdot g & \text{for } t \in [t_{p,i} : t_i] + t_i \cdot k \end{cases} \quad (4.25)$$

$$h_{x,i}(t) = \begin{cases} m_r \frac{d_{x,i}}{t_{p,y,i}^2} & \text{for } t \in [0 : t_{p,x,i}] + t_i \cdot k \\ 0 & \text{for } t \in [t_{p,x,i} : t_i] + t_i \cdot k \end{cases} \quad (4.26)$$

with:

$$t_i = \frac{1}{n_b (f_r - f_{\text{FTF}})} \quad \text{and } k \in \mathbb{N}_0 \quad (4.27)$$

As an example, the inner race bearing fault force functions $h_{y,i}(t)$ and $h_{x,i}(t)$ are obtained and presented in Figure 4.11a and Figure 4.11c for the vertical and horizontal direction concerning a single point bearing pit described in Table 4.1 (and the angle $\phi = \pi/5$). The corresponding system response functions $y_i(t)$ and $x_i(t)$ are presented in respectively Figure 4.11b and 4.11d.

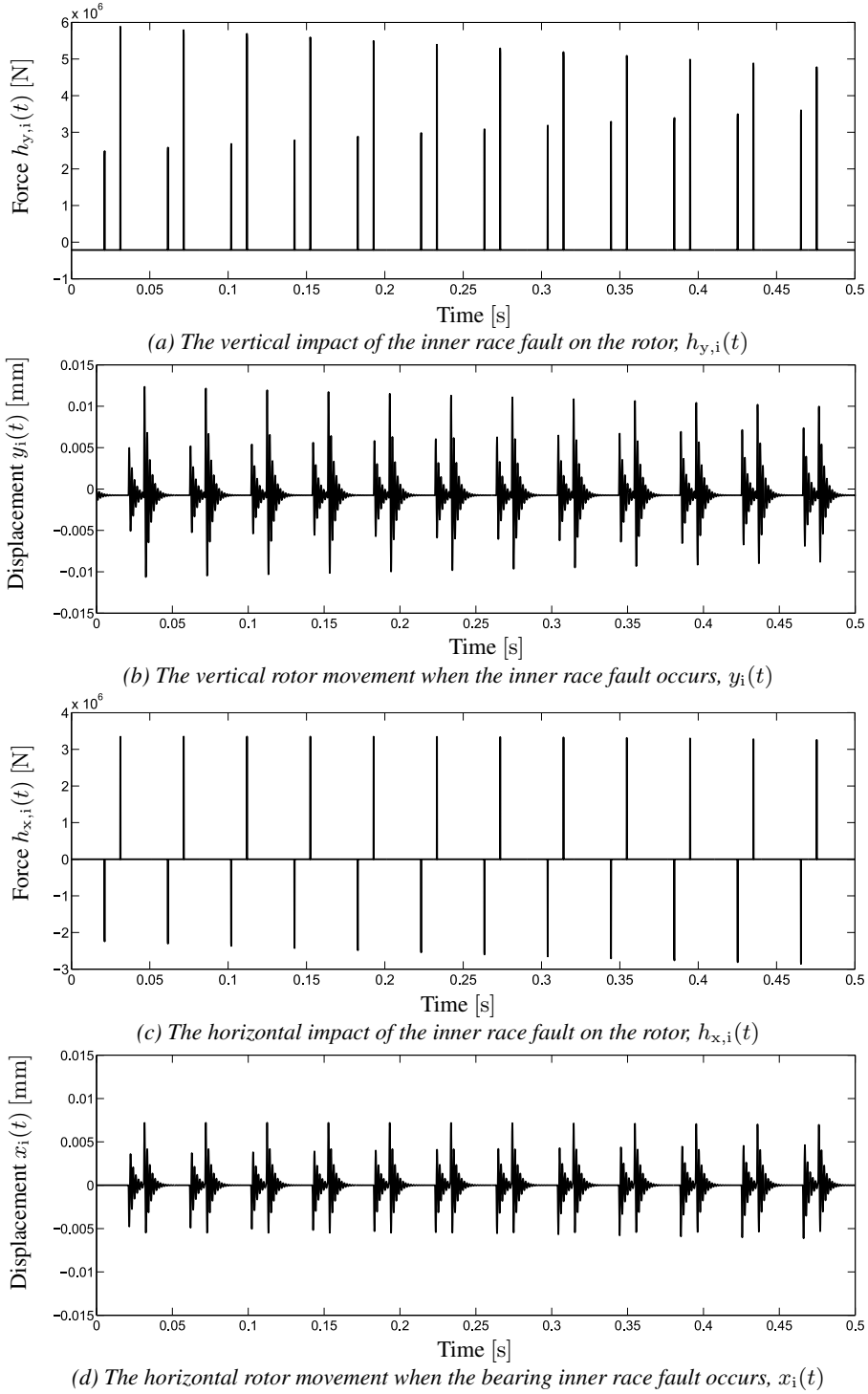


Figure 4.11: The vertical/horizontal impulse functions and rotor movements for the inner race bearing fault specified in Table 4.1

Note: The angle $\phi \in [0; \frac{2\pi}{n_b}]$ can be chosen randomly, but the importance can not be neglected. The functions obtained to characterize the rotor movements when an inner race bearing faults is elaborating are not periodic. This due to the irrational factor between the rotating frequency f_r and the pulse train frequency $\frac{1}{t_i}$. If a function, containing two different frequencies is periodic, the composing function has a period r following the equation:

$$r = a \cdot t_i = b \cdot \frac{1}{f_r} \quad (4.28)$$

in which a and b must be positive integers. If the previous expression is rewritten, an interesting statement can be made:

$$r = \frac{a}{n_b(f_r - f_{\text{FTF}})} = \frac{b}{f_r} \quad (4.29)$$

$$\frac{a}{b} = n_b \left(1 + \frac{f_{\text{FTF}}}{f_r} \right) \quad (4.30)$$

$$= \frac{n_b}{2} \left(1 + \frac{bd}{pd} \cdot \cos \beta \right) \quad (4.31)$$

When a and b are positive integers, $\frac{a}{b}$ must be a rational number. However, the right side of equation 4.31 can never be a rational number. This because the values pd and bd are both physical dimensions and thereby irrational numbers, inevitably implying that the ratio bd/pd is not rational. Consequently, the signature of an inner race bearing fault is not periodic and the fundamental frequency of that function is defined to be 0Hz. Nevertheless, it does not imply that the separated frequencies f_r and f_{in} (Table 3.5) are not detectable in the stator current spectra. To clearly identify an inner race bearing fault, the fault component f_{in} are propagated to the stator spectrum with sidebands of $\pm f_r$ [1, 5]. These sidebands are in fact present because of the rotational character of the single point inner race bearing fault.

4.3.3 Bearing cage fault

The detection of the bearing cage fault frequencies is generally seen as the final stage of a bearing life-time. This is because, in vibration analysis, the faulty cage frequency is only noticed when severe bearing wear occurs. However, this statement holds only for vibration analysis, because the rather low cage fault frequency can only be noticed by accelerometers when significant forces are propagating. Regarding current analysis, the cage fault frequency is detected at a very early stage of any bearing fault. The current faulty cage components are in fact linear to the air gap deviation and so depend on the rotor displacement (not on the rotor acceleration). Furthermore, the detection of the bearing cage fault frequency can indicate either a bearing outer race, inner race or cage problem and can be used for fault determination/identification. However, it should be noted that as soon as the cage of any bearing is failing, the machine remaining operational time will be negligible.

Concerning the definition of cage related issues, it is commonly addressed as an unequal angular distribution of the bearing balls throughout the bearing race

(see Chapter 2). This can be caused by any defect in the cage e.g. looseness, cracks or bursts. The defect in the cage implies a non-concentric deviation between the stator and the rotor with a circular speed of f_{FTF} , defined as the fundamental train frequency. This deviation of the rotational center of the rotor with respect to the stator geometrical center is commonly defined as dynamic eccentricity, presented in Figure 4.12. The exact rotor movement in the respectively vertical and horizontal direction is described by following functions:

$$\begin{cases} y(t) = A_{\text{cage}} \cdot \sin(2\pi \cdot f_{\text{FTF}} \cdot t) \\ x(t) = A_{\text{cage}} \cdot \sin\left(2\pi \cdot f_{\text{FTF}} \cdot t + \frac{\pi}{2}\right) \end{cases} \quad (4.32)$$

The magnitude of the dynamic eccentricity can be linked with the fault severity. For a machine in good condition, highly depending on the bearing type and load topology, a magnitude of $\approx 20\mu\text{m}$ is acceptable. As the clearance in the bearing cage is required for a proper functioning of the bearing, the bearing cage fault frequency is by using stator current analysis even detectable in a machine without any bearing problems. For this type of fault, it is more interesting to log the differential increase in magnitude instead of the absolute interpretation of the detected fault components. This because, in contrast to bearing cage faults, the other characterized mechanical faults do have a specific relation with their fault severity (e.g. pit length, gap difference, mass-unbalance). However, differential logging is for every detected fault interesting as it indicates the evolving character of the fault.

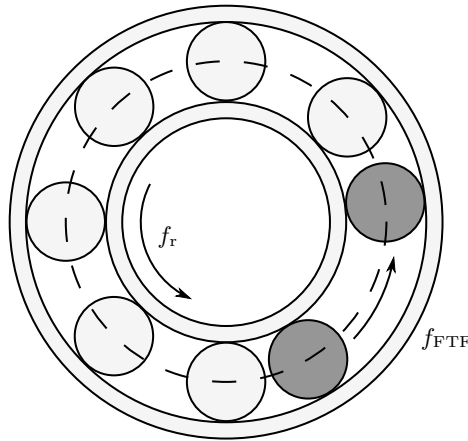
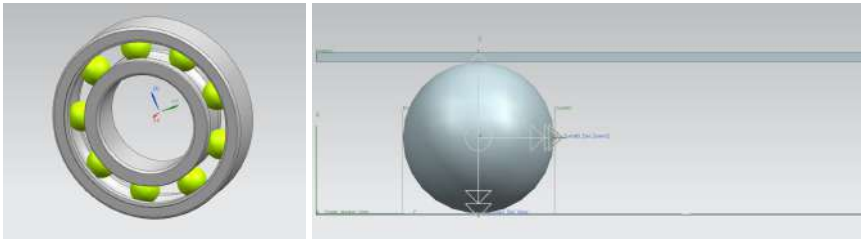


Figure 4.12: Rotor dynamic eccentricity when bearing cage fault occurs

4.4 Validation of the bearing fault model

In order to obtain the high quality of relevance and reproducibility during fault emulation, it is important to validate the analytic model which is used to obtained mechanical fault related rotor movements. Two ways are applied in order to do so: via Multi-body dynamics simulation and via a practical test case. By the simulation, the interaction of the rotor and stator when a bearing fault occurs could be obtained by simplifying the interaction of a single bearing ball passing an outer race pit. By the industrial case study, the same as presented in §3.4.3, the specific rotor movement while the DE bearing is severing an outer race pit is calculated out of the vibration measurements (acceleration of the stator housing). Those estimated movements of both methods are subsequently compared with the analytical model.

4.4.1 Multi-body dynamics simulation



(a) 3D-drawing of the used SKF®-bearing 6302-2Z

(b) Simplified Multi-body dynamics model used to estimate the interacting forces between rotor and stator

Figure 4.13: The implementation of the bearing in the Multi-body dynamics simulation software Siemens NX® motion

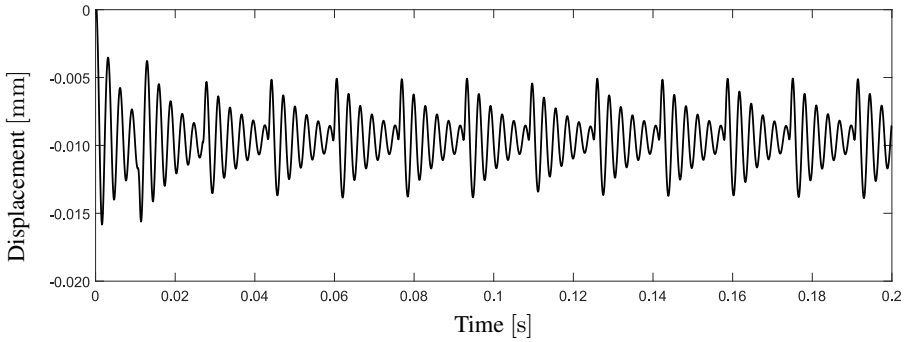
Using the software package Siemens NX® motion, simulations can be performed on all kinds of mechanical systems. The 3D CAD drawings of most implemented bearings can be gathered via the bearing supplier for dimensioning purposes. In following analysis, the bearing 6302 - 2Z of the company SKF® is used of which the 3D drawing is presented in Figure 4.13a. For the model to be representative, the mass, stiffness and damping properties of the rotor is included into the model's inner race. The outer race is considered to be fixed. That can be assumed, because in most cases the stiffness and damping parameters between the outer race/the stator and the inner race/the rotor are significantly higher than the same parameters between the outer race and the inner race (or stator/rotor relation). Consequently, the weak part of the mechanical rotor/stator system is considered to be the bearing itself and not the bearing housing. The outer race pit is equally added to the bearing outer race as presented in Figure 4.8. Because the unmanageable complexity of the rotational constraints of every bearing element, the simulation model is simplified as presented in Figure 4.13b. The bottom plate in the model is representing the fixed outer race. The upper plate is considered to act as the inner race and rotor. In order the model to be valid, the upper platform

has all the vertical mass properties of the inner race and the rotor at DE side. Note that these properties are not specified by this case, as it only considers the bearing and not a total machine, but chosen as listed in Table 4.2. Between the two plates, the bearing ball is found to roll over the outer race pit.

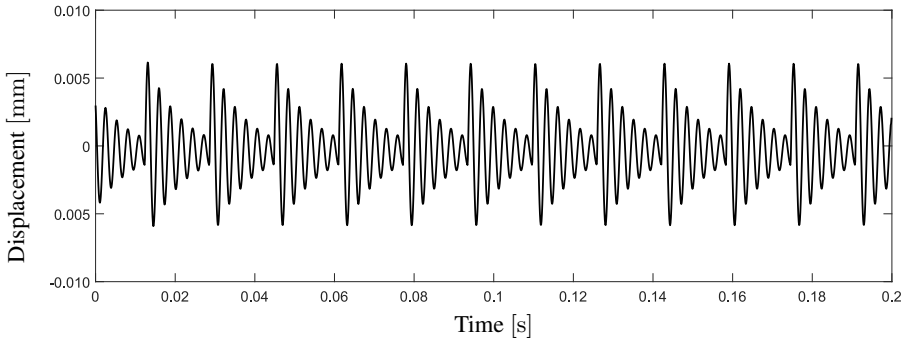
Parameter	Value	Unit
l_{pit}	1	[mm]
d_{pit}	100	[μm]
γ_{pit}	$\frac{\pi}{6}$	[rad]
α_{pit}	0	[rad]
pd	28.5	[mm]
bd	9.2	[mm]
β	0	[rad]
n_b	9	[—]
f_r	24.852	[Hz]
m_r	18.24	[kg]
c_r	4.330	[kNs/m]
k_r	$0.925 \cdot 10^5$	[kN/mm]

Table 4.2: Bearing SKF® 6302 - 2Z parameters and pit dimensions

The vertical movement of the upper plate is presented in Figure 4.14a. The vertical movement of rotor, calculated by the analytical model obtained in §4.3.1 under the same speed, bearing dimensions, bearing properties and pit dimensions (Table 4.2) is presented in Figure 4.14b. As can be observed, the Multi-body dynamics simulation indicates a clear offset in displacement, $\approx 8\mu\text{m}$. That offset is imposed by gravity and is the suppression of the bearing ball and outer race by its own weight (material stiffness). Additionally, the results of the analytical model are slightly larger in magnitude than the simulation model. This can be assigned to many reasons, but one of them is surely the impact of the centrifugal force working on the bearing balls, which is not taken into account in the Multi-body dynamics simulation (due to the simplification). Additionally, a slight difference is noticeable between both system properties as the decay of the vibration is slightly larger for the analytical model than for the Multi-body dynamics simulation. This is because of a small difference in damping properties between the two methods. Nevertheless, it can be concluded that the simple, easy-to-use analytical model obtained in §4.3 perfectly satisfies the needs to calculate rotor movements as a function of numerous speeds, bearing dimensions, bearing properties and pit dimensions. In general, the results are observed as very similar.



(a) The vertical movement of the equivalent rotor in the Multi-body dynamics simulation of a single point outer race pit



(b) The vertical movement obtained by the analytical bearing model

Figure 4.14: The validation of the analytical faulty bearing rotor movement model by Multi-body dynamics simulation

4.4.2 Industrial test case

The case study of a 980kW IM severing from a single point inner race bearing pitting (see §3.4.3) is the perfect case where the proposed analytical model can be validated. However, it is of major importance to estimate the corresponding rotor movements out of the measured IM vibrations. These measured stator vibrations can be recalculated to rotor movements by using the simplified 2DOF model presented in §4.7. Although, significant errors are made by this approach, because vibrations caused by the machine frame and the stator are assumed to have the origin at the rotor as well. Nevertheless, as the exciting frequencies of the inner race fault have their origin on the rotor, the obtained movements related to the inner race bearing fault are assumed to be valid for those specific fault frequencies (no other machines where mounted on that frame). Therefore, as Figure 4.15 proposes, the rotor movements are calculated out of the stator movements.

Because the inner race faulty rotor movements were proven to be non-periodic, techniques such as time-averaging can not be applied to estimate the exact inner race related movements on the IM rotor. In order to translate the forcing fault frequency from the stator to the rotor, only the fundamental inner race fault frequency f_{in} is considered. This method is valid, as this forcing component is fully respon-

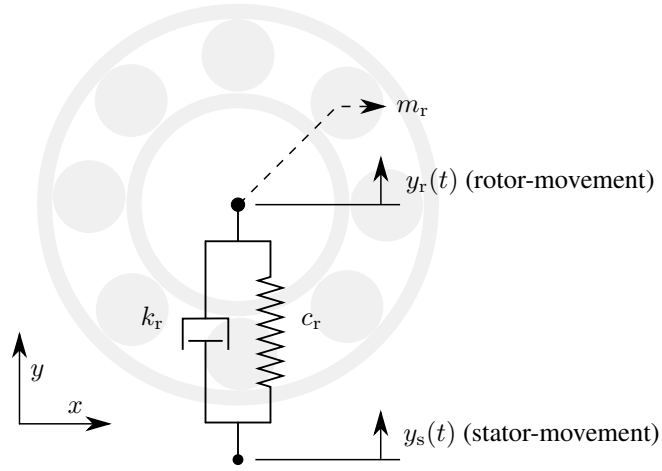


Figure 4.15: The rotor movement $y_r(t)$ is calculated out of the measured vibration on the stator frame $\ddot{y}_s(t)$ using this 2DOF model

sible for the detection in the vibration and current spectra. This component was measured to have a magnitude of $5.380g$ at 124.93Hz following Table 3.6 under the specified load conditions discussed in §3.4.3. To calculate the rotor displacement of that vibration, the *SKF® 6226 - C3* bearing properties are listed Table 4.3. The 2DOF model presented in Figure 4.15, can be mathematically described as:

$$m_r \cdot \ddot{y}_r(t) + c_r \cdot \dot{y}_r(t) + k_r \cdot y_r(t) = c_r \cdot \dot{y}_s(t) + k_r \cdot y_s(t) \quad (4.33)$$

with $\ddot{y}_r(t)$, $\dot{y}_r(t)$ and $y_r(t)$ being the respectively acceleration, velocity and displacement of the rotor and $\ddot{y}_s(t)$, $\dot{y}_s(t)$ and $y_s(t)$ for the stator. As only the inner race fault frequency of 124.93Hz is considered, the mathematical model can be simplified significantly due to the following notation of $\ddot{y}_s(t)$ and $\ddot{y}_r(t)$:

$$\begin{cases} \ddot{y}_s(t) = a_s \cdot \sin(2\pi \cdot f_i \cdot t) \\ \ddot{y}_r(t) = a_r \cdot \sin(2\pi \cdot f_i \cdot t) \end{cases} \quad (4.34)$$

and consequently:

$$\begin{cases} \dot{y}_s(t) = -\frac{a_s}{2\pi \cdot f_{in}} \cos(2\pi \cdot f_{in} \cdot t) \\ \dot{y}_r(t) = -\frac{a_r}{2\pi \cdot f_{in}} \cos(2\pi \cdot f_{in} \cdot t) \\ y_s(t) = -\frac{a_s}{2\pi^2 \cdot f_{in}^2} \sin(2\pi \cdot f_{in} \cdot t) \\ y_r(t) = -\frac{a_r}{2\pi^2 \cdot f_{in}^2} \sin(2\pi \cdot f_{in} \cdot t) \end{cases} \quad (4.35)$$

As $a_s = 5.380g$ and $f_i = 124.93\text{Hz}$ are known variables, the unknown variable a_r is calculated by (4.33) as $20.874g$. This corresponds to a displacement of

144.24 μm at 124.93Hz. In order to compare these results in displacement with the calculations of the analytical bearing model presented in §4.3, the magnitudes of the fundamental components of the single point inner race rotor movements are calculated as a function of the pit length l_{pit} (with $d_{\text{pit}} = 100\mu\text{m}$ fixed). Out of these analytical calculation, the same magnitude of 20.874g corresponds to a pit length of 12.672mm. Now, the model can only be stated as validated when this pit length is comparable with the pit length of the IM's faulty bearing. After replacing the DE bearing of the IM, the company sent the bearing of which the largest single point inner race pit was measured to be $\sim 15\text{mm}$ (next to several roughness damage further on the raceway). As this estimation of pit length can be stated as sufficiently accurate, the analytical bearing model is conclusively be assumed to be valid and will be used in all further calculations and experiments.

Parameter	Value	Unit
pd	180	[mm]
bd	31.75	[mm]
β	0	[rad]
n_b	9	[—]
f_r	24.868	[Hz]
I_r	28.0	[kg/m ²]
c_r	5	[kNs/m]
k_r	$3.24 \cdot 10^5$	[kN/mm]

Table 4.3: Bearing SKF® 6226 - C3 parameters

4.5 Conclusion

This chapter was intended to obtain an analytical model which is able to calculate rotor movements for several types of mechanical faults. Regarding misalignment and mass-unbalance, a quite straight-forward and simple, yet relevant way was proposed in order to establish the time based rotor eccentricities by both phenomena. It was briefly mentioned that misalignment corresponds to static eccentricity as unbalance corresponds with dynamic eccentricity. This statement will be confirmed by experiments in Chapter 6. However, analytical models are constructed which defines both rotor movements as a function of their corresponding fault severity. Regarding bearing problems, more specific single point bearing faults, it was a more complex matter. By constructing a 2DOF model and exciting it by fault related impulse functions, an analytic method was obtained which calculates the fault related rotor movements with high accuracy. Although the simplified 2DOF model can be improved significantly in order to obtain the rotor movements with higher accuracy, the results were successfully validated by both Multi-body dynamics simulation and an industrial test case. Now the rotor movements are analytically obtained for most common mechanical faults and their severity, the active magnetic bearing can be dimensioned based on these dynamic requirements. This is a significant contribution to the field of condition monitoring with the focus on mechanical fault propagation. As this type of analytical model does not exist in today's literature, it can be valuable to the development of several CM-system. Next chapter fully focuses on the dimensioning of the AMB, its construction and the control system. The rotor movement obtained in this chapter for a single point outer race bearing pitting will be used as a benchmark to determine the dynamic capabilities of the AMB. When the test-rig is finalized, experiments will be conducted in the following Chapter 6.

5

Fault emulating test-rig

5.1 Introduction

The majority of the potential mechanical faults which can occur in an IM induces specific radial movements of the rotor in relation to the stator (e.g. unbalance, misalignment, bearing faults). Consequently, emulating several types of mechanical faults in an electric machine can be done by manipulating the position of the rotor in reference to the stator with high accuracy. By replacing one of the mechanical bearings of the machine by a controllable Active Magnetic Bearing (AMB), fault related rotor movements can be imposed on the rotor. Stiffness and damping characteristics of the original mechanical bearing can be implemented in the control loop of the AMB. Therefore, the machine system characteristics can be held constant while the emulated mechanical faults are evolving, controlled via an accessible user interface. Specific faults and their reflection in the stator current are investigated thoroughly with a variety of controllable conditions regarding torque, speed, temperature, supplied voltage... This novel and unique way of emulating faulty conditions results in the achievement of high quality in relevance and in reproducibility. Due to the research conducted in previous chapter, the required rotor movements were obtained which define the dynamics of the AMB system. Thereby the AMB can be dimensioned and constructed.

Many research has already been conducted on AMBs, which significantly simplifies this research. Nevertheless, the AMBs designed and discussed in literature have total different objectives and purposes [87–90]. Mostly, the bearing is dimensioned in order to reduce the losses of the machines, more specific, the friction losses of the mechanical bearings. Therefore, AMBs are more interesting and applicable for high-speed machines ($> 20000rpm$ rotational speed, example in Figure 5.1). This will be at one hand an advantage in terms of dynamics, because most control strategies designed for AMBs are focused on high-dynamic

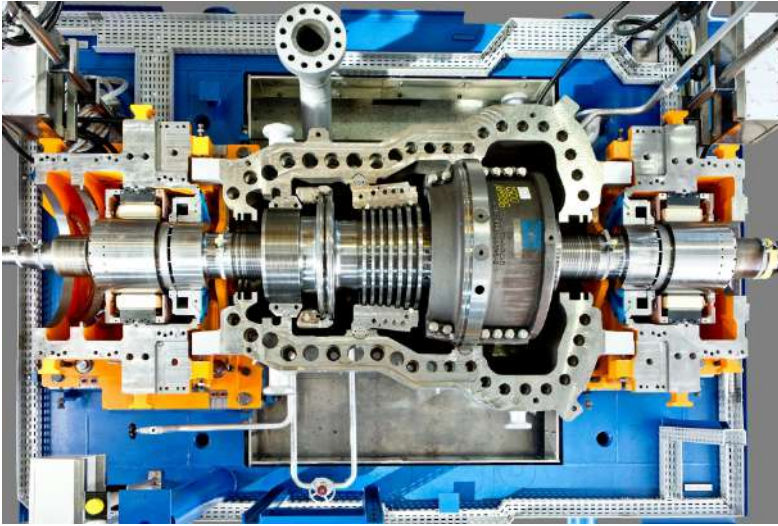


Figure 5.1: The SST-600 high-speed steam turbine of Siemens® equipped with AMBs

responses due to the high speed. As the IM is only rotating at $1500rpm$, it is considered as a rather slow, low dynamic system. On the other hand, as rotor movements are to be induced, the AMB air gap will have to be relatively large, which has a negative impact on the dynamics. As this research is about controlling the rotors position instead of optimizing the machines efficiency, the bearing will not be dimensioned with the focus on losses. First, the power range of the AMB will be determined in §5.2.1. This includes the range of force needed to counter all reacting forces between the rotor and the stator. Subsequently, the dynamics are analyzed in §5.3. In that section, the control loop will be designed on simulation basis in order to validate the capability in emulating the rotor movements obtained in previous section. This is to increase assurance that the bearing will do the job when it is fabricated. Finally, the AMB is constructed, implemented and tested on the 11kW IM (§5.4). The successful construction of the test-rig and its concept as it was presented in Chapter 1 revolutionizes the world of mechanical fault emulation. The test-rig obtained in this research, which enables reproducible and relevant fault emulation such as bearing faults varying in their severity, is a unique and significant contribution to the world of condition monitoring and fault diagnosis. The accessible control and manipulation of several environmental conditions will definitely enhance the development and valorization of MCSA as a full and reliable CM-system.

5.2 AMB dimensions

5.2.1 Steady state parameter estimation

An AMB is in general applied to reduce the losses in high-speed machinery by shifting the bearing friction losses to copper and iron losses [87–90]. As in this project the main purpose of the AMB is to deliberately manipulate the rotor position with respect to the stator, the AMB effectiveness is more important than the efficiency. Loss calculations are thereby excluded from this thesis. The AMB is dimensioned with the focus on compensating all interacting forces between the rotor and the stator during rotation and additionally creating fault related rotor movements.

The forces imposed on the DE bearing by the rotor and the stator are in essence the gravitational force of the rotor/coupling, the unavoidable mechanical rotor unbalance and the Unbalanced Magnetic Pull (UMP). Apart from those, the AMB must be able to provide an additional dynamic force on the rotor in order to create a displacement according to the obtained response functions out of Chapter 4. As a reference, the functions $y_o(t)$ and $x_o(t)$ presented in Figure 4.10 are used to estimate the required range in force. Since the rotor will be moving with respect to the stator, the AMB must be constructively dimensioned with a relatively large air gap between the AMB and the rotor shaft in order to maintain the freedom of the rotor moving around in the entire air gap of the IM (regular AMBs: 10 – 100 μ m, [87–90]). The air gap in the IM is 0.85mm which determined the air gap between the AMB and the rotor shaft to be 2mm. This due to the NDE bearing being radially fixed causing a leverage effect. Nevertheless, an additional mechanical safety will be mounted to avoid contact between the rotor and stator of the IM resulting in a radial freedom in the air gap of 0.6mm.

The physical topology used for the AMB is presented in Figure 5.2. Two coils around two adjacent poles form one winding (four windings in total). The current through one winding imposes a magnetic flux in two poles, following a closed path through the AMB and the rotor shaft. That closing flux through the air gap generates an attractive force between the rotor and the AMB stator [32]. Unfortunately, as the rotor has no magnetic polarity, a repulsive force can not be generated. In order to move and control the rotor in each direction, four windings are implemented perpendicularly so that forces can be imposed on the rotor in the upper, down, left and right direction. The attractive force between the AMB and the rotor shaft for one winding (two coils, two poles) is analytically expressed as [32, 88]:

$$u(t) = \mu_0 \left(\frac{N \cdot i(t)}{\frac{l_{stat}}{\mu_{rstat}} + \frac{l_{sh}}{\mu_{rsh}} + 2 \cdot z(t)} \right)^2 A_a \cdot \cos \alpha \quad (5.1)$$

with: $u(t)$, the resulting force; μ_0 , the permeability of vacuum; N , the number of turns in the winding; $i(t)$, the current through the winding; l_{stat} , the length of the flux path through the AMB; l_{sh} , the length of the flux path through the rotor shaft; μ_{rstat} , the relative permeability of the AMB laminated electrical steel; μ_{rsh} , the relative permeability of the rotor shaft; $z(t)$, the mean radial air gap between the

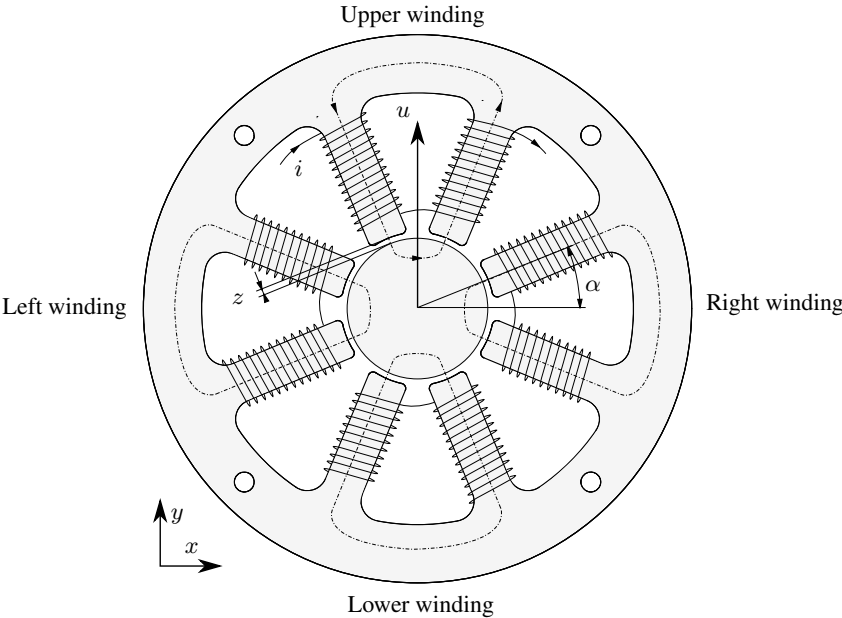


Figure 5.2: Magnetic bearing topology

two AMB poles and the rotor shaft; A_a , the cross section surface of one pole and α , the angle between the generated force and one pole.

Parameter	Value	Unit
μ_0	$4\pi \cdot 10^{-7}$	[H/m]
$\mu_{r_{stat}}$	4000	[—]
$\mu_{r_{sh}}$	1800	[—]
α	22.5	[°]
m_r	21.9	[kg]
g	9.81	[m/s ²]
l_{sh}	0.02	[m]
B_{max}	1.8	[T]

Table 5.1: Fixed AMB parameters

Some of the AMB parameters in (5.1) are fixed due to geometric and physical constraints such as material properties or construction space around the IM (Table 5.1). By varying the remaining variable parameters e.g. number of turns in the windings, cross pole surface, pole width..., the optimal AMB is constructively dimensioned with respect to the required operational range of the four generated forces. These variables are mainly determined by the available constructive space within the stator housing. Applying the variable parameters according to Table

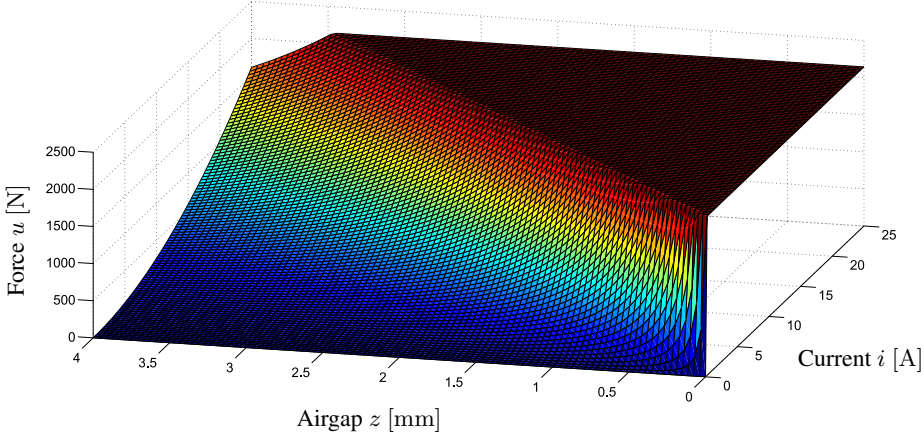


Figure 5.3: The steady state attractive force u generated by a winding as a function the current through that winding, i , and the air gap between the rotor and the poles of that winding z (applicable for each of the four windings)

5.2 in (5.1), the data of Figure 5.3 is established for one winding/force generator. This figure presents the time independent steady state force u as a function of the current i and the air gap z (applicable for each winding). The upper limit of the generated force, $\sim 2.2\text{kN}$, is where the flux density in the AMB electrical steel is maximum (the magnetic material saturates at $\sim 1.8\text{T}$). Since the UMP is typically around $\sim 500\text{N}$ for the 11kW IM under test, [85, 91], and the measured gravitational force at DE side is $\sim 215\text{N}$, the AMB will be able to generate a compensating counter force with an air gap of 2mm within a current range from 0A to 25A (according to the range of the intended current sources). A sufficient margin is left to dynamically move the rotor corresponding to a bearing related fault emulation. As can be observed, due to the amount of specific literature on this topic, dimensioning the AMB's steady state force range is relatively straightforward.

Parameter	Value	Unit
N	400	$[-]$
A_a	$l \cdot b$	$[\text{m}^2]$
l	0.075	$[\text{m}]$
b	0.012	$[\text{m}]$
l_{stat}	0.16	$[\text{m}]$

Table 5.2: Variable AMB parameters

5.2.2 Electromagnetic finite element simulation

To increase the assurance that the bearing is well designed, especially the flux linkage between the bearing and the shaft of the machine, the FEA software *Flux 2D - Cedrat®* is used. In that software package, phenomena such as eddy currents, hysteresis losses, saturation effects... are taken into account. Also the effect of the rotational speed of the shaft on the flux linkage can be analyzed. It is of crucial importance that the inductance between the stator and the rotor is comparable with the analytical calculations. If for example some field lines are not completely closing through the rotor shaft, the inductance decreases which results in a smaller attractive force $u(t)$ for the same electrical current $i(t)$. Therefore, several shapes of pole shoes with different roundings of the pole-tip were extensively tested in order to optimize the transferring flux path through the air gap. Figure 5.4a presents the most optimal FEA simulation where the upper pole is powered with 5A and the other poles with 1A.

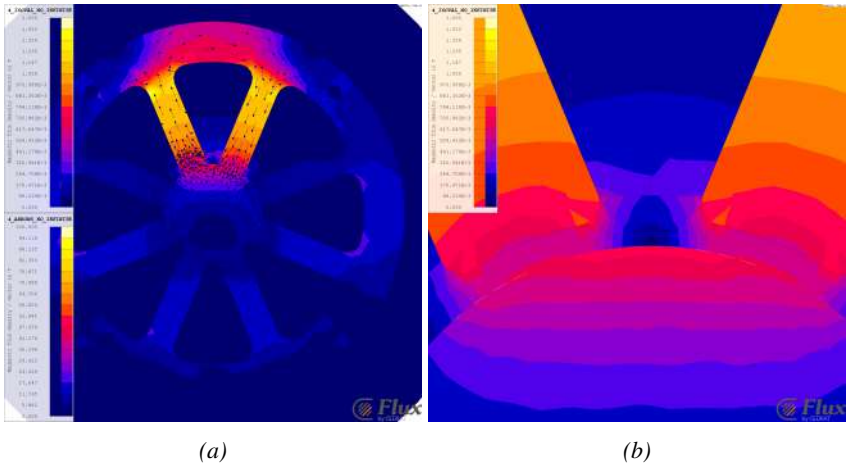


Figure 5.4: *Flux 2D®* simulation flux density (a) with 5A in the upper pole and 1A in the lower, left and right pole and a zoom in (b)

A more detailed version of Figure 5.4a is illustrated in Figure 5.4b. It can be observed that the flux density in the air gap is $\sim 0.617\text{T}$, which is highly comparable with the analytic calculations (0.619T for 5A through the winding or 2000Aw). Thereby, it is confirmed that the constructive dimensions of the AMB will meet the required conditions in force range. If the proper magnetic material can be found with an accurate winding installation, the AMB will be able to compensate all interacting forces. Nevertheless, it is important that the bearing is dynamic enough to generate fast varying forces which induce the fault related rotor movements. As the AMB is an inductive electrical load, this challenge is not negligible.

5.3 AMB dynamics

To induce the desired rotor movements e.g. $y_o(t)$ and $x_o(t)$ out of Chapter 4, dynamic varying forces of $u(t)$ are required in each of the four windings. Consequently, following (5.1), a dynamic varying current $i(t)$ is required. Since the currents through the AMB windings are driven by H-bridge current regulators, the dynamics of the electrical system are highly dependent on the switching DC voltage, $v(t)$. In other words, to induce a fast varying current, a large voltage is needed. Because the AMB is an inductive/resistive load, the current change and furthermore the rotor displacement lags the applied change in voltage. In the following equations on the electrical aspects of the AMB, the rotor movements defined by $y_o(t)$ and $x_o(t)$ are interpreted as an air gap variation $z(t)$ at one of the four winding point of view. This is because the expressions would apply for all four windings/force generators. The exact relation between the applied voltage $v(t)$, the current through the AMB windings $i(t)$ and the air gap variation $z(t)$ can be expressed as [32]:

$$v(t) = R_w \cdot i(t) + L_w(t) \frac{di(t)}{dt} + K_i \cdot \frac{dz(t)}{dt} \quad (5.2)$$

with: R_w , the winding resistance; $L_w(t)$, the winding inductance and K_i , the current stiffness, further clarified in (5.6). This last factor corresponds to the voltage induced in the winding due to the magnetic rotor shaft which is moving within the AMB magnetic field.

The amount of flux generated by a pair of poles that closes through adjacent poles of another force generator (winding) is negligible when the magnetic fields of those adjacent poles have the same spatial direction. This will be confirmed by FEA further in this section, Figure 5.11. Consequently, the mutual inductances between the four windings/force generators is negligible. Therefore, the total inductance of each winding can be written as [32]:

$$L_w(t) = \frac{N^2}{\mathcal{R}_m(t)} \quad (5.3)$$

with the reluctance path $\mathcal{R}_m(t)$, highly depending on the air gap $z(t)$, defined as [32]:

$$\mathcal{R}_m(t) = \frac{l_{\text{stat}}}{\mu_{r_{\text{stat}}} \cdot \mu_0 \cdot A_a} + \frac{2 \cdot z(t)}{\mu_0 \cdot A_a} + \frac{l_{\text{sh}}}{\mu_{r_{\text{sh}}} \cdot \mu_0 \cdot A_a} \quad (5.4)$$

As the focus of the AMB is imposing fault related rotor movements following $y_o(t)$ and $x_o(t)$, the air gap $z(t)$ for each winding, the reluctance path $\mathcal{R}_m(t)$ and subsequently the winding inductance $L_w(t)$ changes inevitably for every winding. To ensure that the AMB is dynamically able to emulate the fast varying rotor movements obtained in §4.3, the complex relation between current and position is simulated in the next section in order to verify the performance and optimize the control system of the AMB system. From thereon, the required DC voltage of the H-bridge current sources is determined. That voltage is the most crucial parameter concerning the system dynamics. Comprehensibly, as following (5.2), a high DC voltage implies the ability of a fast varying current, hence a dynamically varying force and displacement.

5.3.1 AMB control design

To simulate the physical AMB system and its control loop behavior, *Matlab - Simulink*[®] is used. The entire physical AMB system (electrical and mechanical) is modeled and presented for the vertical axes in Figure 5.5. Although current sources are applied, the AMB model input is the supplied voltage on the upper, lower, left and right winding. This because the H-bridge current source is a hard chop switching DC voltage with current control. The output of the model is the rotor position in the vertical direction, $y(t)$. The AMB model contains a combination of the formulas (5.1) and (5.2). Set-points for current are outputs of the PID controllers (one for the vertical and one for the horizontal direction), designed according to (5.5). The input of the PID controller is the error between the real position and the set-point for position. In order to enhance the stability, an ever present force is implied by adding a bias current i_{bias} in each winding, [32, 88, 90].

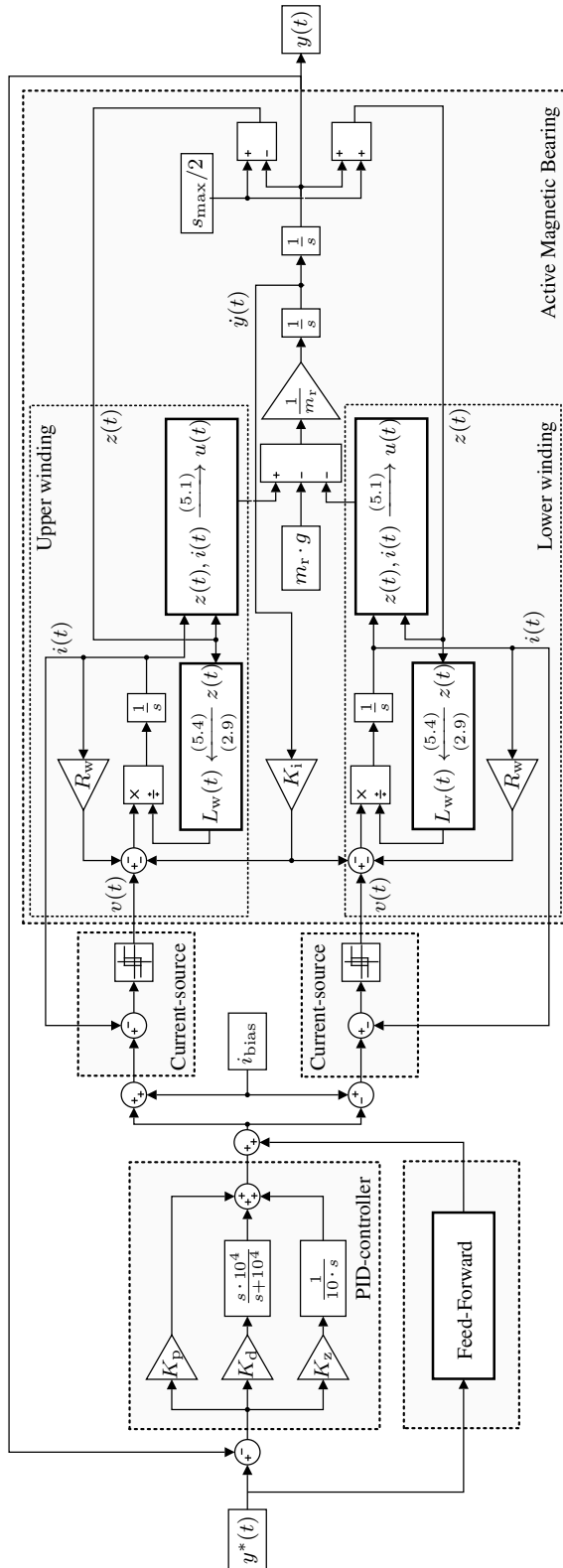


Figure 5.5: Simulink based model of the vertical AMB system

Based on literature, two equal PID controllers are designed for vertical and horizontal direction in order to control the position of the rotor with respect to the stator, [32, 88, 90, 92]. The PID controller $L_{\text{PID}}(s)$ can be expressed in the s-domain with s the Laplace operator, [92]:

$$L_{\text{PID}}(s) = K_p + K_d \frac{s \cdot 10^4}{s + 10^4} + K_z \frac{1}{s \cdot 10} \quad (5.5)$$

with:

$$K_p = \frac{m_r \cdot \omega_n + K_z}{K_i}$$

$$K_d = \frac{2 \cdot m_r \cdot \omega_n \cdot \psi + K_z}{K_i}$$

where ω_n is the bandwidth, in [rad/s], of the PID controller and ψ is the controller overshoot. K_z and K_i are respectively the position stiffness and the current stiffness of the AMB. They are a result of the linearization of (5.1) and are calculated as follows, [32, 88]:

$$u = m_r \cdot g + K_i (i - i^*) + K_z (z - z^*) \quad (5.6)$$

with:

$$K_z = \left. \frac{\partial u}{\partial z} \right|_{i^*, z^*} = - \frac{4 \cdot \mu_0 \cdot A_a \cdot \cos \alpha \cdot N^2 \cdot i^{*2}}{\left(\frac{l_{\text{stat}}}{\mu_{\text{rstat}}} + \frac{l_{\text{sh}}}{\mu_{\text{rsh}}} + 2 \cdot z^* \right)^3}$$

$$K_i = \left. \frac{\partial u}{\partial i} \right|_{i^*, z^*} = \frac{2 \cdot \mu_0 \cdot A_a \cdot \cos \alpha \cdot N^2 \cdot i^*}{\left(\frac{l_{\text{stat}}}{\mu_{\text{rstat}}} + \frac{l_{\text{sh}}}{\mu_{\text{rsh}}} + 2 \cdot z^* \right)^2}$$

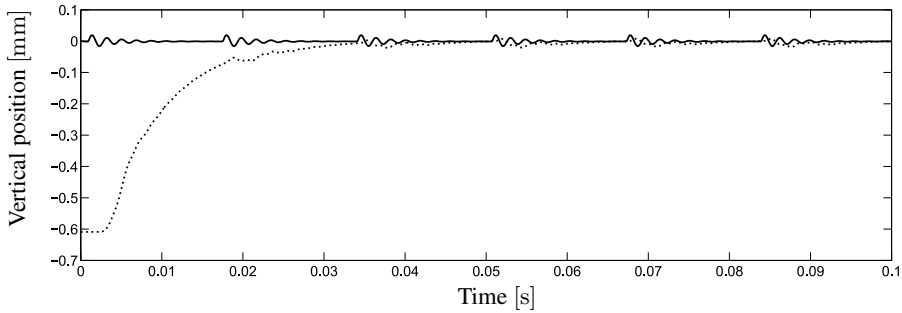
with $z^* = 2\text{mm}$ and i^* can be derived out of (5.1), where $z(t) = z^*$ and $u(t) = m_r \cdot g$. These values for z^* and i^* correspond to the air gap and current through the upper winding when the rotor is lifted and centered in the AMB. In order to be sure that the AMB behaves as the original mechanical bearing did, the stiffness k_r and damping c_r of the original mechanical bearing is matched with the stiffness and damping properties of the AMB. [93] is the first to publish the estimation of the stiffness and damping properties for the entire control loop and the real magnetic bearing system on an experimental basis. This leads to the possibility of adapting the control loop properties in order to manipulate the overall characteristic system stiffness and damping properties, including the effect of the rotational speed. As a consequence, these optimization equations are used in this research to adapt the overall system characteristics by fulfilling: [93]:

$$k_r = - (K_z + K_i) \cdot \text{Re} [L_{\text{PID}}(j \cdot \omega_e)] \quad (5.7)$$

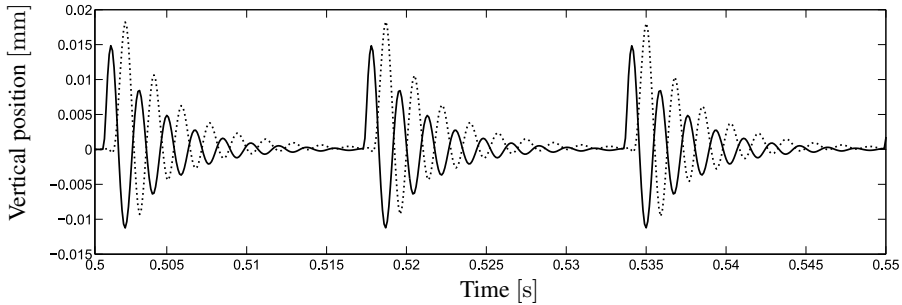
$$c_r = - \frac{K_i}{\omega_e} \cdot \text{Im} [L_{\text{PID}}(j \cdot \omega_e)] \quad (5.8)$$

where ω_e is the external excitation frequency and j is the imaginary unit. In this application, $\omega_e = 2\pi \cdot f_r$. Despite the fact that the stiffness and damping properties of the AMB will not be equal to the real mechanical bearing for the whole

frequency range, it will be equal for the most influential excitation frequency f_r . Consequently, in order to imply the faulty rotor movements, containing numerous excitation frequencies, the forces generated by the AMB will never exactly correspond to the faulty impulse functions $h_{y,o}(t)$ or $h_{x,o}(t)$ as obtained in Chapter 4. Nevertheless, the fault related rotor movements are still analytically obtained in §4.3 based on k_r and c_r and will be propagated as it would be from the original mechanical bearing. Conclusively, the forces between stator and rotor will be different in the fault emulator as it would be on a real faulty bearing, but the imposed stator/rotor displacement will be equal. This because the system properties (stiffness and damping) of the mechanical bearing are matched with the magnetic bearing for only one frequency, the rotational speed f_r and not for the whole transfer function.



(a) The set-point for the rotor (full line) and the corresponding simulation result (dotted line)



(b) Simulation result: set-point (full line) and rotor position (dotted line)

Figure 5.6: Comparing the simulation results with the set-points for a single point outer race bearing fault

Parallel to the PID-controller, a Feed-Forward is implemented in the control loop (see Figure 5.5) to benefit the fault emulation. This feed forward uses the inverse form of the obtained AMB-model to calculate the required current profile in order to obtain a specific set point. This means that, based on the applied rotor movements, the Feed-Forward estimates the current profile needed to generate these movements without taking into account the real rotor position. This implementation benefits the effectiveness of the overall control loop significantly.

Implementing the designed control system $L_{PID}(s)$, simulation is conducted. In the simulation, the rotor is at start virtually placed in an idle position on the

physical bottom of the magnetic bearing ($\sim -0.6\text{mm}$). At time $t = 0\text{s}$, a vertical set-point corresponding to $y_o(t)$ (as in Figure 4.10) is provided to the control system. The simulation result, presented for the vertical direction as a dotted line in Figure 5.6a, states that the rotor is centered within $\sim 40\text{ms}$. A more detailed view of the set-point (full line) and the system response (dotted line) in a later time frame is illustrated in Figure 5.6b. In that time frame, a clear lag of $\sim 1\text{ms}$ can be observed due to the implemented delay of the real-time PC and its control loop ($100\mu\text{s}$ cycle time). However, due to the independence of the angular position of the bearing balls in reference to the IM's angular rotor position, the phase shift between the set-point and the simulation response is of negligible importance. Although a difference in magnitude can be observed, it can be concluded that the AMB system sufficiently fulfills the dynamic requirements in order to emulate a very specific single point outer race bearing fault. The full designed system is able to generate these fast varying fault related rotor movements. It must be noted that, even when the phase and magnitude of the real rotor movements deviates with the set-points, the real rotor movements can inversely be recalculated to the force function $h_{y,o}(t)$ and $h_{x,o}(t)$ in which the specific dimensions of the original bearing pit can be determined (see §4.3). Thus, if it is observed that the AMB does not exactly generate the movement according to the required set-point, the fault severity can be calculated out of the real rotor movement. However, the real focus of this simulation is the verification of the dynamic behavior of the dimensioned AMB and its control loop. The H-bridge DC voltage is determined by varying the DC voltage from 24V to 240V while accordingly verifying the achievement of the rotor movements. Out of those simulations, a voltage of 140V is determined to be sufficient. Nevertheless, current sources with a DC voltage of 170V are implemented in order to maintain a certain dynamic flexibility. Nevertheless, although an increase in DC voltage would benefit the AMB dynamics, the designed current sources have to be commercially available.

Utilizing the AMB model, extensive simulations were performed focusing on compensating mechanical and magnetic unbalance, position measurement disturbances/interferences, mechanical torque ripples, magnetic rotor/stator distortions, AMB parameter sensitivities, inner and aouter race bearing fault emulation... All simulations confirmed the compliance of the total AMB system when current sources are implemented with a range of 0A till 25A, a DC voltage of 170V and a maximum switching frequency of 20.7kHz. It must be noted that this does not imply that one winding needs a full power of $25\text{A} \cdot 170\text{V} = 4.25\text{kW}$. The current range determines the force range and so the dissipated power in the winding, while the voltage range only determines the dynamics of the force. The voltage will eventually continuously switching between 0V and 170V, corresponding to a RMS voltage of $\sim 3\text{V}$ in the upper winding during operation (obtained in simulation). The power needed for countering gravity is then calculated to be $\sim 12\text{W}$. If one of the windings is actually pushed to the limit of its force range, being $u(t) = 2.2\text{kN}$ with $i(t) = 25\text{A}$ and $z(t) = 2\text{mm}$, a power of 350W is dissipated. The corresponding RMS of the voltage $v(t)$ is only $\sim 14\text{V}$. In order to be able to deliver the full AMB power when needed, a DC source of 1kW is installed to feed all four current sources. This is inevitably over-dimensioned, as the maximum required power by the control system can only be $2 \cdot 350\text{W}$ in two perpendicular

directions. Apart from the bias currents, the control system will never demand current in the upper and lower winding at the same time, as it is an inherent property of the control topology (Figure 5.5).

5.4 Practical implementation

Now all the AMB components are dimensioned and meet all requirements following its model, the hardware can be acquired, constructed and assembled. This part is subdivided in four sections. First, the position measurement is elucidated. These signals are of major importance for the current control system, which is implemented in a real-time controller, handled in the second section. Third, the practical implementation of the AMB in the IM is described. The concentric alignment of the stator and the AMB is crucial in order to impose the rotor movements relevant to a real faulty situation.

5.4.1 Position measurement

One of the more crucial parts in the control system is the measurement of the rotor position with respect to the stator. As the shaft material is ferromagnetic material, two MTN/EP200, *Monitran* eddy current probes are used with a range of 0mm-5mm. In order to suppress noise and increase accuracy, position is measured on a very smooth, approximately a perfect round-shaped surface. It is of major importance that when the rotor is perfectly centered and rotating at 1500rpm, the eddy-current probes measure a constant value. To obtain this goal, an inner race of a needle bearing is placed over the shaft on the axial position where the eddy-current probes are installed. This ensures that the eddy current probes do not notice a difference in speed of the rotating rotor, but only measure the radial shaft position.

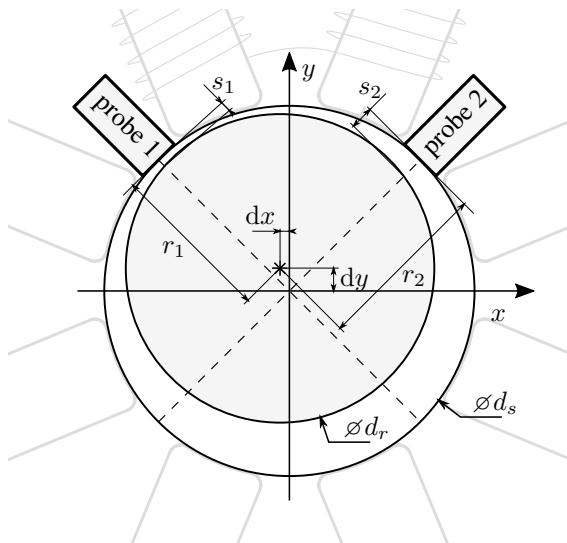


Figure 5.7: Transformation from s_1 and s_2 to dx and dy

The current probes are tactically placed due some constructional limitations as presented in Figure 5.7. This means that a transformation must be applied in order to determine dx and dy (error between the rotor center and the stator center) out of

measuring the distances s_1 and s_2 . Those errors in vertical and horizontal position are required for the previously dimensioned control system. The transforming equations related to the distances illustrated in Figure 5.7 are:

$$dx = \frac{\sqrt{2}}{2} (s_1 - s_2) \quad (5.9)$$

$$dy = \frac{\sqrt{2}}{2} (d_s - d_r - s_1 - s_2) \quad (5.10)$$

With:

dx	horizontal difference between rotor and stator center [mm];
dy	vertical difference between rotor and stator center [mm];
s_1	measured distance by eddy current probe 1 [mm];
s_2	measured distance by eddy current probe 2 [mm];
d_s	diameter of sensor placement [mm];
d_r	diameter of rotor shaft [mm].

The eddy current probes can axially not be placed at the exact position where the original mechanical bearing was installed, because that is where the AMB is located. All of this is to ensure that the forces imposed on the rotor are at the axial position of the original mechanical bearing. The position set-point (as in Figure 4.10) is the displacement of the rotor at the axial location of the faulty mechanical bearing. Therefore, a correction factor must be implied to transform the measured rotor displacement to the displacement of the rotor at the axial center of the original mechanical bearing, equal to the axial center of the AMB. The correction factor can be determined via Figure 5.8 by dividing x_3 with x_4 , corresponding to respectively the distance between the original mechanical bearings and the distance between the NDE bearing and the sensors. Due to the fixed radial rotor position at the NDE mechanical bearing, the rotor position dx' and dy' at the center of the AMB can be described as (5.11). The values dx' and dy' will be used as feedback positions in the control loop. The factor x_3/x_4 is measured to be 0.8125.

$$dx' = \frac{x_3}{x_4} dx \quad \text{and} \quad dy' = \frac{x_3}{x_4} dy \quad (5.11)$$

5.4.2 Current control

After measuring position and estimating the rotor position with respect to the stator in the vertical and horizontal position, the voltage signals are captured using a *Speedgoat*® real-time controller (Figure 5.9a). This controller executes the control loop as presented in §5.3.1 at a cycle time of 100µs. The output of the PID controllers (horizontal and vertical) are four set-points for current for the upper, lower, left and right winding. The current sources are H-bridge current sources of the type *AZB25A20* of the company *Advanced Motion Control (AMC)*®. They are able to control current between 0A and 25A with a maximal switching voltage of

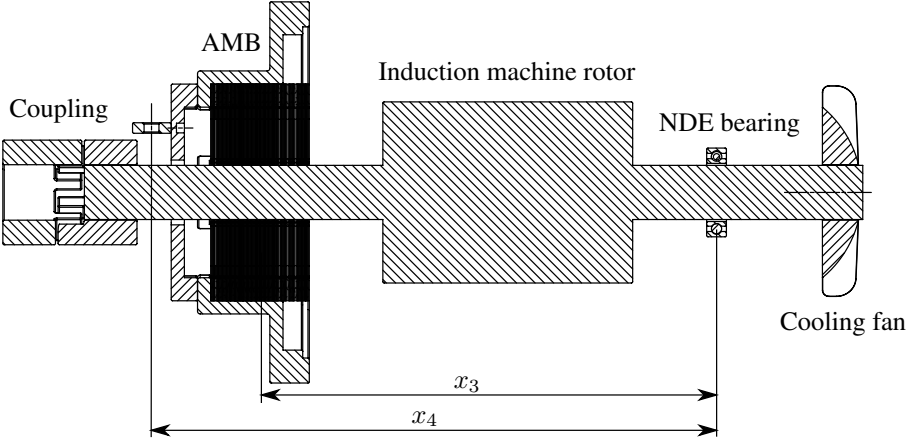


Figure 5.8: Distance x_3 between the original mechanical bearings and x_4 between the sensors and the bearing at NDE

200V at 20.7kHz based on a 0V to 10V input signal. The DC source feeding all four H-bridge sources is a power supply of 170V DC, 50A. One current source and the used power supply are illustratively presented in Figures 5.9b and Figure 5.9c. Conclusively, with this setup, the ability is created of controlling the current through all four AMB windings based on the measurement of position with high dynamics and accuracy.

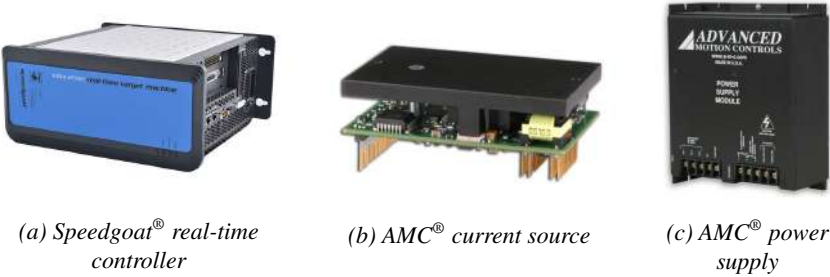


Figure 5.9: The current sources which control the current through the four windings based on the output of the real-time controller

5.4.3 The AMB

The production of the AMB dimensioned in §5.2.1 was relatively convenient. Based on the physical constraints, bearing topology and magnetic FEA, the obtained CAD drawings were sent to the manufacturer who punched the AMB lamination out of 1mm electrical steel. This specific width for the lamination sheets was not chosen because of dimensional/energetic incentives (as the magnetic flux is one-directional and almost no eddy currents are induced), but because of constructional reasons regarding the punching process. 75 laminations are used to

stack the magnetic material. Subsequently, the four windings are mounted manually (200 turns per pole/coil, 400 turns per winding). It is crucial that the AMB is perfectly centered and aligned to the stator housing of the electric machine. Therefore, a special mounting structure is designed (Figure 5.10a). The assembly of the whole system can be found in Figure 5.10b. The claws of the mounting structure are well designed fittings to make sure that the concentric tolerances are minimal. The back of the structure is similarly shaped as the flange of the electric machine. The used material for the mounting structure is aluminum, for its non-magnetic properties.

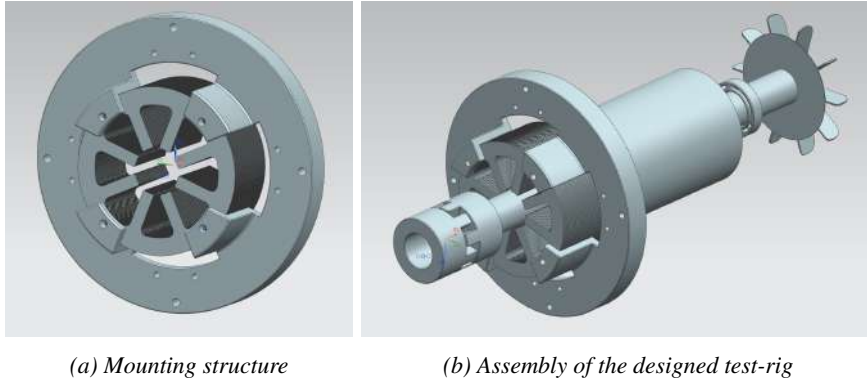
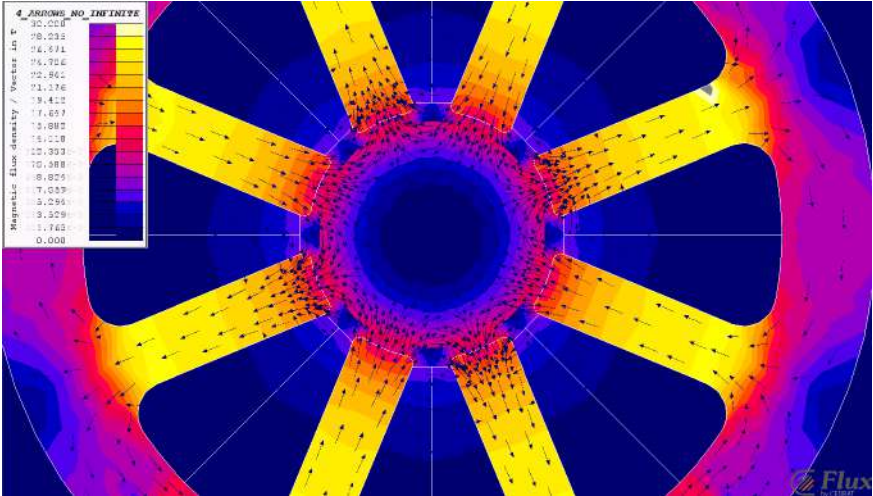


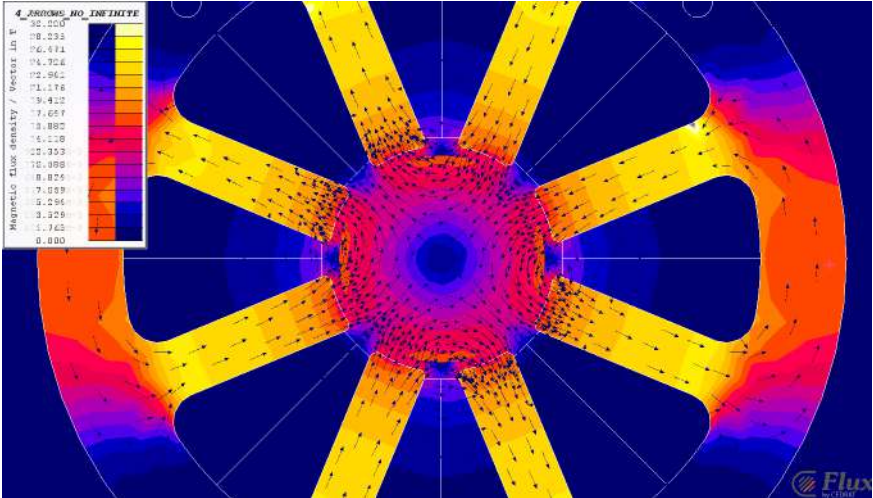
Figure 5.10: Perfect alignment between the AMB and stator housing of the electric machine using an Aluminum mounting structure

The DC current through each winding creates a flux which is determined to form a closed flux path through one pair of poles. Inevitably, the flux path will close as well through adjacent poles. This flux will not induce any voltage in the adjacent windings as it has one polarity, but it will sum up with the flux induced by the other poles. This can disturb the working of the control system significantly. In order to minimize this effect, every pair of adjacent coils of two different windings are connected to the current sources in such a way that the current flows in the same direction. This implies the magnetic field to be the same, resulting in the same repulsive polarity in the adjacent pole tips. Consequently, the induced flux in between these adjacent poles is minimized. Figure 5.11a and Figure 5.11b are magnetic FEA simulation results demonstrating the difference when the current direction is alternating every pole, or when its alternating every two coils. The current through the windings is set to be a constant 5A in every coil. This is no realistic situation, but it graphically demonstrates the induced fluxes in every pole. The simulation results indicates the importance of the alternating current per winding. The flux density in the shaft is consequently increased, resulting in obtaining the previously dimensioned force range.

An interesting thing to investigate in this research is the mutual inductances between the different coils of the AMB. As the switching current control will imply a time-varying DC current (not a constant DC signal), this current variation through any winding will unavoidably generate an alternating magnetic field which induce voltage in its adjacent coils. That induced voltage, if confirmed to be significant,



(a) Current is changing direction every pole



(b) Current is changing direction every two pole (per winding)

Figure 5.11: Flux 2D® simulation of the flux density with different current directions

can disturb the current in that affected coil and subsequently disturb the control loop. In the FEA simulations, the rotor is considered to be perfectly centered within the stator. In reality, the rotor is constantly moving around in the AMB, which can result in different interactions of the mutual inductances between the four windings. Additionally, due to imperfections in the magnetic material and errors in the manually installed windings, an unequal distribution of magnetic field affect the mutual inductances as well. Consequently, only conducting measurements on the real magnetic bearing can visualize the self and mutual inductances and their dependency on the rotor position. Of course, as inductance is only defined for a change in current, an AC current is used in this experiment. As it

already was presented, the relation between voltage, current and inductances of one winding with neglecting mutual inductances is:

$$v(t) = R_w \cdot i(t) + L_w(t) \frac{di(t)}{dt} + K_i \cdot \frac{dz(t)}{dt} \quad (5.12)$$

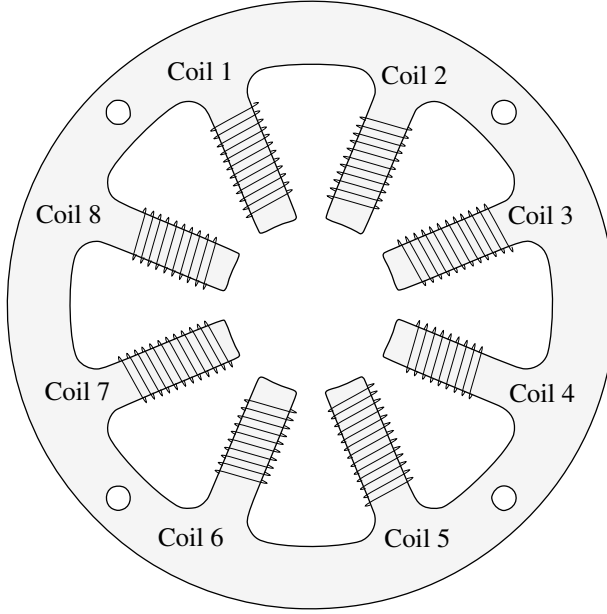


Figure 5.12: Separating the AMB into eight separate coils in order to obtain the self and mutual inductances

To obtain a full and clear view on the mutual and self inductances of the AMB, the four windings are separated into eight independent coils around every AMB pole, assigned as in Figure 5.12. This results in the correct equation for the relation between voltage and current for coil k as:

$$v_k(t) = R_k \cdot i_k(t) + L_k(t) \frac{di_k(t)}{dt} + \sum_{l=1}^8 \left[M_{k,l}(t) \cdot \frac{di_l(t)}{dt} \right] + K_i \cdot \frac{dz_k(t)}{dt} \quad (5.13)$$

where $v_k(t)$, $i_k(t)$ and R_k are respectively the voltage, current and resistance of coil k ; $L_k(t)$ is the self inductance of coil k and $M_{k,l}(t)$ is the mutual inductance of coil l to coil k . $z_k(t)$ is the time varying distance between each pole k and the rotor shaft. During measurements, different rotor positions will be taken in a stabilized situation (no transient in the air gap). This implies that the time dependency of $z_k(t)$ can be neglected. Consequently, the term $K_i \cdot dz_k(t)/dt$ is nullified which benefits the complexity. However, following (5.3) and (5.4), this does not imply that the components $L_k(t)$ and $M_{k,l}(t)$ are constant parameters. They remain dependent on the air gap between each pole and the shaft, z_k . This results in the following full matrix notation of the relation of voltage and current for steady state

rotor positions:

$$V(t) = R \cdot I(t) + M(z) \frac{dI(t)}{dt} \quad (5.14)$$

where:

$$V(t) = \begin{bmatrix} v_1(t) \\ v_2(t) \\ v_3(t) \\ v_4(t) \\ v_5(t) \\ v_6(t) \\ v_7(t) \\ v_8(t) \end{bmatrix} \quad R = \begin{bmatrix} R_1 \\ R_2 \\ R_3 \\ R_4 \\ R_5 \\ R_6 \\ R_7 \\ R_8 \end{bmatrix} \quad I(t) = \begin{bmatrix} i_1(t) \\ i_2(t) \\ i_3(t) \\ i_4(t) \\ i_5(t) \\ i_6(t) \\ i_7(t) \\ i_8(t) \end{bmatrix} \quad (5.15)$$

and:

$$M(z) = \begin{bmatrix} L_1(z_1) & M_{1,2}(z_1, z_2) & \cdots & M_{1,8}(z_1, z_8) \\ M_{2,1}(z_2, z_1) & L_2(z_2) & & \vdots \\ \vdots & & \ddots & \\ M_{8,1}(z_8, z_1) & \cdots & & L_8(z_8) \end{bmatrix} \quad (5.16)$$

Equations (5.3) and (5.4) elucidate a very important property of the matrix $M(z)$. The relation between inductance in coil k and the distance z_k is inversely proportional $\sim 1/z_k$. This implies that the matrix $M(z)$ can be written as a function of Z , resulting in the definition of the time and position independent matrix C :

$$M(z) = C \cdot Z \quad (5.17)$$

where:

$$Z = \begin{bmatrix} \frac{1}{z_1} \\ \frac{1}{z_2} \\ \frac{1}{z_3} \\ \frac{1}{z_4} \\ \frac{1}{z_5} \\ \frac{1}{z_6} \\ \frac{1}{z_7} \\ \frac{1}{z_8} \end{bmatrix} \quad (5.18)$$

This rotor position dependent matrix can subsequently be rewritten as a function of the rotor coordinates x and y , being the respectively horizontal and vertical rotor position as:

$$Z = T \cdot \begin{bmatrix} x \\ y \end{bmatrix} \quad (5.19)$$

with the transformation matrix T consisting of constant values only.

The matrix C should theoretically be a symmetrical matrix, independent on time or rotor position. It reflects an overall relation between the quantities of the

self and mutual inductances and represents imperfections of the AMB construction. As these parameters reflect the question on the mutual inductances perfectly, this matrix is constructed by measurements. By synchronously measuring voltage in every coil and sequentially inducing current (1A, 50Hz) in every coil, the inductance matrix was constructed for a numerous rotor positions. As a result, the position and time independent matrix C is calculated to be:

$$C = \begin{bmatrix} 15.212 & 4.236 & 1.058 & 0.782 & 0.761 & 0.821 & 1.032 & 3.837 \\ 4.248 & 15.381 & 4.280 & 1.154 & 0.901 & 0.761 & 0.758 & 1.015 \\ 1.092 & 4.277 & 15.175 & 4.062 & 1.367 & 0.912 & 0.681 & 0.747 \\ 0.728 & 1.201 & 4.121 & 15.087 & 4.071 & 1.406 & 0.834 & 0.682 \\ 0.721 & 0.860 & 1.284 & 4.278 & 15.225 & 4.052 & 1.352 & 0.845 \\ 0.821 & 0.720 & 0.836 & 1.302 & 4.168 & 15.132 & 4.275 & 1.182 \\ 1.077 & 0.758 & 0.681 & 0.834 & 1.278 & 4.122 & 15.007 & 4.472 \\ 3.835 & 1.013 & 0.747 & 0.682 & 0.881 & 1.153 & 4.567 & 15.124 \end{bmatrix} \cdot 10^{-5}$$

The matrix, graphically presented for each coil in Figure 5.13, confirms that there are some imperfections in the AMB as the diagonal values are not all exactly the same. Nevertheless, the matrix can be assumed to be significantly symmetric, as there is a strong diagonal relation. It can be noticed that, as literature describes, the mutual inductance from fictional coil A to B is exactly the same as from coil B to A (coinciding measurement values). Additionally, the difference between the self and the mutual inductance is rated to be large. Certainly when the adjacent poles are neglected as it is a part of the AMB winding topology (two poles form one force-generator). The induced voltage in the next to adjacent pole is negligible with respect to the self inductance (only 6%). This experiment states that when the current through the windings of the magnetic bearing will fluctuate due to the varying set-points for the control loop, there will be voltage induced in other windings which will affect the current through and flux induced by that winding. Although there will be a disturbing effect for sure, it will be of an insignificant amount. This mainly because the alternating factor is relatively small in relation to the DC component. The next section will confirm that this phenomena will not noticeably affect the performances of the AMB.

5.4.4 Validating experiment

As the AMB is now implemented in the 11kW IM, presented in Figure 5.14, the evaluation of the real AMB system performances with the AMB model used in simulation can be conducted. With the use of an interactive user interface, the AMB can be activated and the set-points for the horizontal and vertical direction can be adjusted on-line. This is a crucial property, as now the operational parameters remain constant. Consequently, it enables the possibility of varying the fault severity during operation. Thereby, the effect on the stator current can be logged as a time varying signal. The experiment performed contains the emulation of a single point outer race bearing fault, discussed in §5.3.1 and characterized in Table 4.1. The time based set-point $y_o(t)$ (full line) and the real rotor position (dashed line) can be found in Figures 5.15a and 5.15c. Illustratively, the simulation results

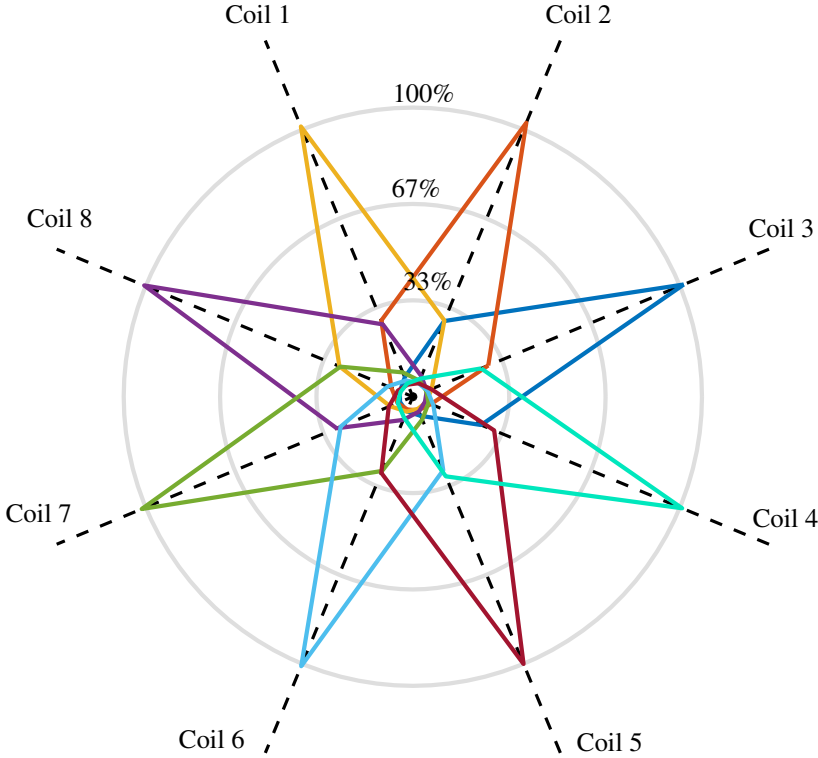


Figure 5.13: The spatial presentation of matrix C for all 8 coils in the AMB, representing the rotor position independent values for the mutual inductances relatively to the self inductances

are again plotted in Figure 5.15b in order to compare the AMB model and the real AMB. If the real AMB obtains the same results as the AMB model, there is an increase in the certainty that all fault emulations will be representative. The main difference between the AMB model and the real AMB can be observed in Figure 5.15a. The approximated step response of the AMB model is already stabilized within $\sim 40\text{ms}$ while the real AMB requires $\sim 80\text{ms}$ to center the rotor. Also the rise time of the two responses differ a lot. The deviation is most likely due to neglecting the mass, stiffness and damping properties of the complex coupling between the IM and the load (visible in Figure 5.14). A small deviation in those parameters imposes a significant impact on the step response. Nevertheless, this step response does not determine the exact behavior of the AMB as the control loop is (due to the linearization) optimized for small deviations around the stator center. About this linear behavior visualized in Figure 5.15a, the non-linearities of the complex voltage/current/position relation can be noticed by the atypical gradient of the response function. The noticeable time lag of $\sim 3\text{ms}$ in the response when the step is applied is mainly due to the residual magnetization being present between the rotor and the AMB. However, the most important functionality of the AMB is

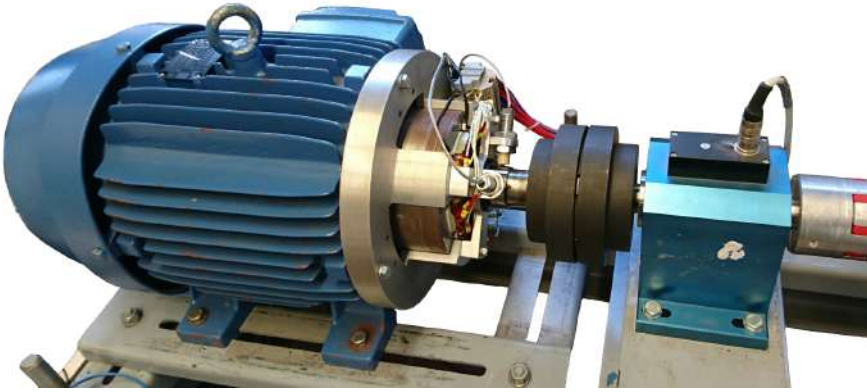
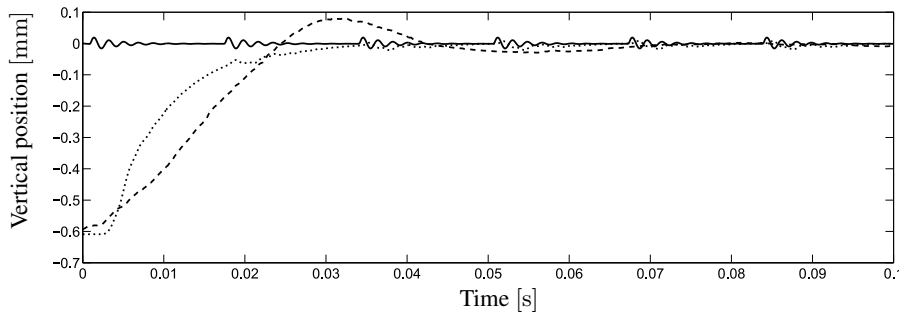
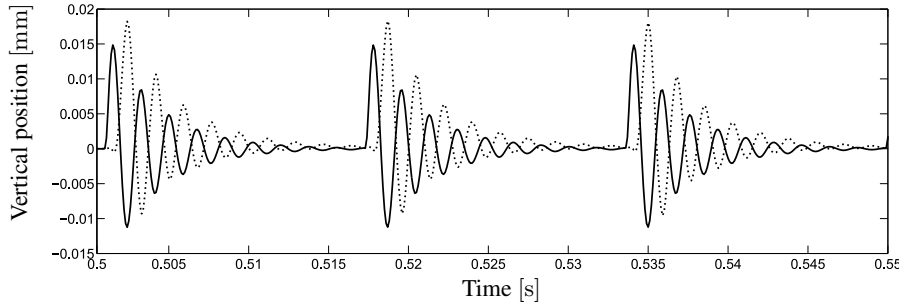


Figure 5.14: The AMB implemented at DE side of the 11kW IM

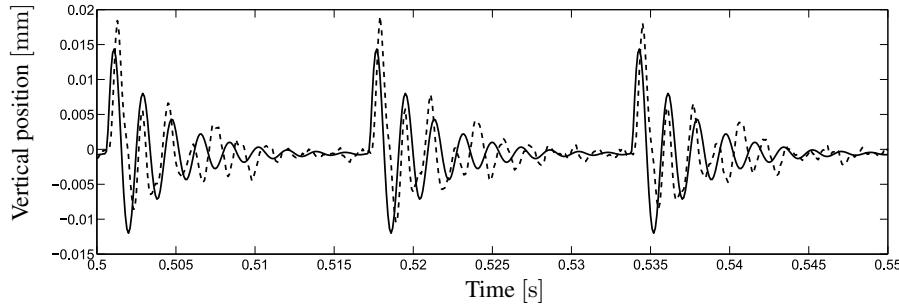
the emulation of the mechanical faults, hereby validated using the obtained movements of the rotor severing a single point outer race bearing fault. By applying the previously obtained rotor movements as a set-point on the AMB control loop, Figure 5.15c is constructed presenting the set-points and the real response. Regarding the single point outer race fault emulation, the real AMB achieves really satisfying results, even more satisfying with respect to the simulation result. The high-dynamic movement is obtained by sufficient accuracy. Certainly by considering that only the lowest periodic frequency components (f_{out} , §2.3.3) are actually analyzed in the spectrum. Consequently, it is stated that the test-rig is sufficiently able to emulate the single point outer race bearing faults. Further experiments were conducted on different severity stages for both outer and inner race bearing faults. Repetitively, the AMB was able to accurately emulate the analytically obtained rotor movements. Furthermore, in some emulation experiments, the stator current was analyzed with focus on detecting the bearing faults. Fortunately, the bearing fault signatures were found in the exact way as they propagate with a real faulty bearing, [2, 39]. However, these experiments are extensively discussed in the next chapter.



(a) The set-point for the rotor (full line) and the corresponding simulation (dotted line) and emulation result (dashed line)



(b) Simulation result: set-point (full line) and rotor position (dotted line)



(c) Emulation result: set-point (full line) and rotor position (dashed line)

Figure 5.15: Comparing the simulation results with the emulation results for a single point outer race bearing fault

5.5 Conclusion

This chapter was one of the more challenging parts in this dissertation. The idea of inducing fault related rotor movements by manipulating the rotor position in an IM was executed by replacing a mechanical bearing with an active magnetic bearing. First, the force range was determined by the gravitational force, the UMP and the unavoidable mass-unbalance. By adapting some variable physical parameters, the optimal AMB properties were determined. To ensure that the AMB is dynamically able to induce the specific rotor movements elucidated in the previous chapter, a simulative model was dimensioned and extensively tested. These results fixed among others the minimal DC voltage in the current sources. Subsequently, the AMB and its total system was constructed. Next to some constructional challenges e.g. aligning the AMB with the IM and measuring the rotor position sufficiently accurate, research was conducted on the mutual inductances between the separate windings and the corresponding interacting of these fluxes. All of this to estimate the influence of the mutual induced fluxes on the operating stability. However, the AMB was tested and was confirmed to meet the dynamic and static conditions. As the fault related rotor movements were defined in previous chapter and now the test-rig is finalized to induce those movements in a real 11kW IM, experiments can finally be conducted with the focus on finding relations between mechanical fault severity and their corresponding reflections in the stator current. Obtaining this kind of reproducible mechanical fault emulator is on this day a very unique contribution to the field of condition monitoring. This enables the investigation of the behavior of several mechanical faults and their impact on the induction machine. The possibilities of this fault emulator go far beyond this thesis and will certainly enhance the valorization of MCSA as a full and reliable CM-technology.

6

Experiments

6.1 Introduction

Finally, the core goal of this research can be achieved: finding relations between the severity of mechanical faults and their reflection in the IM stator current. Following the literature study in Chapter 2, it is clear how mechanical faults propagate towards the current. In Chapter 3, the current measurement method and signal processing techniques were determined in order to be able to find and differentiate those reflections in the stator current. The research elucidated in Chapter 4 resulted in a specific characterization of the specific rotor movements imposed by mechanical faults of several origin. These movements can now be induced in an 11kW IM, of which the practical test-rig was dimensioned and constructed in Chapter 5. This type of test-rig is unique in the way that mechanical faults can be reproducibly emulated in a real induction machine. As all the facilities to characterize and quantify the relations between the mechanical fault severity and the reflecting components in the stator current are obtained, pioneering research can now be conducted. This chapter is first discussing the measurement procedure, how the practical emulation is conducted and how the evolving faults will be linked with the stator current spectra. Secondly, all predefined mechanical faults are emulated with respect to fault severity. The mechanical faults which will be discussed are misalignment (§6.2), mass-unbalance (§6.3) and bearing faults (§6.4). The emulation of the bearing faults are then subdivided by single point outer race, single point inner race and bearing cage faults. It must be noted that in these experiments, only research was conducted on the impact of fault severity, as it is one of the most challenging parts within MCSA regarding mechanical faults. Future research will have to handle torque, speed, temperature, power quality conditions...

6.1.1 Emulating evolving mechanical faults

The reflection of the fault related signals in the stator current are small components with respect to the fundamental current component. In this stage of conducting scientific research, it is important that all influential conditions on the current spectrum are minimized. The current analysis may not be disturbed or interfered due to other phenomena. Therefore, effort must be made to ensure that all operational conditions during emulation are held as constant as possible. This includes torque, speed, temperature, voltage conditions... First, to guarantee the optimal power quality conditions and exclude any disturbing influence of the upper voltage grid, a 15kW controllable three phased voltage supply is used to drive the IM under test. Secondly, as the IM is directly fed by the power supply (\approx DOL) and consequently the only remaining load varying parameter is torque, the load machine is set up in torque control. This load machine is a DC machine with brushes, which is, due to its inherent properties, the perfect machine to control in torque mode (\approx current control). Thereby, it is guaranteed that the operational conditions are constant during emulation. Additionally, the environmental temperature is constantly logged in order to quantify its influence on the measurements. As other research abundantly addressed the importance of the machine internal temperature during experiments, the measurements are conducted when the 11kW IM is operating in thermal stability [94,95]. This equilibrium is reached by warming up the machine for ~ 2 h, graphically presented in Figure 6.2. This measurement was performed by logging the stator surface temperature during a warm-up under full load conditions. To ensure these thermal conditions and the constant operational settings, it is essential to adapt the conditions of the fault related rotor movements during operation. More specific for these experiments, the mechanical fault severity should be adapted on-line without shutting down the test-rig. To obtain this requirement, an easy accessible Graphical User Interface (GUI) is programmed which enables the ability of controlling the entire test-rig on-line. This GUI controls both the settings on the *Speedgoat*[®] real-time PC and the settings of the DC load-machine. The GUI is presented in Figure 6.1. Using this GUI, the power source and the thermal logging, the environmental conditions which have a significant effect on the machine behavior and its stator current are controlled. Conclusively, all kinds of mechanical faults can be emulated and imposed into the IM while all influential characteristics are held constant (or controllable).

6.1.2 Analyzing variations in the stator current

The machine under test is an 11kW *Totally Enclosed Fan-Cooled squirrel caged Induction Machine* with an efficiency class *EFF2*. The nameplate parameters of the IM are listed in Table 6.1. As the nominal stator current is indicated to be ~ 22 A, the current clamps and corresponding measurement topology described in Chapter 3 are excellent to be applied. Next to the three stator currents, the three-phased voltage is captured as well. Although the used power source assures a stable and pure sinusoidal voltage, possible signatures in the current due to voltage are thereby included in the analysis. Illustratively, the magnetic finite element model of this machine, presented in Figure 6.3, was constructed in a preliminary study on simulating mechanical faults. This figure elucidates informatively the

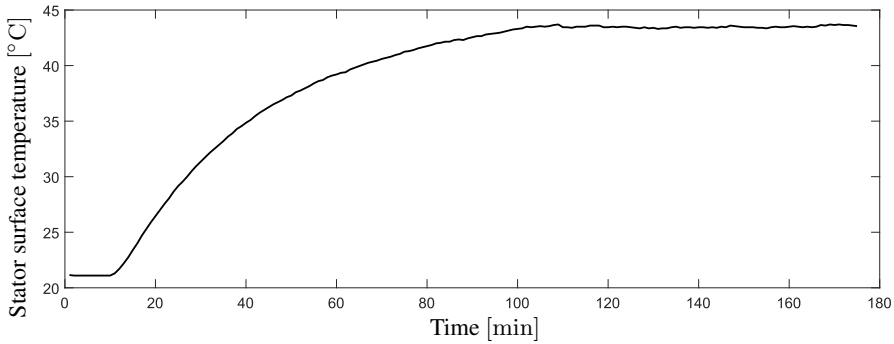


Figure 6.2: Thermal stability of the IM is obtained if the machine warms up under full load for at least 2h

Parameter	Value
Power	11kW
Nominal voltage	$\Delta 380V$
Nominal current	22.0A
$\cos \phi$	0.85
Frequency	50Hz
Nominal speed	1455rpm
Protection class	IP55
Efficiency class	EFF2 (IE1)

Table 6.1: Nameplate parameters of the IM under test

overall inner topology of the IM under test.

As the AMB ensures an accurate and reproducible emulation, now the variation in the stator current due to these emulations has to be analyzed. As discussed in Chapter 2, all mechanical faults can be indicated and detected due to spectral analysis or MCSA. This was mathematically expressed and implemented in Chapter 3. That chapter additionally indicated the usefulness of applying the EPVA (demodulation technique) in order to simplify the stator current analysis. As these experiments are focused on the impact of varying fault severity of any mechanical fault reflection in the stator current, it is now of great importance that these variations are accurately quantified and/or visualized. The mechanical faults are in practice adapted in severity by some predefined discrete steps. For example, The emulation of misalignment will be performed from $-400\mu m$ till $+400\mu m$ in steps of $5\mu m$. Consequently, for each step, the stator currents can be logged for several seconds in a stable operational situation. The measuring time is set on 10s per step in order to obtain a sufficient resolution of 0.1Hz in the spectrum. Subsequently, the frequency spectrum is obtained from the current signal $i_e(t)$, the re-

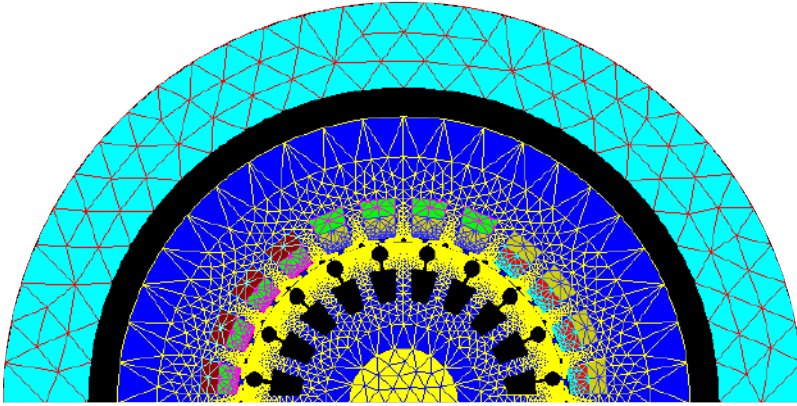


Figure 6.3: The inner construction of the 11kW IM under test

sulting vector out of the EPVA as discussed in §3.5. By doing this, the opportunity is created to analyze the current frequency spectra as a function of the mechanical fault severity. In this way, the influence of mechanical fault severity on the stator current fault components can easily be analyzed and visualized. To enhance the analysis furthermore, an algorithm is established which detects the variation of the spectral components as a function of fault severity. This avoids the suppression of valuable, varying spectral components between other spectral peaks which are not related to the emulated fault (e.g. current harmonics). Nevertheless, the algorithm takes all frequency components in consideration without focusing on the specific components related to the emulated faults. This to obtain an objective and full view on the influence of the mechanical faults in the current spectrum. The used fitting method is the method of the least squares, which indicates the correlation with a specific model by calculating the coefficient of determination, usually referred to as r^2 . This factor represents a reference to compare a certain series of measurement points with the applied model. In this case, the series of values which are fitted are defined for each spectral frequency component as a function of the fault severity. The models used in the fitting algorithm are:

- first order polynomial (linear);
- second order polynomial (quadratic);
- third order polynomial (cubic);
- logarithmic function;
- exponential function.

However, the best fitting models will shown to be mainly first and second order polynomial functions. The experiments will show that these functions sufficiently approaches the observed variations. A spectral component is experimentally defined as dependent on the fault severity as the coefficient of determination is set

≥ 0.65 and the absolute proportional parameter is significantly high (further referred to as a , b or c), this to obtain a minimum correlation between the used model and the measurements points. However, the following experimental results will show that the coefficient of determination will in most case be higher then 0.65. Using *Matlab*[®], fitting a polynomial function on a vector is very convenient. If X is the vector consisting the discrete change in fault severity and Y_f is the vector consisting the observed magnitude of frequency component f as a function of X , expressed as:

$$Y_f = \begin{bmatrix} y_f(x_1) \\ y_f(x_2) \\ y_f(x_3) \\ \vdots \end{bmatrix} \quad \text{and} \quad X = \begin{bmatrix} x_1 \\ x_2 \\ x_3 \\ \vdots \end{bmatrix} \quad (6.1)$$

then the coefficients a , b and c of the fitted second order polynomial are determined to be:

$$Y_f = a \cdot X^2 + b \cdot X + c \quad (6.2)$$

$$[a \quad b \quad c] = \frac{Y_f}{[X^2 \quad X \quad 1]} \quad (6.3)$$

$$= \frac{\begin{bmatrix} y_f(x_1) \\ y_f(x_2) \\ y_f(x_3) \\ \vdots \end{bmatrix}}{\begin{bmatrix} x_1^2 & x_1 & 1 \\ x_2^2 & x_2 & 1 \\ x_3^2 & x_3 & 1 \\ \vdots & \vdots & \vdots \end{bmatrix}} \quad (6.4)$$

The coefficient of determination, r^2 , expressing how good the obtained model approaches the real trend is subsequently noted as:

$$r^2 = 1 - \frac{\sum_i (Y_f(i) - a \cdot X(i)^2 - b \cdot X(i) - c)^2}{\sum_i (Y_f(i) - \bar{Y}_f)^2} \quad (6.5)$$

where \bar{Y}_f is the mean value of the vector Y_f . Conclusively, the presentation of the fault related spectral components in the stator current will be the frequency components of which r^2 is found to be ≥ 0.65 and where the parameters a , b and c are significantly high. This methodology of determining the most valuable components after conducting an experiment will be applied in next sections. By doing this, the risk of overseeing valuable trends in the current spectrum is minimized. Even the smallest current component which varies under influence of the fault severity will be highlighted.

6.2 Misalignment

The origin and impact of misalignment regarding industrial IMs was extensively discussed in Chapter 4. Out of that chapter, it became clear that misalignment is comparable with an imposed static eccentricity. Due to an excessive radial load, the rotor is decentralized with respect to the stator. Consequently, misalignment is emulated as a time independent deviation of the rotor with respect to the stator. The severity of misalignment is thereby defined as the magnitude of the deviation, A_{mis} , §4.2.1. During the experiment, the rotor shaft is moved by the AMB in the horizontal direction from $-400\mu\text{m}$ to $+400\mu\text{m}$ with respect to the stator geometric center (static eccentricity). The vertical position of the rotor is kept steady at the horizontal centerline of the stator. The current is measured and analyzed every 10s per step of $5\mu\text{m}$. As discussed, those signals are demodulated by the EPVA and subsequently transformed to the frequency spectrum where all frequency components are analyzed as a function of the misalignment.

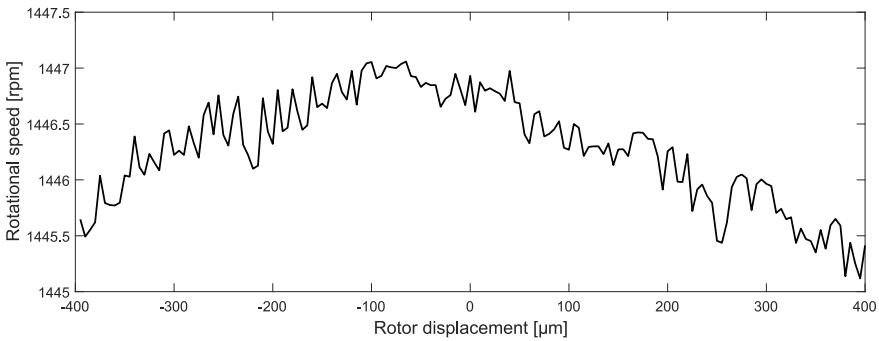


Figure 6.4: The variation in speed during the 160 experiments has to be taken into account in the fault component calculation

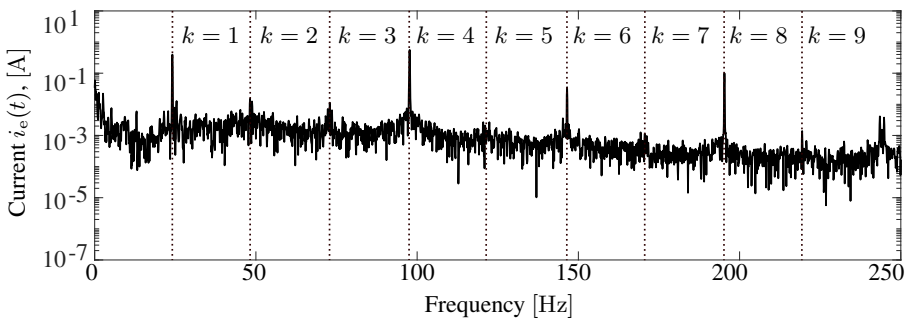


Figure 6.5: The $i_e(t)$ spectra during emulated misalignment where $A_{\text{mis}} = 400\mu\text{m}$ with the indicated fault related frequencies f_{eccm} (rotor mixed eccentricity)

The current spectral components of which a certain trend could be detected are plotted in Figure 6.6 and listed in Table 6.2. The first thing to notice is that the speed was determined to be 1445rpm . It is sometimes more interesting to express the frequencies in *orders*, which is a relative ratio with respect to the speed. This

is generally done for speed varying applications. Nevertheless, as in this experiment the speed is sufficiently constant, the absolute notation of frequency is used. The speed during the experiments is presented in Figure 6.4 by visualizing the first order component of rotor mixed eccentricity ($f_{\text{eccm}} = k \cdot f_r$, Table 3.5). This relatively small variation in speed of $\pm 2\text{rpm}$ or $\pm 0.033\text{Hz}$ is taken into account in the frequency fault component calculation for each step in severity. However, in this experiment, the effect of the $\pm 0.033\text{Hz}$ variation is negligible in the detection of eccentricity components. As can be observed in Figure 6.6 and as well in Table 6.2, the trending current components have an undeniable quadratic relation with the severity of misalignment, A_{mis} . Furthermore, the dominant components are exactly related to *Rotor Mixed Eccentricity* (coefficient of determination: $r^2 = 0.84$) and *Rotor Static Eccentricity* ($r^2 = 0.72$). It can be observed that although the rotor was symmetrically varying from $-400\mu\text{m}$ to $+400\mu\text{m}$, the quadratic reflection to the stator current is not exactly symmetric. This can be assigned to the remaining static eccentricity at the NDE bearing of the rotor with respect to the stator. Thereby, even when the rotor within the AMB is perfectly centered, there remains some residual misalignment at NDE-side. However, it can be concluded that a strong correlation can be observed between the misalignment and both static and mixed eccentricity. The estimated parameters of the quadratic functions listed in Table 6.2 provide a quantified relation between the severity of the emulated misalignment and the magnitude of the fault components in the stator current. Using these functions irreversibly, an estimation of the misalignment can be calculated by observing the low-frequency fault components related to static eccentricity and rotor mixed eccentricity. As the fault response for misalignment is noted to have an influence on rotor mixed eccentricity, which can be a fault component for other phenomena, the detection of the complementary static eccentricity indicating components is required to fully distinguish between misalignment and other phenomena e.g. mass-unbalance.

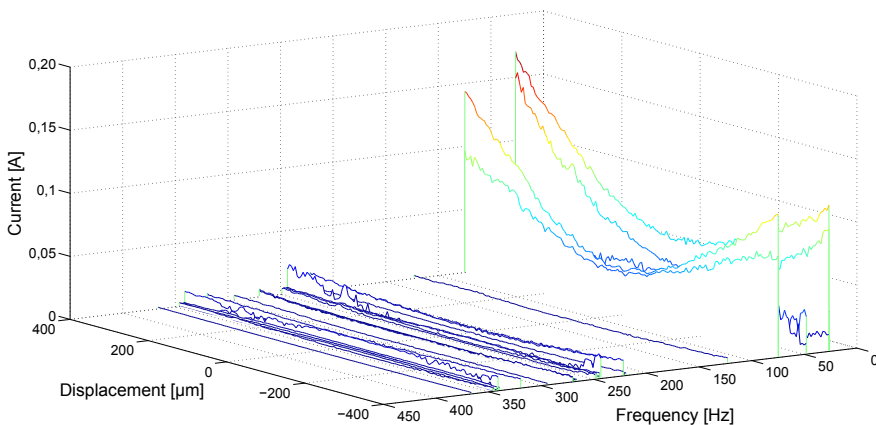


Figure 6.6: Varying frequency components in the EPVA vector during the emulation of misalignment/static eccentricity

Illustratively, the spectral analysis of the EPVA current $i_e(t)$ is presented in Figure 6.5 with highlighting the characteristic fault harmonics for mixed eccen-

tricity ($k \cdot f_{\text{eccm}}$). Note the difference of this spectrum with respect to Figure 6.6. Figure 6.6 shows only the fault dependent frequency components, as Figure 6.5 indicates all frequencies. Thereby the importance of finding trends in the stator spectrum is confirmed, as valuable components can easily be suppressed by noise or other components. However, the fault is by this analysis clearly distinguishable to other phenomena. This is mainly because the eccentric positioned rotor bars induce several fault indicating frequencies in the stator current equivalent to *rotor static eccentricity*. Regarding industrial applications, an evolving misalignment fault can easily be detected by trending the spectral current for several measurements. In practice, as misalignment generally does not evolve, the detection of an exceedingly high first order component of mixed eccentricity results in the evaluation of misalignment and rotor unbalance. The term 'exceedingly high' can be quantified based on these experiments. For example, the machine operator can be advised on realigning his rotational machine when the first order mixed eccentricity component in the current exceeds the trigger of 15mA ($\sim -60\text{dB}$ with respect to the fundamental current).

Frequency [Hz]	Indication	Order $k(n)$	$f(A_{\text{mis}}) = a \cdot A_{\text{mis}}^2 + b \cdot A_{\text{mis}} + c$			
			a x e-05	b x e-03	c x e-03	r^2
24.09	Mixed ecc.	1	0.1364	0.0328	5.4302	0.9971
48.18	Mixed ecc.	2	0.0582	-0.0682	2.1880	0.8255
72.27	Mixed ecc.	3	0.1224	0.0439	3.2389	0.9949
144.54	Mixed ecc.	6	0.0099	-0.0033	0.1461	0.7291
216.81	Mixed ecc.	9	0.0130	0.0008	0.4587	0.9641
240.90	Mixed ecc.	10	0.0342	-0.0479	1.7455	0.8761
264.99	Mixed ecc.	11	0.0024	-0.0009	0.0130	0.8579
313.17	Mixed ecc.	13	0.0008	-0.0003	0.0093	0.6332
328.81	Static ecc.	1(-13)	0.0450	-0.0495	1.2691	0.7305
337.86	Mixed ecc.	14	0.0049	-0.0008	0.0094	0.8176
361.35	Mixed ecc.	15	0.0015	-0.0004	0.0068	0.7995
426.47	Static ecc.	1(-11)	0.0002	-0.0740	0.0182	0.7631
524.13	Static ecc.	1(-9)	0.0484	-0.0521	1.2838	0.7370
621.79	Static ecc.	1(-7)	0.0002	-0.0006	0.0369	0.8215
817.11	Static ecc.	1(-3)	0.0231	-0.0255	0.6571	0.7252
914.77	Static ecc.	1(-1)	0.0834	-0.0883	2.1289	0.7178
1012.41	Static ecc.	1(1)	0.006	-0.0066	0.1687	0.7171
1101.91	Static ecc.	1(3)	0.0400	-0.0430	1.0587	0.7385
1207.85	Static ecc.	1(5)	0.0004	-0.0005	0.0155	0.7149
1403.19	Static ecc.	1(9)	0.0089	-0.0094	0.2281	0.7168

Table 6.2: Misalignment trending functions of the detected fault components in the EPVA vector

6.3 Rotor unbalance

Rotor unbalance or mass-unbalance was discussed in Chapter 4. Machine imperfections or material impurities cause an inevitable mass-unbalance in every rotor. This deviation of the geometric center of rotation and the gravitational center of rotor causes a rotating radial force on the bearings. The resulting movement of the rotor with respect to the stator was stated to be relatable to dynamic eccentricity. Consequently, mass-unbalance is hereby emulated by a predefined dynamic eccentricity. Formulas were constructed which calculated the movement as a function of the equivalent mass of the unbalance working on the DE bearing, m_{unb} , which can be interpreted as the severity of the working unbalance. Other parameters in that specific formula discussed in §4.2.2 are kept constant. These parameters are the radial location of the unbalance $r_{\text{unb}} = 100\text{mm}$, the bearing stiffness at DE side $k_r = 2.85 \cdot 10^5 \text{kN/mm}$ and the rotational speed $f_r = 24.09\text{Hz}$ or 1445rpm . This speed is on-line estimated out of the stator current and feed-back to the rotor movement calculation, as the dynamic eccentricity imposed by the unbalance is speed-depending. The mass is on-line adapted from 0kg to 1.6kg in steps of 10g . The maximum mass-unbalance in this experiment is based on the maximum rotor deviation in previous section, discussing misalignment, $\sim 400\mu\text{m}$. Similar to the experiment regarding misalignment, the current is measured and analyzed every step. The stator current frequency components transformed by the EPVA which have a clear relation with the mass-unbalance are visualized in Figure 6.7 and listed in Table 6.3. Again, only components which are actually influenced by the unbalance are plotted and included in the table. The full spectrum for the severest emulation ($m_{\text{unb}} = 1.6\text{kg}$) is included by Figure 6.8 with highlighted fault indicating frequency f_{eccm} (mixed eccentricity).

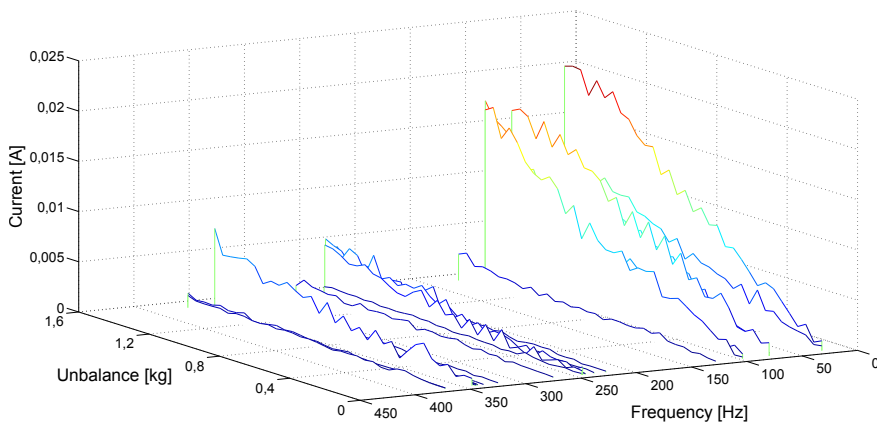


Figure 6.7: Varying frequency components in the EPVA vector during the emulation of mass-unbalance/dynamic eccentricity

An undeniable clear relation can be observed between the severity of the mass-unbalance, A_{unb} , and the current components, this time following a first order polynomial. The dominant fault components are related with *Rotor Mixed Eccentricity* ($r^2 = 0.91$) and *Rotor Dynamic Eccentricity* ($r^2 = 0.71$). The trending

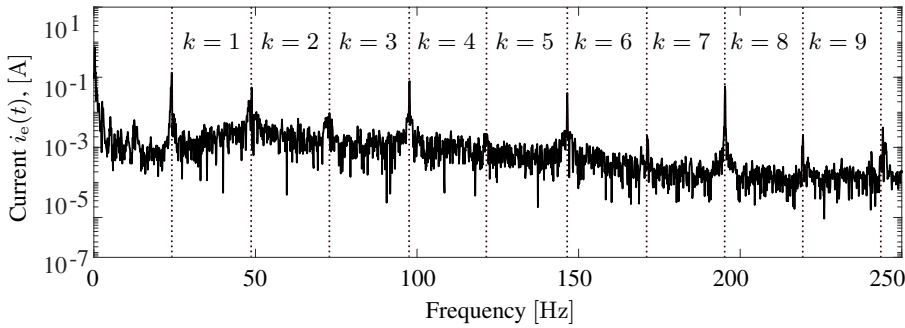


Figure 6.8: The $i_e(t)$ spectra during emulated unbalance where $m_{\text{unb}} = 1.6\text{kg}$ with the indicated fault related frequencies f_{eccm} (rotor mixed eccentricity)

frequency components confirm a clear and strong relation between both mixed and dynamic eccentricity and the emulated mass-unbalance. It is noticeable that the trending fault components in the current indicate a comparable magnitude for both misalignment and unbalance for the same absolute deviation ($\sim 20\text{mA}$ for $\sim 400\mu\text{m}$). Although, the shape of the trending function is quite counter-intuitive. Misalignment -a static deviation- follows a second order polynomial, while mass-unbalance -a dynamic deviation- follows a first order trend. This effect is probably due to the combination of rotor-velocity and -displacement which is propagated to the stator current in case of mass-unbalance. Additionally, the UMP is interacting differently with the rotor when it is statically or dynamically deviated with respect to the stator geometric center. However, the listed parameters of the linear functions in Table 6.3 can be used to estimate a certain degree of severity out of the current components. Similar to misalignment, in the detection or identification of mass-unbalance, the combination of rotor mixed eccentricity and dynamic eccentricity is opportune to fully differentiate mass-unbalance from other faults. Additionally, if other rotational speeds are applicable, the fault components related to mass-unbalance will vary quadratically (see Chapter 2). This can be used as an additional way to link the detected fault components and their origin.

In order to visualize the rotor movement with respect to the stator due to the severest unbalance of 1.6kg , the demodulated current $i_e(t)$ (EPVA) can be spatially presented by plotting the direct and quadrature components $i_d(t)$ and $i_q(t)$ as it was presented in (3.6). These two components are presented in Figure 6.9, resulting in a circular shape. Comprehensibly, as the components are in the demodulated shape corresponding to the variation of inductance; reluctance; air gap; and consequently rotor movement. As the circular rotor movement due to the mass-unbalance coincides with the circular behavior of the EPVA vectors, a proportional expression can be obtained between induced currents and the rotor deviation. Out of Figure 6.9 and Figure 6.7, it is concluded that the deviation relates linearly to the current as $\sim 62.54\text{mA/mm}$ or, in terms of the emulated unbalance: 15.71mA/kg (25.14mA for 1.6kg). Generally, mass-unbalance is expressed as g-mm , [5], including the influence of the radial distance from the center to the mass. This results in defining the relation between mass-unbalance and the stator current EPVA as: $0.157\mu\text{A/g-mm}$. Applying this proportional factor, the mass-unbalance can be es-

Frequency [Hz]	Indication	Order $k(n; m)$	$f(A_{\text{unb}}) = a \cdot A_{\text{unb}} + b$		
			a x e-05	b x e-05	r^2
24.09	Mixed ecc.	1	6.6826	-5.6466	0.9872
48.19	Mixed ecc.	2	3.1586	-4.8931	0.9728
72.28	Mixed ecc.	3	4.9495	-2.9889	0.9913
97.05	Mixed ecc.	4	4.9764	-15.9334	0.9407
121.35	Mixed ecc.	5	0.6504	-0.0458	0.8284
220.04	Mixed ecc.	9	0.4996	-0.3491	0.8604
231.36	Static ecc.	1(-15)	1.3934	-7.8003	0.8192
235.19	Dynamic ecc.	1(-9; -12)	0.7389	-1.0374	0.8525
240.95	Mixed ecc.	10	1.4596	-0.5474	0.8734
265.05	Mixed ecc.	11	0.4522	-0.1187	0.8527
332.85	Dynamic ecc.	1(-9; -8)	0.1348	0.1158	0.7767
361.43	Mixed ecc.	15	0.3779	-0.1580	0.9071
840.90	Dynamic ecc.	1(-1; -3)	0.1347	-1.0194	0.6415
962.50	Dynamic ecc.	1(-1; 2)	0.1502	-1.1670	0.5599
988.88	Dynamic ecc.	1(1; -1)	0.0709	-0.4179	0.6229
1037.09	Dynamic ecc.	1(1; 1)	0.2313	-1.8054	0.6699
1061.21	Dynamic ecc.	1(1; 2)	0.1708	-1.2089	0.7345
1205.83	Dynamic ecc.	1(1; 8)	1.1044	-6.2791	0.8230
1403.61	Static ecc.	1(9)	0.3354	-1,9111	0.7678

Table 6.3: Unbalance trending functions of the detected fault components in the EPVA vector

timate out of the magnitude of the direct and quadratic current component. Further research could be conducted to express this ratio for other sizes of IMs. For example, as it is done in the ISO vibration standards, an expression could be obtained for mass-unbalance as a function of the kilogram rotor. For this example, the ratio would be $2.83\mu\text{A}/\text{g}\cdot\text{mm}/\text{kg}$ (rotor of 18kg). In other words, 1kg rotor with an unbalance of 1g at a radius of 1mm induces a frequency component of $2.83\mu\text{A}$ in the EPVA vector at rotational speed. This should however be confirmed by measurements of unbalance on other sizes of IMs, which will be discussed in future work (see Chapter 7). Using that standard *ISO 21940-11:2016* for mass-unbalance in rigid motors, it is indicated that the maximum residual unbalance in the 11kW induction machine under test is 13.6g on 100mm radius. This implies that the unbalance in the 11kg exceeds the ISO standard for normal operation if the mixed eccentricity fault component detectable in the stator current exceeds $213\mu\text{A}$.

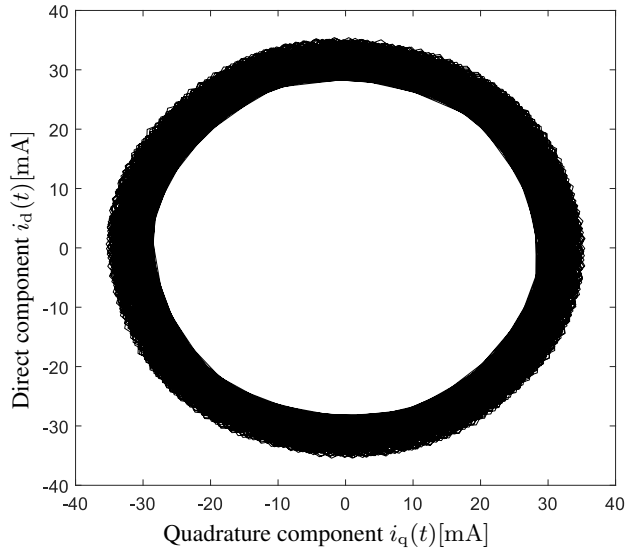


Figure 6.9: The circular rotor movement visible in the direct and quadrature component $i_d(t)$ and $i_q(t)$

6.4 Bearing faults

Bearing faults, the most common direct and indirect cause of failure, are essential to be detected by any condition monitoring technology. They are nevertheless the most complex in behavior and in prediction of development. The way they impact IMs by imposing specific rotor movements was extensively discussed in Chapter 4. The obtained analytical model is able to calculate all kinds of bearing problems with all kinds of conditions e.g. fault severity, bearing properties or operational settings, discussed in Chapter 5. These dynamic movements were used to dimension the AMB and its control loop. As it is sufficiently clear how these faults interact with the stator current, discussed in Chapter 2, the investigation on the relation between the severity of bearing faults and their reflection in the stator current can be conducted. Three main experiments are conducted. One regarding single point outer race bearing pitting, one for single point inner race bearing pitting and one regarding bearing cage problems. All experiments are intended to elucidate the relation between the fault severity of the three mechanical faults and the varying spectral reflection in the EPVA signal $i_e(t)$. In order to do so, the IM under test is operating in a stable operational condition (temperature, speed, torque). Although it is of major importance that the influence of load on the reflection in the stator current is investigated, this could not yet be included in this research due to some limitations of the real-time controller. All focus was on the dependency of fault severity and the corresponding fault signatures in the stator current as this remains the missing link in the MCSA-related literature. However, in following experiments, the load is held constant as it was in previous experiments in order to quantify the reflections of evolving bearing faults in the spectral stator current.

6.4.1 Single point outer race bearing faults

An increasing severity of an incipient single point outer race bearing pit is an increase in length of that pit. As the bearing balls are flying over the pit with a significant speed, the bearing balls rarely touch the actual bottom of the pit. They collide, as discussed in Chapter 4, with the end surface of the bearing pit. This results in an increase of pit length as the bearing pit evolves instead of an increase in pit depth [39, 49]. Consequently, in order to emulate a change in severity of the single point outer bearing faults, the parameter l_{pit} is adapted from 0mm till 2.5mm in steps of 10 μm . When more severe bearing fault would be emulated, not only the pit length, but as well the pit depth should be increased. Comprehensibly, as the bearing balls repetitively touch the bottom of the pit in case of longer pits. In order to visualize the effect of an evolving single point pit on the absolute movements of the rotor with respect to the stator, Figure 6.10 is constructed by simulations by using the formulas obtained in §4.3. In that figure, the maximum displacement of the rotor with respect to the stator is presented as a function of both the pit depth and pit length. The analysis elucidates the influence and impact of both the depth and length of the pit on the rotor movements. The depth of the pit plays an important role when the pit is sufficiently long. This because for long pits, the falling bearing ball collides with the bottom of the pit. From that point on, when the pit length further increases, it does not influence the movement of

the rotor in magnitude anymore. This because the force needed to restore the bearing ball in the circular track remains equal. Additionally, the pit depth does not have any influence on the movements for short pits, because the bearing ball does not have time to reach the bottom surface of the single point bearing pit. However, in this emulation, the pit length is adapted as this is how incipient bearing pitting evolves (short pits) [39, 49]. During emulation, the stator current is similar to previous experiments monitored 10s in stabilized condition for every adaption in severity. By repetitively recalculating the rotor movements $y(t)$ and $x(t)$ and subsequently updating the AMB controller, the evolving fault is imposed on the operating IM on-line.

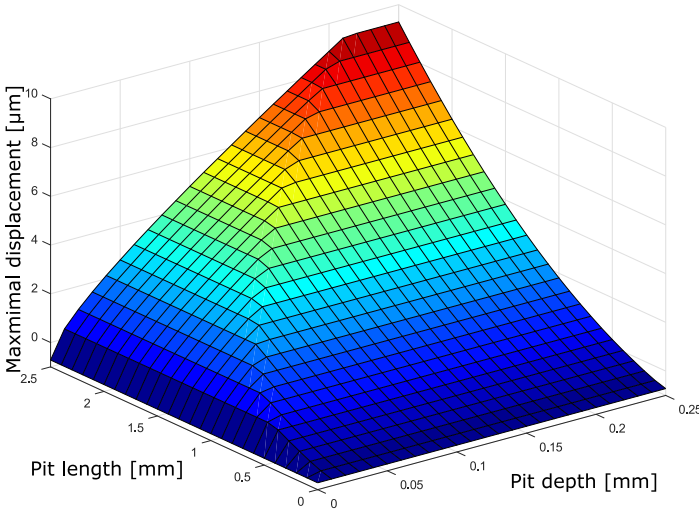


Figure 6.10: Maximum rotor displacement for a single point bearing outer race fault under varying pit depth and pit length obtained by simulations

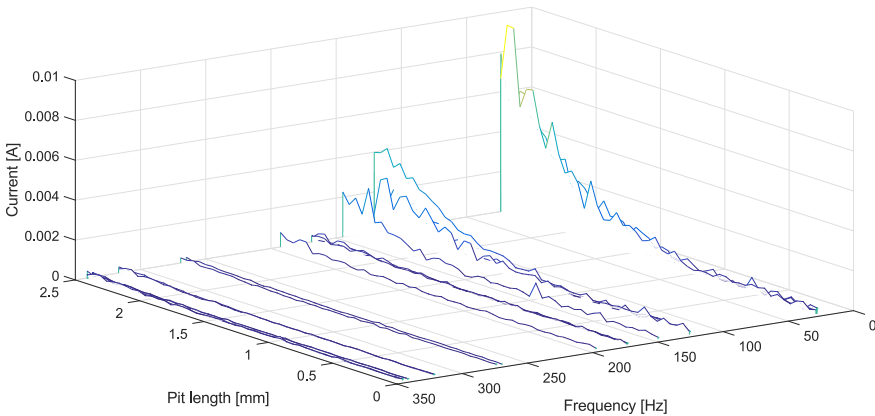


Figure 6.11: Varying frequency components in the EPVA vector during the emulation of evolving single point outer race bearing pitting

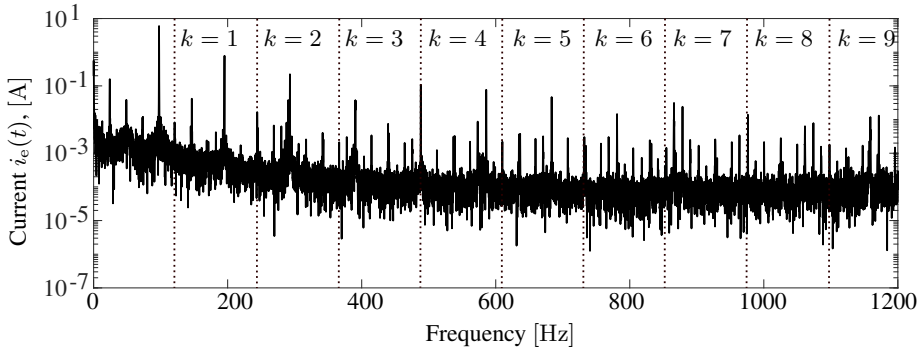


Figure 6.12: Spectral EPVA vector $i_e(t)$ for an outer race bearing fault emulation where $l_{\text{pit}} = 2.5\text{mm}$

The results of the experiments are shown via the trending spectral components in the EPVA vector $i_e(t)$ in Figure 6.11 and listed in Table 6.4. Not surprisingly, but yet remarkable that the trending fault components undoubtedly indicate the outer race bearing fault (formula in (3.8), Chapter 3). A very clear, quantifiable relation is confirmed between the severity of the outer race bearing fault and its reflection in the stator current EPVA vector. Furthermore, the relation can be defined following a second order polynomial function. These defined functions are listed in Table 6.4. In that table, the coefficient of determination, r^2 , is in average equal to ~ 0.7 . Furthermore, the first order outer race fault indicator at 119.55 is related to the pit length with $r^2 = 0.9018$. Although the emulated fault is really premature, a very clear signature is introduced in the current spectrum. However, the very beginning of the fault is hard to differentiate between the noise of the captured signal, not very different to other CM technologies. As the first order component of the outer race signature in the current is very dominant and does not indicate any other type of fault, the second order polynomial function can be used to identify the fault and estimate its severity. This is not the case for previously discussed misalignment and unbalance, where these faults partially influence the same fault components (e.g. mixed eccentricity). Although, as can be noticed in Table 6.4, the outer race fault components are accompanied with signatures of inner race and cage faults. This is in fact very common, especially regarding severe bearing faults [2, 49]. However, in this case, by linking the spectral content with the characteristic bearing frequencies, it becomes clear that the signature in the current concerns an outer race bearing problem (Table 6.4). It is additionally remarkable that an emulated incipient bearing fault of only 2.5mm induces a spectral current component up to 10mA. The advantage in detecting/analyzing bearing fault is that the induced signatures are all very unique in frequency value. This avoids confusion in detection/analysis due to merged frequency components or to the possibility of several diagnosis. As soon as several bearing related components are visible in the current spectrum, it can be stated with high certainty that there is in fact an evolving bearing problem. In completion, Figure 6.12 is included presenting the visualized outer race fault indicating EPVA vector spectral components in the final stage ($l_{\text{pit}} = 2.5\text{mm}$) with highlighted harmonics of the characteristic outer race bearing frequency ($k \cdot f_{\text{BPFO}}$).

[Hz]	Indication	k	$f(l_{\text{pit}}) = a \cdot l_{\text{pit}}^2 + b \cdot l_{\text{pit}} + c$			
			a x e-07	b x e-05	c x e-05	r^2
24.08	Mixed ecc.	1	17.8122	-4.7870	33.7553	0.9341
119.55	Outer race	1	6.5168	-1.6216	18.1236	0.9018
144.15	Ball spin	3	5.2905	-1.8411	22.9265	0.7899
168.51	Mixed ecc.	7	1.1481	-0.3372	4.6839	0.6687
192.19	Ball spin	4	0.3781	-0.2869	8.3849	0.6063
288.30	Ball spin	6	0.4049	-0.1752	2.6483	0.7411
336.35	Ball spin	7	0.1987	-0.1487	3.5154	0.7166
358.41	Outer race	3	1.8759	-0.2205	4.0893	0.6436
478.21	Outer race	4	0.2416	-0.2084	4.7921	0.7070
580.42	Inner race	3	-0.1245	0.0835	5.9220	0.6974
717.32	Outer race	6	0.7330	-0.6206	13.1592	0.7315
836.27	Outer race	7	0.1187	-0.0567	1.7853	0.6862
955.74	Outer race	8	0.0487	-0.0342	1.0892	0.7483

Table 6.4: Trending functions of the spectral outer race fault components in the EPVA vector

6.4.2 Single point inner race bearing faults

The characterization of these types of faults is very similar to outer race bearing pitting. Thereby, the emulation is conducted with the same principles and under the same conditions. The pit is increased in length from 0mm to 2.5mm in order to adapt the fault severity. Again, the current is logged for 10s and subsequently transformed by the EPVA in every stabilized emulation. The trending components in the spectrum of $i_e(t)$ are presented in Figure 6.13 and listed in Table 6.5. As can be observed, the bearing fault is detected and identified without any doubt. However, the signature is way less pronounced in the spectrum as it is for outer race faults. Not only in magnitude, but as well in present fault components in the spectral EPVA vector. This is mainly because the fault component is rotating in the machine, which implies that the periodic impact according to f_{in} (formula in (3.9), Chapter 3) is significantly less present in magnitude. The impacts are less frequent and energetic than they are in case of outer race bearing faults. The rotational phenomena is as well noticeable due to the sidebands around the first two harmonics of the inner race fault component: 193.78Hz and 387.56Hz. This confirms the mathematical magnitude modulation of the periodic inner race impact with the rotational speed and the Fundamental Train Frequency (FTF), (4.32), corresponding to the rotational speed of the bearing cage. However, the effect of the sidebands around the characteristic inner race bearing frequency is less pronounced in the

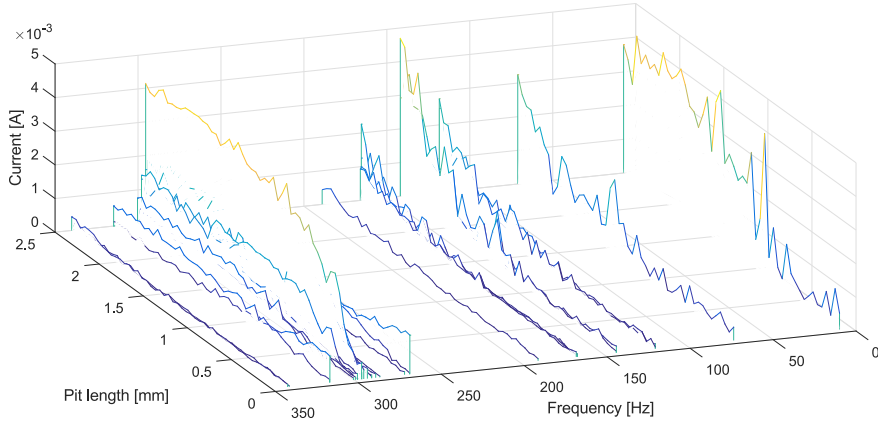


Figure 6.13: Varying frequency components in the EPVA vector during the emulation of evolving single point inner race bearing pitting

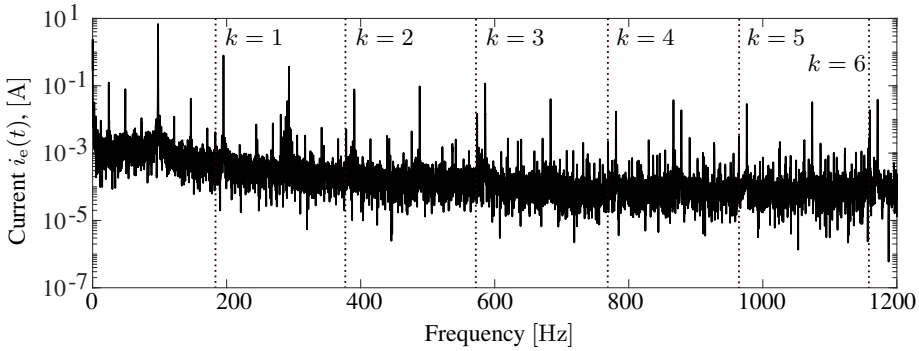


Figure 6.14: Spectral EPVA vector for an inner race bearing fault emulation where $l_{\text{pit}} = 2.5\text{mm}$

current then it is in vibration analysis. This is partially due to the demodulation transform by the EPVA. Additionally, it can be seen that around $\sim 300\text{Hz}$, some dynamic eccentricity is detectable as well. This confirms the significance of the effect of the rotating inner race bearing pit on the rotor. Similar to outer race signatures, the other bearing related forcing frequencies are present in the spectrum as well (outer, cage and ball spin). Conclusively, inner race bearing faults are less explicit and thereby more difficult to detect with respect to outer race faults. This mainly due to the modulation between the inner race fault frequency with the rotational and cage speed. Nevertheless, these interacting phenomena ensures the identification of the detected bearing fault. Nevertheless, these incipient inner race bearing faults were detected by the current analysis. Using the first and second order inner race polynomial functions, an estimation can be made on the severity of the detected inner race bearing fault. Due to the lower certainty (average $r^2 \sim 0.65$), the severity estimation will be less accurate compared to the predictions for outer race bearing faults. Supplementary, the periodic inner race fault frequency detectable in the EPVA vector is highlighted in Figure 6.14 for the fi-

[Hz]	Indication	$k(n; m)$	$f(l_{\text{pit}}) = a \cdot l_{\text{pit}}^2 + b \cdot l_{\text{pit}} + c$			
			a x e−07	b x e−05	c x e−05	r^2
9.20	Cage defect	1	2.1580	−3.1244	19.7649	0.6713
72.33	Mixed ecc.	3	2.4040	−6.6258	11.4871	0.5912
119.69	Outer race	1	1.6347	−0.3471	7.4485	0.6201
144.37	Ball spin	3	2.9669	−0.8051	5.1960	0.7790
193.78	Inner race	1	0.3805	−0.1334	1.2934	0.7047
288.75	Ball spin	6	1.8625	−3.3744	8.7177	0.6345
301.85	Dynamic ecc.	1(−9; −9)	1.9416	−4.5892	2.4634	0.6951
336.87	Ball spin	7	0.2900	−0.1684	2.4822	0.7016
387.55	Inner race	2	0.2964	−0.3888	12.4677	0.6648
576.48	Ball spin	12	0.3258	−0.4480	15.4107	0.6007
580.31	Inner race	3	0.2693	−0.4206	16.9402	0.7523
597.22	Outer race	5	0.1330	−0.1790	6.2729	0.6591
672.56	Ball spin	14	0.2664	−0.3569	11.4832	0.6364
773.74	Inner race	4	0.2236	−0.2985	9.6924	0.6405
967.18	Inner race	5	0.6465	−0.8737	27.7185	0.6561
1075.00	Outer race	9	0.7392	−1.0094	32.3092	0.6894
1160.61	Inner race	6	4.3375	−5.9518	188.6236	0.6273

Table 6.5: Trending functions of the spectral inner race fault components in the EPVA vector; $i_e(t)$

nal severity stage ($l_{\text{pit}} = 2.5\text{mm}$) with highlighted harmonics of the characteristic inner race bearing frequency ($k \cdot f_{\text{BPF1}}$).

6.4.3 Bearing cage faults

Regarding bearing cage problems, the same methodology as before is applied. Only the increase in fault severity is done by adapting the magnitude A_{cage} from $0\mu\text{m}$ till $130\mu\text{m}$ in steps of $1\mu\text{m}$. This deviation represents an induced dynamic eccentricity at the Fundamental Train Frequency (FTF). Table 6.6 presents the varying spectral components of the EPVA signal i_e . The trending fault components are complementary presented in Figure 6.15.

The detected fault frequencies are significantly lower in frequency than the other emulated bearing faults due to harmonics of the characteristic cage fault frequency (related to the FTF, formula in (3.11), Chapter 3). The trend is far more accurate in terms of coefficient of determination, which is on average ~ 0.9 . A

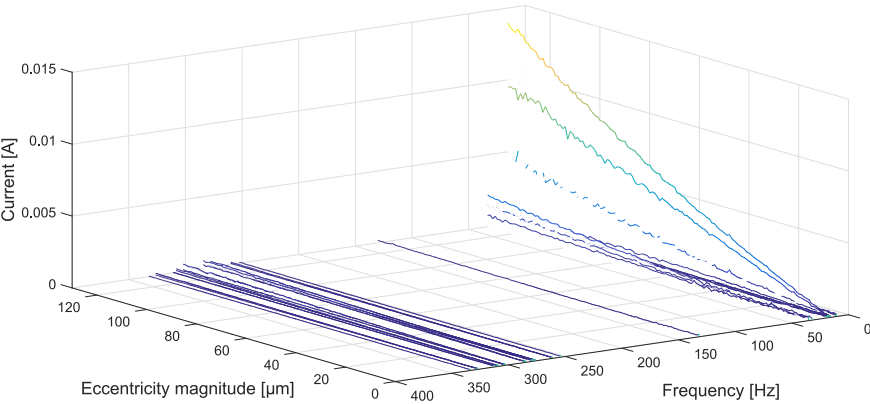


Figure 6.15: Varying frequency components in the EPVA vector during the emulation of an evolving bearing cage fault

[Hz]	Indication	k	$f(A_{\text{cage}}) = a \cdot A_{\text{cage}} + b$		
			a x e-05	b x e-05	r^2
9.19	Cage defect	1	2.5511	-24.7563	0.9637
18.40	Cage defect	2	5.1242	-9.2723	0.8805
27.60	Cage defect	3	0.9745	-7.4428	0.8973
36.79	Cage defect	4	1.4312	-1.5924	0.9603
128.78	Cage defect	14	0.1349	-0.0441	0.8799
288.59	Ball spin	6	0.3658	-0.8002	0.8408
336.69	Ball spin	7	0.0759	0.2492	0.6211

Table 6.6: Trending functions of the spectral cage defect fault components in $i_e(t)$

very clear and strong first order linear relation is observed between the faulty cage frequency and the reflection in the stator current EPVA vector. This trend is quite similar to the emulation of mass-unbalance, as it is in essence a dynamic eccentricity as well. Due to the inherent properties of using current instead of vibration, these types of faults (low-frequency and force, large displacement) are in fact detectable in a premature stage. As for vibration analysis the cage fault is hardly visible, current analysis has a firm trend with the dynamic eccentricity around the FTF, the speed of the rotating cage. However, a cage fault rarely occurs without any cause of damage by the outer or inner race with the exception of a fundamental dimensioning error. Consequently, the detection of cage fault frequency is mostly accompanied with the presence of either inner or outer race bearing fault signatures. Nevertheless, when a pure cage fault occurs, it can easily be detected and quantified in terms of severity.

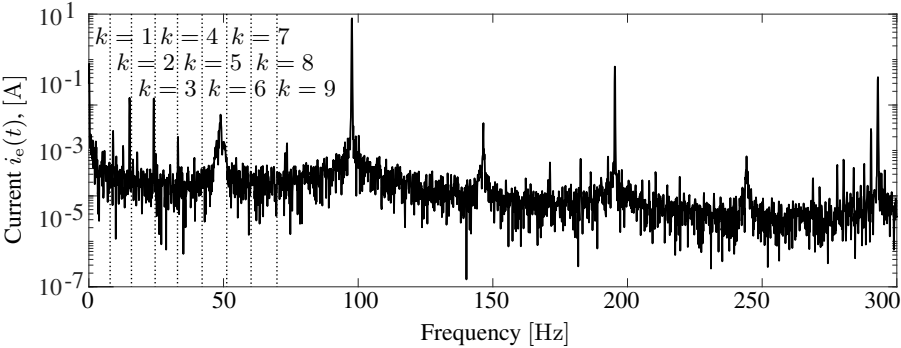


Figure 6.16: Spectral EPVA vector for a bearing cage fault emulation where $A_{\text{cage}} = 150\mu\text{m}$

6.5 Conclusion

The test-rig dimensioned in previous chapter showed its valuable functionalities throughout this chapter. Different mechanical faults were emulated with high accuracy and reproducibility with the focus on fault severity quantification. This was confirmed by repetitively re-conducting experiments resulting in the same, minor differing results. Firstly, misalignment was emulated in which the rotor center was statically deviated with respect to the stator. This static eccentricity was easily detected in the stator current on two fault indicating components: mixed and static eccentricity. A clear relation is now quantified between the fault severity and the current EPVA components following a second order polynomial equation. As second experiment, mass-unbalance was emulated in the IM under test. These responses in the current were linked to dynamic and mixed eccentricity. Due to the clear first order linear trend, a factor is defined which actually links the real mass-unbalance with the magnitudes of the present fault components. Additionally, the shape of the rotor movement was reconstructed by the demodulated direct and quadrature current component. Thirdly, regarding bearing faults, every emulated type of fault had a strong relation with the corresponding fault indicators in the EPVA signal. The single point outer race emulation resulted in the dominant presence of the characteristic outer race bearing fault current component. A quadratic relation is observed between the fault severity, more specific the length l_{pit} , and the harmonics of the outer race fault components. The relatively small coefficients of a with respect to b indicates that the dependency is linear for small values of l_{pit} and is quadratic for large values. This can be interpreted that for immature faults, a change in severity affects the stator current moderately, while severe faults have a strong impact on the current fault reflections. A similar behavior is noted regarding the single point inner race fault emulation. The inner race fault components are dominant and experience a quadratic change when fault severity is increased. Although, the reflection in the stator current is less explicit for inner race bearing faults due to the bearing pit is rotating, the characteristic fault frequency component f_{in} is modulated in magnitude with f_r . Considering Figures 6.12 and 6.14, it is observed that during severe single point bearing faults the three types of characteristic fault frequencies can be spotted. For example, inner race fault indicating components are present in the spectrum for the outer race fault emulation and vice versa. Nevertheless, only the characteristic components of the corresponding bearing fault show a clear and strong correlation to the fault severity noticed by the coefficient of determination, r^2 . Regarding the bearing cage defect emulation, the current components are subjected to a first order linear trend with respect to the increased magnitude. This is due to linear dependency of the magnitude of the rotor deviation with the emulated fault severity.

Lastly, it must be noted that for every type of emulated fault, even when the fault is immature, the fault components are clearly detectable in the current EPVA vector. Furthermore, the severity of each fault was easily quantified with a relatively high accuracy ($r^2 \geq 0.65$). Due to these conducted experiments, the fault indicating spectral components in the EPVA vector can distinctively be linked with evolving mechanical faults of several origins, complemented with a satisfying severity estimation. Regarding bearing faults, although inner, outer and cage

Power size [kW]	Dominant fault component			Fault severity (pit length)	
	[Hz]	[mA]	Fault	Estimated [mm]	Real [mm]
15	120.23	23.16	Outer race	3	~ 4
250	119.55	48.85	Outer race	2	~ 4
500	87.14	134.55	Outer race	12	~ 9
980	91.89	185.13	Inner race	15	~ 17

Table 6.7: Comparing the emulation results with real bearing fault test cases (all IMs)

faults can be distinguished through spectral analysis, they generally occur simultaneously in real industrial applications. Nevertheless, this increases the possibility of detection in a premature stage. The added value of determining the exact location of the fault compared to the detection on component level could be questioned as the damaged bearing is commonly replaced completely. The machines operator should be satisfied with the knowledge of which bearing is damaged and the corresponding severity estimation. During this research, several industrial cases were conducted with the focus on confirming and validating these experiments on signature and severity estimation. Although far more research is needed on the exact translation of the quantified relations to other power sizes of IMs (see §7.2), Table 6.7 is included presenting a condensed result of the dominant fault related component in the stator current for industrial cases severing bearing problems conducted during this research as service to the industry. All these are complemented with an estimated fault severity. These results conclude firstly that the detected signatures of the test rig emulations are exactly related to the real evolving bearing fault of any kind. Secondly, the analysis on severity estimation is preliminary able to approximately obtain the real fault severity in terms of size of the faulty pitting. It must be noted that the *real* pit length was quite inaccurately determined by measuring on the biggest pit of several bearing pitting (some from pictures). However, as this severity estimation for other power sizes is only based on the re-scaled ratio of fault component with respect to the fundamental RMS value, the potential of this algorithm is confirmed and can be significantly improved and optimized in future research.

7

Conclusions and future work

7.1 Overall conclusions

This dissertation was fully focused on applying stator current analysis as a complete and reliable condition monitoring technology. As this way of performing condition monitoring does have in essence several advantages with respect to the nowadays commercially applied systems, this research gains a lot of interest by the current world-wide market players in predictive maintenance strategies. It was extensively shown by the conducted literature study and industrial experiments that measuring stator currents can easily increase the reliability and flexibility in performing the monitoring for a wide variety of applications. Key-properties were the rather low costs, the robustness of the sensors, no need of access to the machine, perfect for harsh environments, the ability of detecting both mechanical and electrical faults. . . By performing an in depth market study, it became rapidly clear what the issues of the commercially available current based systems are: a proper severity estimation as soon as a specific mechanical fault is detected. This is thereby the main reason why this technology does not breach into the market of condition monitoring, the machine operator needs this information in order to plan the appropriate action. The lack of this severity estimation is understandable as these complex reflections of mechanical faults in the stator current are subjected to numerous influences and conditions e.g. machine torque, rotational speed, stator temperature, power quality. . . However, this limitation has to be overcome before MCSA can be applied as a full and reliable condition monitoring technology. As a consequence, the quantification between the severity of the most common mechanical faults and their reflections in the stator current was the main goal of this dissertation. In order to obtain this ambitious goal, three main scientific challenges were handled leading to three main contributions to the field of CM with MCSA:

- The establishment of an analytical model which is able to obtain all kinds of

rotor movements induced by several mechanical faults.

- The development of an experimental test-rig where the most common mechanical faults can accessibly be emulated with the focus on high accuracy and reproducibility.
- The quantification of the fault related reflections in the stator current with respect to the severity of the most common mechanical faults.

The overall goal, building the experimental test-rig, is completed with success. The novel and unique idea of replacing the mechanical drive end bearing of an 11kW induction machine enabled various possibilities. At one hand, the functionalities of the mechanical bearing were transferred by optimizing and adopting its main system properties to the magnetic bearing control loop. This resulted in the magnetic bearing behaving exactly as the mechanical bearing, without influencing or interacting the induction machine normal behavior. On the other hand, the magnetic bearing and its control loop are dimensioned as such that the high-dynamic required rotor movements corresponding to mechanical faults could be regenerated with high accuracy and reproducibility. As an advanced analytical model was established in order to calculate these exact rotor movements of the main mechanical faults based on their severity, bearing parameters, speed, coupling properties... they can be fed and adapted as set-points to the magnetic bearing on-line. Measurements concluded the obtained reproducibility and flexibility of the test-rig extensively. Numerous experiments on mechanical faults (misalignment, mass-unbalance and bearing faults) and their reflection in the stator current were emulated in a very accessible way. This leads us to the third main contribution, the identifications and quantification of the imposed mechanical faults through the stator current. For misalignment, mass-unbalance, single point outer race, single point inner race and cage faults, experiments were conducted on the impact of an increase in fault severity on their corresponding signatures in the stator current. Each fault clearly imposed very quantifiable reflections on the exact frequency components described in literature, resulting in the construction of a database of polynomials describing these reflections for the 11kW induction machine. Although lots of research has to be conducted on the effect of load variations and the translation of these findings on other sizes of induction machines and other types of electrical machines, these quantifications are applicable in order to estimate the severity of mechanical faults as soon as they are detected in the stator current. Preliminary test cases resulted in the ability of translating the found quantifications on other machine sizes by rationally expressing the fault signatures to the fundamental current component. However, this simplification is quite short-sighted and required far more attention in order to be validated. Nevertheless, these characterizations during this presented research on the relation between mechanical fault severity of different origin and the stator current placed MCSA a major step closer in the practical application as a complete and reliable condition monitoring technology.

7.2 Future Research

Today, the author sees two main scientific challenges that should be overcome before MCSA is actually ready for industrial valorization:

- The influence of torque and speed variations on the quantified relation between mechanical faults and the stator current should be elucidated thoroughly.
- The found quantifications between fault severity and the corresponding stator current signatures must be translated to other sizes of induction machines and to other types of electric rotating machines (synchronous machines, DC machines, SRMs...).

Regarding vibration analysis, it is commonly known that variations in speed and/or torque heavily disturb the spectral analysis and thereby the effectiveness of the condition monitoring system. This is because the magnitudes of the frequency components in the vibration signal are undefinably linked with the operational conditions as it is very dependent on the machine mounting and structure. Usually, it is dealt with this limitation by categorizing some explicit operational ranges where only spectra on that specific rotational speed and/or torque are compared with each other. Consequently, the system reliability is decreased as at least two measurements should take place under the same operational conditions in order to evaluate the fault evolution for that specific day. Additionally, regarding very high dynamic applications which have a critical role in a certain production process, this method is determined to be insufficient. As both torque and speed do have a clear, uniform and predefined impact on the stator current, the ability is created where the influence of the operational condition on the fault transmission from rotor to stator can be evaluated. These kind of tests were planned to be conducted throughout this research as they can easily be performed by using the novel test-rig. However, the real-time controller is currently not fast enough to computationally compensate the UMP and additionally impose the fault related rotor movements with sufficient accuracy and reproducibility. Nevertheless, replacing the real-time controller with a more powerful one (shorter cycle time) will inevitably result in the ability of conducting these experiments on the impact of operational changes on the reflections of mechanical faults in the current spectrum.

The second challenge is the translation of the obtained results to other machines with different sizes and different topologies. As the obtained quantifications between the severity of mechanical faults and their impact on the current spectra are now only obtained for the 11kW induction machine under test, the translation to other sizes and types of electrical rotating machinery is crucial in the industrial relevance. With the use of both finite element analysis and captured data of industrial test cases, the obtained quantification can be translated and validated with the focus on other machine sizes. On this day, in the scope of a subsequent research/valorisation-project, several test-setups are spread in the Flemish industry which are capturing voltage, current and vibration data from several induction machines with different power-size. With the use of the vibration signals of the stator housing, the rotor movements can be obtained analytically as was presented in §4.4.2. As every machine rotor is subjected to several forcing frequencies such as

unbalance, misalignment, fans, blades of compressors. . . the rotor is always moving with respect to the stator on several specific frequencies. Subsequently, the corresponding reflections in the stator current can be analyzed in magnitude after performing the EPVA. Consequently, for several frequencies throughout the spectrum, the response between rotor vibration and current can be quantified by a linear factor. By recreating these obtained movements from industrial cases with the novel mechanical fault emulating test-rig, as well the impact of those movements on the stator current for the 11kW machine can be stated. As then a rescaling of the response function between rotor vibration and stator current can be extracted for several sizes of induction machines, the real reflection of mechanical faults for several power-sizes can be artificially constructed. Additionally, and preferably mainly, the occurrence of a real evolving mechanical fault in one of the industrial cases will immediately result in the translation of the findings in this thesis for that specific size of induction machine. However, as this chance of occurrence is rather small, these validating experiments will as well be conducted using FEA software. By virtually creating rotor dynamic eccentricity on different machine sizes for a wide frequency range, the linear response functions between vibration and current can be obtained. Complementary to the experimental test cases, these results will as well enable the translation of the severity quantifications of the 11kW induction machine to other machine sizes. All of this in order to find a certain dependency of these obtained response functions with some machine size parameters (rotor diameter, air gap length, power size, nominal current. . .). This can result in the ability of uniforming the response functions and thereby the severity quantifications from this thesis on every size of induction machine. Regarding translating the findings in this research to other types of electrical machines, the approach would be the same. By combining both FEA and industrial cases, response functions for several types of machines can be obtained. However, the success of this research goal is of less importance as at least 90% of the installed electric rotating machines which are fulfilling a critical role are induction machines.

8

Bibliography

- [1] Electrical Apparatus Service Association. *Root Cause Failure Analysis*. EASA, The Electro Mechanical Authority, 2004.
- [2] Bram Corne, Bram Vervisch, Colin Debruyne, Jos Knockaert, and Jan Desmet. *Comparing MCSA with Vibration Analysis in order to detect Bearing Faults - A Case Study*. IEEE International Electrical Machines and Drives Conference (IEMDC 2015), pages 1366–1372, 2015.
- [3] R. B. Randall. *Frequency analysis*. Brüel and Kjaer, 1987.
- [4] Fusheng Zhang, Zhongxing Geng, and Wei Yuan. *The algorithm of interpolating windowed FFT for harmonic analysis of electric power system*. IEEE Transactions on Power Delivery, 16(2):160–164, April 2001.
- [5] ISO 10816-3 - *Mechanical vibration - Evaluation of machine vibration by measurements on non-rotating parts - part 3: Industrial machines with nominal power above 15 kW and nominal speeds between 120 r/min and 15 000 r/min when measured in situ*. 2009.
- [6] Bryan Yarborough. *Components and Methods for Current Measurement*. Vishay Dale, 2015.
- [7] USA Fluke Corporation. *Fluke i400s AC Current Clamp - Instruction Sheet*. Fluke, 2004.
- [8] National Instruments. *NI-9238 Voltage card - Datasheet*. NI, 2016.
- [9] Anders Brandt. *Noise and Vibration Analysis: Signal Analysis and Experimental Procedures*. Wiley, 2011.

- [10] P.I Waide and C. Brunner. *Energy-Efficiency Policy Opportunities for Electric Motor-Driven Systems*. Internation Energy Agency, 2011.
- [11] BEMAS. *Challenges for industry in North-West Europe*. MORE4CORE - enfms, 2016.
- [12] Mari Cruz Garcia, Miguel a. Sanz-Bobi, and Javier del Pico. *SIMAP: Intelligent System for Predictive Maintenance*. Computers in Industry, 57(6):552–568, aug 2006.
- [13] Bram Corne, Colin Debruyne, Patrick De Baets, and Jan Desmet. *Stator current measurements as a condition monitoring technology - The-state-of-the-art*. 2014 International Conference on Electrical Machines (ICEM), pages 1659–1665, sep 2014.
- [14] R. Puche-Panadero, M. Pineda-Sanchez, M. Riera-Guasp, J. Roger-Folch, E. Hurtado-Perez, and J. Perez-Cruz. *Improved resolution of the MCSA method via Hilbert transform, enabling the diagnosis of rotor asymmetries at very low slip*. IEEE Transactions on Energy Conversion, 24(1):52–59, 2009.
- [15] William T. Thomson and Mark Fenger. *Current signature analysis to detect induction motor faults*. IEEE Industry Applications Magazine, 7(August):26–34, 2001.
- [16] G.K Singh and Sa’ad Ahmed Saleh Al Kazzaz. *Induction machine drive condition monitoring and diagnostic research - a survey*. Electric Power Systems Research, 64:145–158, 2003.
- [17] Arfat Siddique, G. S. Yadava, and Bhim Singh. *A review of stator fault monitoring techniques of induction motors*. IEEE Transactions on Energy Conversion, 20(1):106–114, 2005.
- [18] Gerald B. Kliman, William J. Premerlani, Birsen Yazici, Rudolph a. Koegl, and Jeff Mazereeuw. *Sensorless, online motor diagnostics*. IEEE Computer Applications in Power, 10(April):39–43, 1997.
- [19] Mohamed El Hachemi Benbouzid. *A review of induction motors signature analysis as a medium for faults detection*. IEEE Transactions on Industrial Electronics, 47(5):984–993, 2000.
- [20] Gojko M. Joksimovic and Jim Penman. *The detection of inter-turn short circuits in the stator windings of operating motors*. IEEE Transactions on Industrial Electronics, 47(5):1078–1084, 2000.
- [21] M. E H Benbouzid and Gerald B. Kliman. *What stator current processing-based technique to use for induction motor rotor faults diagnosis?* IEEE Transactions on Energy Conversion, 18(2):238–244, 2003.
- [22] Levent Eren and Michael J. Devaney. *Bearing Damage Detection via Wavelet Packet Decomposition of the Stator Current*. IEEE Transactions on Instrumentation and Measurement, 53(2):431–436, 2004.

- [23] Michael J. Devaney and Levent Eren. *Detecting motor bearing faults: Monitoring an induction motor's current and detecting bearing failure*. IEEE Instrumentation and Measurement Magazine, 7(December 2004):30–50, 2004.
- [24] Jason R. Stack, Thomas G. Habetler, and Ronald G. Harley. *Bearing fault detection via autoregressive stator current modeling*. IEEE Transactions on Industry Applications, 40(3):740–746, may 2004.
- [25] Jee Hoon Jung, Jong Jae Lee, and Bong Hwan Kwon. *Online diagnosis of induction motors using MCSA*. IEEE Transactions on Industrial Electronics, 53(6):1842–1852, 2006.
- [26] Rangarajan M. Tallam, Sang Bin Lee, Greg C. Stone, Gerald B. Kliman, Jiyoon Yoo, Thomas G. Habetler, and Ronald G. Harley. *A survey of methods for detection of stator-related faults in induction machines*. IEEE Transactions on Industry Applications, 43(4):920–933, 2007.
- [27] Xiadong Li, Qing Wu, and Subhasis Nandi. *Performance analysis of a three-phase induction machine with inclined static eccentricity*. IEEE Transactions on Industry Applications, 43(2):531–541, 2007.
- [28] Wei Zhou, Thomas G. Habetler, and Ronald G. Harley. *Bearing fault detection via stator current noise cancellation and statistical control*. IEEE Transactions on Industrial Electronics, 55(12):4260–4269, dec 2008.
- [29] J. Cusido, L. Romeral, J.a. Ortega, J.a. Rosero, and a. Garcia Espinosa. *Fault Detection in Induction Machines Using Power Spectral Density in Wavelet Decomposition*. IEEE Transactions on Industrial Electronics, 55(2):633–643, 2008.
- [30] M'Hamed Drif and a. J Marques Cardoso. *The use of the instantaneous-reactive-power signature analysis for rotor-cage-fault diagnostics in three-phase induction motors*. IEEE Transactions on Industrial Electronics, 56(11):4606–4614, 2009.
- [31] Arun Gandhi, Timothy Corrigan, and Leila Parsa. *Recent advances in modeling and online detection of stator interturn faults in electrical motors*. IEEE Transactions on Industrial Electronics, 58(5):1564–1575, 2011.
- [32] G. Schweitzer. *Magnetic Bearings*. Proceedings of the First International Symposium, ETHG Zurich, Switzerland, 1989.
- [33] J. Bradna, J. Bauer, S. Fligl, and V. Hlinovsky. *Comparison of Alternative Equivalent Circuits of Induction Motor with Real Machine Data*. Mechanisms and Machine Science, Springer Science and Business, 2012.
- [34] Randy R. Schoen, Thomas G. Habetler, Farrukh Kamran, and Robert G. Bartheld. *Motor bearing damage detection using stator current monitoring*. IEEE Transactions on Industry Applications, 31(6):1274–1279, 1995.

- [35] M. Delgado, G. Cirrincione, a. Garcia, J. a. Ortega, and H. Henao. *A novel condition monitoring scheme for bearing faults based on Curvilinear Component Analysis and hierarchical neural networks*. Proceedings - 2012 20th International Conference on Electrical Machines, ICEM 2012, pages 2472–2478, 2012.
- [36] Wajdi Saadaoui and Kahled Jelassi. *Induction motor bearing damage detection using stator current analysis*. 2011 International Conference on Power Engineering, Energy and Electrical Drives, (May):1–6, 2011.
- [37] Wei Zhou Wei Zhou, Bin Lu Bin Lu, T.G. Habetler, and R.G. Harley. *Incipient Bearing Fault Detection via Motor Stator Current Noise Cancellation Using Wiener Filter*. IEEE Transactions on Industry Applications, 45(4):1309–1317, 2009.
- [38] Lucia Frosini and Ezio Bassi. *Stator current and motor efficiency as indicators for different types of bearing faults in induction motors*. IEEE Transactions on Industrial Electronics, 57(1):244–251, jan 2010.
- [39] Bram Corne, Jos Knockaert, and Jan Desmet. *Emulating Bearing Faults - A Novel Approach*. International Conference on Electrical Machines 2016 (ICEM), 2016.
- [40] Peng Guo, David Infield, and Xiyun Yang. *Wind turbine generator condition-monitoring using temperature trend analysis*. IEEE Transactions on Sustainable Energy, 3(1):124–133, 2012.
- [41] Olivier Janssens, Mia Loccufier, Rik Van de Walle, and Sofie Van Hoecke. *Data-driven imbalance and hard particle detection in rotating machinery using infrared thermal imaging*. Infrared physics and technology, Vol. 82, pages 28–39, 2017.
- [42] Deepak Singh and Antero Arkkio. *Calorimetric measurement of stator core losses*. 2012 XXth International Conference on Electrical Machines, pages 1206–1211, sep 2012.
- [43] Sa McInerny and Y Dai. *Basic vibration signal processing for bearing fault detection*. Education, IEEE Transactions on, 46(1):149–156, 2003.
- [44] Jason R. Stack, Thomas G. Habeter, and Ronald G. Harley. *Fault classification and fault signature production for rolling element bearings in electric machines*. IEEE Transactions on Industry Applications, 40(3):735–739, 2004.
- [45] S. Djurović, D. Vilchis-Rodriguez, and a. C. Smith. *Vibration monitoring for wound rotor induction machine winding fault detection*. Proceedings - 2012 20th International Conference on Electrical Machines, ICEM 2012, pages 1906–1912, 2012.
- [46] Vicente Climente-Alarcon, José a. Antonino-Daviu, Francisco Vedreño-Santos, and Rubén Puche-Panadero. *Vibration transient detection of broken*

- rotor bars by PSH sidebands*. IEEE Transactions on Industry Applications, 49:2576–2582, sep 2013.
- [47] O. Vitek, M. Janda, V. Hajek, and P. Bauer. *Detection of eccentricity and bearings fault using stray flux monitoring*. SDEMPED 2011 - 8th IEEE Symposium on Diagnostics for Electrical Machines, Power Electronics and Drives, pages 456–461, sep 2011.
- [48] Fabio Immovilli, Alberto Bellini, Riccardo Rubini, and Carla Tassoni. *Diagnosis of bearing faults in induction machines by vibration or current signals: A critical comparison*. IEEE Transactions on Industry Applications, 46:1350–1359, 2010.
- [49] Bram Corne, Bram Vervisch, Stijn Derammelaere, Sérgio M.A. Cruz, Jos Knockaert, and Jan Desmet. *Single Point Outer Race Bearing Fault Severity Estimation using Stator Current Measurements*. International Electrical Machine and Drives Conference 2017 (IEMDC), pages 3141–3148, 2017.
- [50] Alberto Bellini, Fiorenzo Filippetti, Giovanni Franceschini, Carla Tassoni, Renzo Passaglia, Massimo Saottini, Giorgio Tontini, Mauro Giovannini, and Alessandro Rossi. *On-field experience with online diagnosis of large induction motors cage failures using MCSA*. IEEE Transactions on Industry Applications, 38(4):1045–1053, 2002.
- [51] Nawal A Hussein and Asst Lect. *3-phase Induction Motor Bearing Fault Detection and Isolation using MCSA Technique based on neural network Algorithm*. Journal of Engineering and Development, 16(3):175–189, 2012.
- [52] W T Thomson and M Fenger. *Current signature analysis to detect induction motor faults*. Industry Applications Magazine, IEEE, 7(4):26–34, 2001.
- [53] Sérgio M a Cruz and a. J Marques Cardoso. *Diagnosis of stator inter-turn short circuits in DTC induction motor drives*. IEEE Transactions on Industry Applications, 40(5):1349–1360, 2004.
- [54] Siwei Cheng, Pinjia Zhang, and Thomas G. Habetler. *An impedance identification approach to sensitive detection and location of stator turn-to-turn faults in a closed-loop multiple-motor drive*. IEEE Transactions on Industrial Electronics, 58(5):1545–1554, 2011.
- [55] Frederick C. Trutt, Joseph Sottile, and Jeffery L. Kohler. *Online condition monitoring of induction motors*. IEEE Transactions on Industry Applications, 38(6):1627–1632, 2002.
- [56] A. Muetze and E. G. Strangas. *On inverter induced bearing currents, bearing maintenance scheduling, and prognosis*. 2014 International Conference on Electrical Machines (ICEM), pages 1915–1921, sep 2014.
- [57] Nadine Lahoud, Jérôme Faucher, David Malec, and Pascal Maussion. *Electrical ageing modeling of the insulation of low voltage rotating machines fed by inverters with the design of experiments (DoE) method*. SDEMPED 2011

- 8th IEEE Symposium on Diagnostics for Electrical Machines, Power Electronics and Drives, pages 272–277, sep 2011.
- [58] Subhasis Nandi. *Detection of stator faults in induction machines using residual saturation harmonics*. IEEE Transactions on Industry Applications, 42(5):1201–1208, sep 2006.
- [59] H. Douglas, P. Pillay, and a. K. Ziarani. *Broken rotor bar detection in induction machines with transient operating speeds*. IEEE Transactions on Energy Conversion, 20(1):135–141, mar 2005.
- [60] Martin Riera-Guasp, M. F. Cabanas, Jose a. Antonino-Daviu, Manuel Pineda-Sánchez, and Carlos H. Rojas García. *Influence of nonconsecutive bar breakages in motor current signature analysis for the diagnosis of rotor faults in induction motors*. IEEE Transactions on Energy Conversion, 25(1):80–89, 2010.
- [61] Mohamed Yazid Kaikaa and Marouane Hadjami. *Effects of the simultaneous presence of static eccentricity and broken rotor bars on the stator current of induction machine*. IEEE Transactions on Industrial Electronics, 61(5):2452–2463, may 2014.
- [62] K. Drobnič, M. Nemec, D. Makuc, R. Fišer, and V. Ambrožič. *Pseudo-salient model of induction machine with broken rotor bars*. SDEMPED 2011 - 8th IEEE Symposium on Diagnostics for Electrical Machines, Power Electronics and Drives, pages 213–220, 2011.
- [63] Subhasis Nandi, Thirumarai Chelvan Ilamparithi, Sang Bin Lee, and Doosoo Hyun. *Detection of eccentricity faults in induction machines based on name-plate parameters*. IEEE Transactions on Industrial Electronics, 58(5):1673–1683, 2011.
- [64] Subhasis Nandi, Raj Mohan Bharadwaj, and Hamid a. Toliyat. *Performance analysis of a three-phase induction motor under mixed eccentricity condition*. IEEE Transactions on Energy Conversion, 17(3):392–399, 2002.
- [65] Jongman Hong, Doosoo Hyun, Sang Bin Lee, and Christian Kral. *Offline monitoring of airgap eccentricity for inverter-fed induction motors based on the differential inductance*. IEEE Transactions on Industry Applications, 49(6):2533–2542, 2013.
- [66] G.M. Joksimovi. *Dynamic simulation of cage induction machine with air gap eccentricity*. IEE Proceedings - Electric Power Applications, 152(4):803, 2005.
- [67] S.M.A. Cruz and A. J. Marques Cardoso. *Rotor Cage Fault Diagnosis in Three-Phase Induction Motors by Extended Park's Vector Approach*. Electric Machines and Power Systems, pages 28:289–299, 2000.

- [68] Myung Jeong, Jangho Yun, Yonghyun Park and Sang Bin Lee, and Konstantinos Gyftakis. *Off-line Flux Injection Test Probe for Screening Defective Rotors in Squirrel Cage Induction Machines*. SDEMPED - IEEE Symposium on Diagnostics for Electrical Machines, Power Electronics and Drives, 2017.
- [69] Rudolf Wieser, Christian Kral, Franz Pirker, and Matthias Schagginger. *On-line rotor cage monitoring of inverter-fed induction machines by means of an improved method*. IEEE Transactions on Power Electronics, 14(5):858–865, 1999.
- [70] Hugh Douglas, Pragasen Pillay, and Alireza K. Ziarani. *A new algorithm for transient motor current signature analysis using wavelets*. IEEE Transactions on Industry Applications, 40(5):1361–1368, 2004.
- [71] P. Pillay and Z. Xu. *Labview implementation of speed detection for mains-fed motors using motor current signature analysis*. IEEE Power Engineering Review, 18:47–48, 1998.
- [72] A.M. Knight and S.P. Bertani. *Mechanical Fault Detection in a Medium-Sized Induction Motor Using Stator Current Monitoring*. IEEE Transactions on Energy Conversion, 20(4):753–760, dec 2005.
- [73] P. J. Tavner. *Review of condition monitoring of rotating electrical machines*. IET Electric Power applications, 2(4):215–247, 2007.
- [74] Birsen Yazici and Gerald B. Kliman. *An adaptive statistical time-frequency method for detection of broken bars and bearing faults in motors using stator current*. IEEE Transactions on Industry Applications, 35(2):442–452, 1999.
- [75] Martin Blodt, Pierre Granjon, Bertrand Raison, and Gilles Rostaing. *Models for bearing damage detection in induction motors using stator current monitoring*. IEEE Transactions on Industrial Electronics, 55(4):1813–1822, 2008.
- [76] Rene J. Romero-Troncoso, Eduardo Cabal-Yepez, Arturo Garcia-Perez, Roque a. Osornio-Rios, Ricardo Alvarez-Salas, and David Granados-Lieberman. *Reconfigurable instrument for power quality monitoring in 3-phase power systems*. 8th IEEE Symposium on Diagnostics for Electrical Machines, Power Electronics & Drives, pages 186–191, sep 2011.
- [77] Annette Muetze. *Bearing Currents in Inverter-Fed AC-Motors*. Technischen Universitaet Darmstadt, Phd-dissertaion, 2010.
- [78] Wei Zhou Wei Zhou, T.G. Habetler, and R.G. Harley. *Stator Current-Based Bearing Fault Detection Techniques: A General Review*. 2007 IEEE International Symposium on Diagnostics for Electric Machines, Power Electronics and Drives, pages 7–10, 2007.
- [79] Ahmed Hamida Boudinar. *Improved stator current spectral analysis technique for bearing fault diagnosis*. 16th International Power Electronics and Motion Control Conference and Exposition, pages 1228–1233, 2014.

- [80] Valéria C M N Leite, Jonas Guedes, Giscard Francimeire, Cintra Veloso, Luiz Eduardo, Senior Member, Germano Lambert-torres, Erik Leandro Bonaldi, Levy Ely, and De Lacerda De Oliveira. *Detection of Localized Bearing Faults in Induction Machines by Spectral Kurtosis and Envelope Analysis of Stator Current*. 62(3):1855–1865, 2015.
- [81] Mario Eltabach and Ali Charara. *Comparative investigation of electric signal analyses methods for mechanical fault detection in induction motors*. Electric Power Components and Systems, pages 1161–1180, 2007.
- [82] Alejandro Paz Parra, Martha Cecilia Amaya Enciso, Javier Olaya Ochoa, and Jairo Arcesio Palacios Penaranda. *Stator Fault Diagnosis on Squirrel Cage Induction Motors by ESA and EPVA*. Workshop on Power Electronics and Power Quality Applications 2013 (PEPQA), 2013.
- [83] L. M. R. Oliveira and A. J. M. Cardoso. *Extended Park's vector approach-based differential protection of three-phase power transformers*. IET Electric Power Applications, 2012.
- [84] Antti Laiho, Anssi Sinervo, Juha Orivuori, Kari Tammi, Antero Arkkio, and Kai Zenger. *Attenuation of harmonic rotor vibration in a cage rotor induction machine by a self-bearing force actuator*. IEEE Transactions on Magnetics, 45(12):5388–5398, 2009.
- [85] David G. Dorrell, Jonathan K H Shek, and Min Fu Hsieh. *The development of an indexing method for the comparison of unbalanced magnetic pull in electrical machines*. IEEE Transactions on Industry Applications, 2015(1):145–153, 2015.
- [86] Bram Corne, Jos Knockaert, and Jan Desmet. *Misalignment and unbalance fault severity estimation using stator current measurements*. International Symposium on Diagnostics for Electrical Machines, Power Electronics and Drives (SDEMPED) 2017, pages 265–272, 2017.
- [87] M Ahrens and L Kucera. *Analytical calculation of fields, forces and losses of a radial magnetic bearing with a rotating rotor considering eddy currents*. 5th Internat. Symp. on Magnetic Bearings, 1996.
- [88] Jeffrey Hillyard. *Magnetic Bearings*. Dissertation of the Technical University of Munich, 2006.
- [89] Karlo Radman, Neven Bulić, and Wolfgang Gruber. *Geometry Optimization of a Bearingless Flux- Switching Slice Motor*. IEEE International Electric Machines & Drives Conference (IEMDC), pages 1695–1701, 2015.
- [90] Parinya Anantachaisilp and Zongli Lin. *An experimental study on PID tuning methods for active magnetic bearing systems*. International Journal on Advanced Mechatronic Systems, 5(2):146–154, 2013.
- [91] A. Tenhunen, T. Benedetti, T.P. Holopainen, and A. Arkkio. *Electromagnetic forces in cage induction motors with rotor eccentricity*. IEEE International Electric Machines and Drives Conference, 3(June):1616–1622, 2003.

- [92] A. Chiba, T. Fukao, O. Ichikawa, M. Oshima, M. Takemo, and D.G. Dorrell. *Magnetic bearings and bearingless drive*. Amsterdam, The Netherlands, 2005.
- [93] Jin Zhou Chaowu Jin, Yuanping Xu and Changli Cheng. *Active Magnetic Bearings Stiffness and Damping Identification from Frequency Characteristics of Control System*. Shock and Vibration 2016, 2016.
- [94] L. Popova, J. Nerg, and J. Pyrhonen. *Combined Electromagnetic and thermal design platform for totally enclosed induction machines*. 8th IEEE Symposium on Diagnostics for Electrical Machines, Power Electronics & Drives, pages 153–158, sep 2011.
- [95] Witold Pawlus, Huynh Van Khang, and Michael R Hansen. *Identification of Induction Motor Thermal Model for Improved Drivetrain Design*. 2016 XXII International Conference on Electrical Machines (ICEM), pages 1778–1784, 2016.

